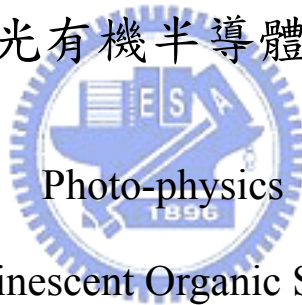# 國立交通大學

物理研究所

博士論文

電致螢光有機半導體之光物理

Photo-physics

of Electroluminescent Organic Semiconductors

研 究 生：陳家勳

指導教授：孟心飛 教授

中華民國九十三年七月

電致螢光有機半導體之光物理

Photo-physics

of Electroluminescent Organic Semiconductors

研 究 生：陳家勳　　　　　　　　　　Student : Chia-Hsun Chen

指導教授：孟心飛　　　　　　　　　　Advisor : Hsin-Fei Meng

國立交通大學

物理研究所

博士論文

A Dissertation
Submitted to Institute of Physics
College of Science
National Chiao-Tung University
in partial Fulfillment of the Requirements
for the Degree of
Doctor of Philosophy
in
Solid State Physics
June 2004
Hsinchu, Taiwan, Republic of China

中華民國九十三年七月

國 立 交 通 大 學

研 究 所 博 士 班

論 文 口 試 委 員 會 審 定 書

本校 ___物理研究___ 所博士班 ___陳家勳___ 君

所提論文 ___電致螢光有機半導體之光物理___

合於博士資格水準，業經本評審委員會評審認可。

口試委員：

指導教授：

所　　長：

中 華 民 國 93 年 6 月 28 日

Institute of Physics

National Chiao Tung University

Taiwan, Republic of Chian
June 28, 2004

We have carefully read the dissertation entitled

Photo-physics of Electroluminescent Organic Semiconductors

Submitted by __Chia-Hsun Chen__ **in partial fulfillment of**

the requirements of the degree of DOCTOR OF PHILOSOPHY

and recommend its acceptance.

Dissertation Advisor:

Director of Institute of Physics:

電致螢光有機半導體之光物理

學生：陳家勳　　　　　　　　　　　　指導教授：孟心飛

國立交通大學物理研究所

摘　　　要

　　我們研究了三個與有機半導體光物理有關的課題：能隙下激發光電流產生機制、藉由磁性摻雜提升電致螢光效益以及可變色多層發光二極體元件模擬。第二章首先回顧了頗受爭議的能隙下光激發光電流實驗。經由深層能階缺陷之俄歇激子解離是為一可能機制。我們也計算了俄歇過程之倒置反應--衝擊離子化。並且提出了運用衝擊離子化過程之單極發光二極體電致螢光發光的可行性。第三章示現了一種提升共軛高分子發光二極體電致螢光發光效益的理論方法。在高分子發光二極體中摻入磁性化合物能夠開啟介於發光單重態激子與非發光三重態激子之間的通道。適當的磁性摻雜濃度，有可能將單重態激子比例從自旋無關的百分之二十五提升上達百分之八十。第四章是多層有機發光二極體的元件模擬。我們提出兩種多層結構，可以在電壓增加時，使發光顏色從橘紅光，變為綠光，再變為藍光。這類結構提供了除了常見的噴墨印表技術以外，另一種利用有機材料達成全彩顯示的具潛力解決方案。

Photo-physics of Electroluminescent Organic Semiconductors

Student: Chia-Hsun Chen   Advisor: Hsin-Fei Meng

Institute of Physics
National Chiao Tung University

Abstract

We study three topics on the photo-physics of organic semiconductors: mechanism for photo-current generation for the excitation below the energy gap; electroluminescence yield improvement by magnetic doping; and device simulation for color-tunable multilayer organic light-emitting diode (LED). Chapter 2 first reviews the controversial photo-current induced by photo-excitation below band gap. Auger exciton dissociation through deep level defects was proposed as the possible mechanism. We calculate the inverse process of Auger process, impact ionization, as well. A feasibility of the electroluminescence for unipolar light-emitting diode based on the impact ionization process is presented. Chapter 3 presents a method to improve the electroluminescence efficiency of conjugated polymer LED theoretically. Doping magnetic complexes into polymer LED can turn on the transition channel between radiative singlet exciton and nonradiative triplet exciton. With suitable concentration for the doped magnetic complexes, it is possible for the singlet exciton ratio being beyond the spin independent value 25% and reach up to 80%. Chapter 4 presents device simulation for multilayer organic LED. Two device structures are shown to have the possibility to tune the luminescence color from orange-red, green, then to blue as the bias voltage increases. These structures provide a potential solution for full-color display with organic material other than the common technology by ink-jet printing method.

誌　　謝

　　能夠完成學業，首先需要感謝的是我的指導教授孟心飛老師，經由他的悉心指引與耐心教導，我才能克服研究過程中的重重困難，完成工作。另外，也要感謝清大的洪勝富老師，從他那裡，我也學習到許多寶貴的研究經驗與專業知識。

　　勝玄，宜秀，紀互，恩仕，立基，宗緯，碩瑋，華賢，長治，俊欣，貴凱，勃學，…，在實驗室的六年期間，看你們兢兢業業投入工作，與你們分享研究心得，是激勵我成長茁壯不可或缺的豐碩泉源。

　　玠郡，偉哥，昭田，文絢，昆憲，…，因為你們的陪伴，這條路才能走得更加沈穩。

　　宋小姐，惠瑛和若淇，甜美欣喜的笑語，讓物理所像個溫暖的家。

　　道行，世昌，這麼十多年來的支持、鼓勵與對人生分秒的認真與用心，是引領你們這個有點憤世嫉俗，常想要深山歸隱的朋友，逐漸成長，一份無法取代的力量。

　　佩君，妳那總是靜靜耐心的傾聽，讓固執冥頑的我，學會開放心胸，勇敢面對一個人不可或缺的情感世界。

　　怡真，平凡生活裡頭的耐人尋味，在與妳相識的時光之中，我嚐到了。

　　米月老師，月雲大姊和佩璇姊，瑜珈課的這兩年時光，時時關心我的工作狀況，何時畢業？讓我能不斷提起精神、投入工作，真正功不可沒。

　　阿媽，爸媽，三姑，大姊和小弟，我親愛家人，你們這麼長時間全心默默的支持，我有說不完的感謝！

Contents

List of Figures

List of Tables

Chapter 1

Introduction to Organic Luminescent Semiconductors

Optoelectronic devices based on organic materials have attracted much attention since the demonstration of the efficient organic light emitting diodes (LEDs) by Tang and van Slyke in 1987, and the first polymer LEDs by Friend in 1990[9, 10]. Their ease of fabrication processes and applicability to flexible and curved substrates, and prospect for much lower cost than their counterpart of inorganic semiconductors make them good candidates for novel flat panel displays which would resolved some severe difficulties for flat panel display based on liquid crystal[11–13]. The ideal display has high brightness, high power efficiency, and low cost[11, 14, 15]. Organic LEDs have promised for satisfying these requirements, making a better understanding of their operation principles very desirable.

This chapter provides some fundamental knowledge to organic LEDs. First, the materials properties of conjugated organic materials is presented. Then the basic operation principles of organic LED devices are discussed. The latest technological status of organic LEDs is reviewed concisely. Finally, with three research topics included in this dissertation, the motivation and structure for each topic, and the mutual relations among them are explained.

1.1   Material properties of conjugated polymer

Inorganic materials are comprised with silicon, however organic materials are made from carbons. The most important difference between inorganic and organic materials is that inorganic materials are "ordered system", however organic materials are "disordered"(Fig. 1.1).

This chapter deals with the materials properties of organic materials used for optoelectronic devices. Some common organic material, small molecule, polymers, and conjugated dendrimers, are shown in Figs. 1.2, 1.3 and 1.4 [1–3, 15]. First the electronic structure of organic materials will be presented, followed by their transport, and finally optical properties.

1.1.1   Electronic structure

The organic materials for organic LEDs are intrinsic semiconductors with large energy gap[16, 17]. The electronic structure of π-conjugated organic semiconductors differs from that of crystalline inorganic semiconductors. The inorganic semiconductor forms a rigid crystalline network, and it is the extended network to determine the electronic structure. The termination of a crystal leads to surface states which lie in the gap and have an effect on

**Silicon   Polyacetylene
film**
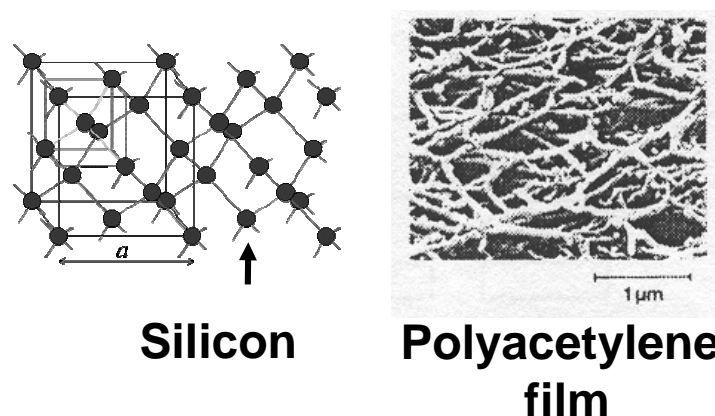
Figure 1.1: The structure for silicon crystal is required for highly ordered arrangement for the atoms; the structure for the polymer chain has order for local area and disorder for global area.

device behavior[18]. The π-conjugated organic has an electronic structure which is basically determined by the conjugation lengths of the polymer or organic molecule[14, 19]. Although such states may arise because of chemical bonding with deposited metals or other organic materials, in general, there is fundamentally no reason for surface states in an organic material. But here are still deep levels states lying in the gap due to other reasons, eg. oxidation, for organic materials [20–22]. Owing to severe electron trapping, electron transport demonstrate trap limited behavior[23–25].

Conjugated organics consist of chains of carbons with alternating double and single bonds(Fig. 1.5(a)). The structural bonding arises from overlap of sp^2 hybridized orbitals which have a strong interaction similar to the overlap of the sp^3 orbitals and form σ bonds with a bonding antibonding orbital splitting of about 10 eV, however in these materials the conduction arises from the overlap of π orbitals to form π bonds which have a weaker interaction and consequently a smaller bonding antibonding orbital splitting (Fig.1.5(b)). The three sp^2 orbitals are coplanar and separated by 120°. The π orbitals are perpendicular to this plane. The σ bonding by sp^2 orbitals from adjacent carbons forms a "planar" backbone, with the conduction π orbitals perpendicular to this plane and therefore having a smaller overlap. The single bonds in the conjugated system consist of a σ bond, the double bonds consist of a σ bond, and a π bond.

Fig. 1.6 illustrates the the energy levels for π-conjugated system. The energy level correspond to the electronic energy levels of electrons or holes
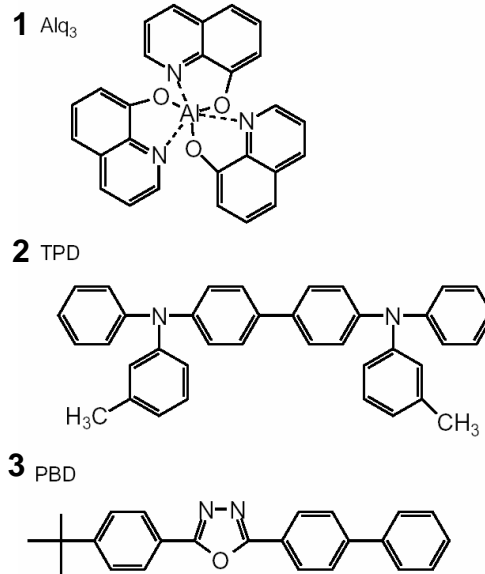
Figure 1.2: Structures of some molecular semiconductors that have been used in thin-film electroluminescent devices. $Alq_3(1)$ is used as an electron transport and emissive layer, TPD(2) is used as a hole transport layer, and PBD(3) is used as an electron transport layer[1].

on a rigid organic molecule or conjugated segment of polymer. Each of these electronic levels consists of many levels due to the vibrational and rotational energy of the host molecule. There are defect levels, notably carbonyls introduced by photo-oxidation of the vinylene bond, which have been shown to lie in the π-π^* gap and degrade performance of polymer light emitting devices[26]. Not all defects lie in the π-π^* gap, and only those that do require attention to prevent them from degrading device performance[15].

When a charge is added to a conjugated organic segment, it induces a structural relaxation of organic, so that the energy levels for electrons and holes shift to lower energies than those given for a rigid molecule[27]. This energy shift is estimated to be 50 meV to 100 meV in organics, compared to a shift of 2meV in GaAs[28, 29]. Because of this relaxation the fundamental charge particle on a segment is not a electron or hole, but rather the quasiparticles which include the electron and the structure deformation it induces or the hole and the structural deformation it induces. These particles are called electron polarons and hole polarons. Since all charge carriers discussed in this work are either electron polarons or hole polarons, they are
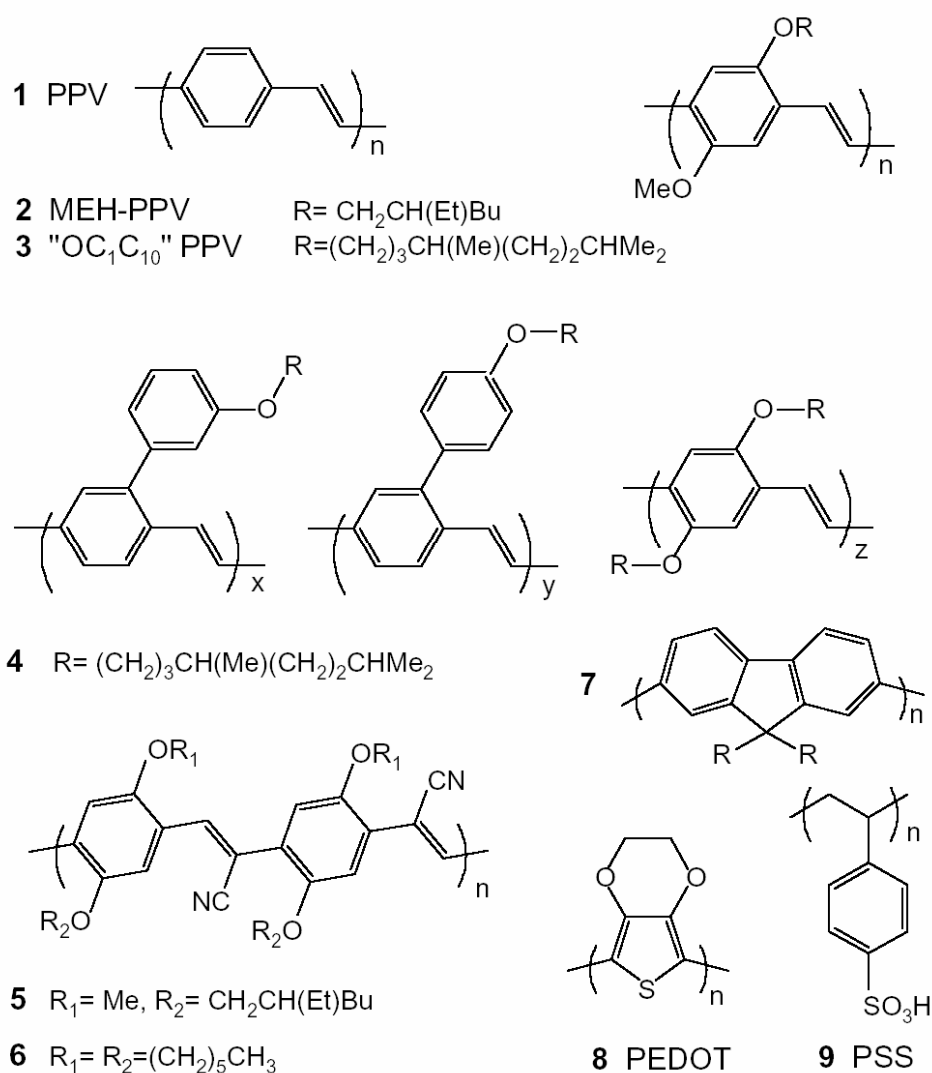
Figure 1.3: Polymers used in electroluminescent diodes. The prototypical (green) fluorescent polymer is poly(*p*-phenylene vinylene), as shown by 1. Condensation polymerization of the bis(halomethyl) monomers affords the two best known (orange-red) solution-processible conjugated polymers MEH-PPV (2) and "OC$_1$C$_{10}$" PPV (3) which have been much used. Copolymers have been widely developed because they allow colour tuning and can show improved luminescence; copolymer 4 has recently been reported to show very high electroluminescence efficiency. Cyano-derivatives of PPV 5 and 6 show increased electron affinities and are used as electron transport materials. Poly(dialkylfluorene)s 7 is high-purity polymer, which show high luminescence efficiencies. 'Doped' polymers such as poly(dioxyethylene thienylene), PEDOT (8), doped with polystyrenesulphonic acid, PSS (9), are widely used as hole-injection layers[1].
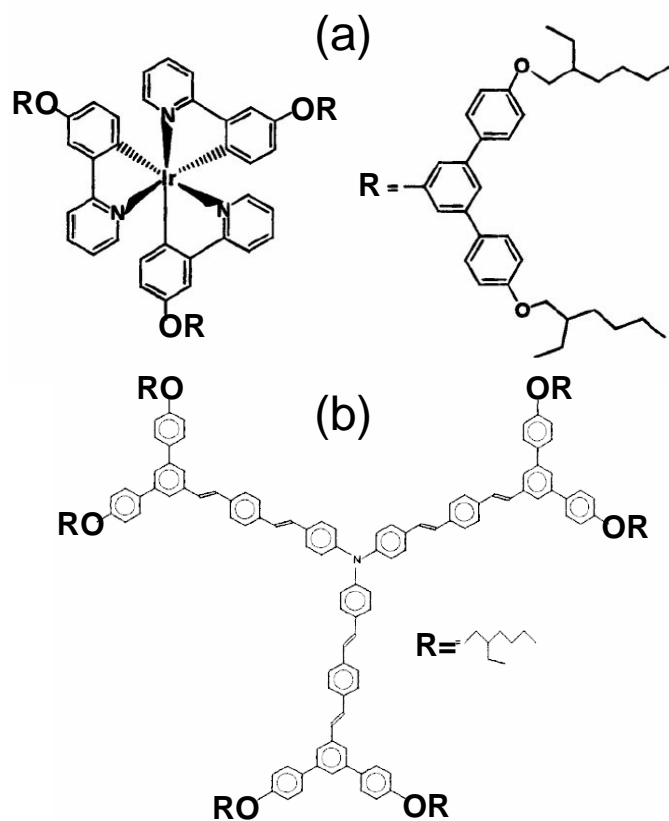
Figure 1.4: The molecular structures of (a) the first generation *fac*-tris-(2-phenylpyridine) iridium cored dendrimer[2] and (b) a conjugated dendrimer consists of three parts: three distyrylbenzene chromophores surrounding a nitrogen core, *meta*-linked biphenyl units as dendrons and alkoxy groups as surface groups[3].

sp² (a)

σ bond

(b)
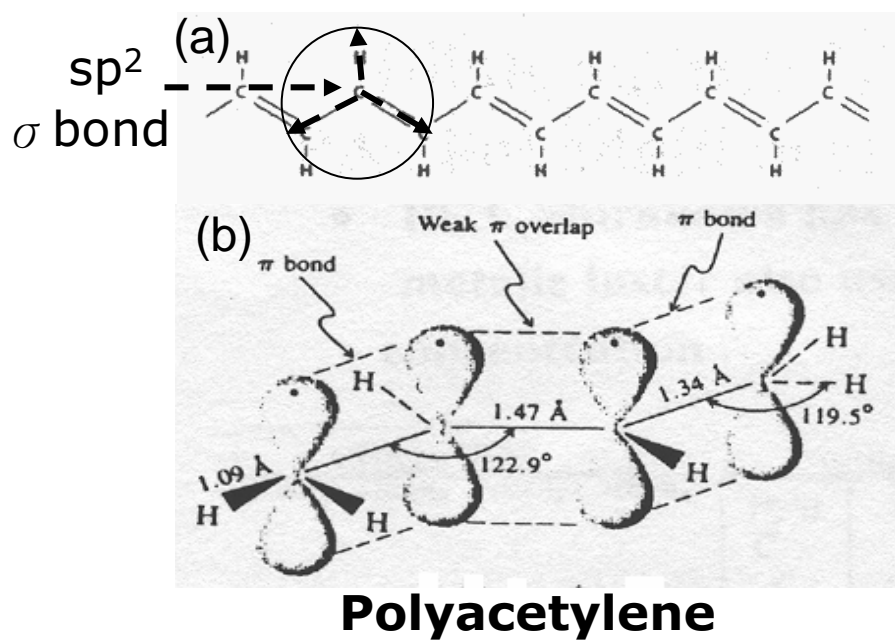
Polyacetylene

Figure 1.5: (a)sp² orbials and σ bonding for polyacetylene; (b) π orbitals and bonding for polyacetylene.

π -conjugated system
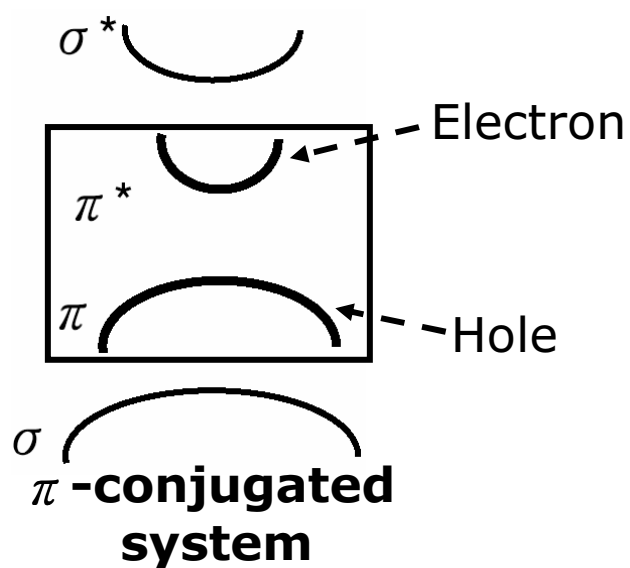
Figure 1.6: Schematic energy diagram for π-conjugated system: organic material which has σ and π bonding.

denoted simply as electrons and holes, the polaronic nature being implicit. The energy levels of the electron and hole polarons form the energy levels for conduction. The conduction is dominated by the highest of the filled energy states and the lowest of the empty energy states. The highest energy of the full states is called the valence energy level on this work, denoted E_V, in chemistry it is called the highest occupied molecular orbital or HOMO. The lowest energy of the empty states is called the conduction energy level in this work, denoted E_C, in chemistry it is called the lowest unoccupied molecular orbital or LUMO.

In organic material, an electron and a hole form a electron-hole pair, the energy for the pair is just the summation for one electron energy and one hole energy. If the distance between them is close enough for the pair to feel the coulomb force for each other, they could form "exciton" state. The energy for an exciton state is lower than that of electron-hole pair by a negative attractive potential due to the Coulomb interaction, which is called exciton "binding energy". Another important difference between inorganic and organic materials is that the exciton binding energy for the organic material is much larger (0.4eV)[30] that for the inorganic material, which ia about several meV. A binding energy of 0.4eV is equivalent to thermal energy for the case of temperature of 4641K, hence under room temperature, the exciton state is very stable, which will not be excited to be dissociated by thermal energy. An exciton state is a "hydrogen-like" state[15], hence the energy level for exciton state has familiar structure as hydrogen atom. There are four kinds of spin states for exciton formation(Fig. 1.7). The exciton spin state with spin angular momentum 0 is called "singlet" exciton, that with spin angular momentum 1 is called "triplet' exciton. Because there are one kind of singlet state and three kinds of triplet state, if the exciton formation is spin-independent, the formation ration for singlet and triplet exciton will be 1:3. Absorbing and emitting one photon can not violate the spin angular momentum conservation: $\Delta S = 0$. The ground state and the singlet exciton is singlet state, the transition between them obeys the dipole selection rule, so the singlet state is radiative. The triplet exciton is triplet state, the transition between the ground state and the triplet exciton state violates the dipole selection rule, so the triplet is nonradiative. Due to exchange interaction[31], there is an large energy difference (1.0eV) between the lowest singlet and triplet state, but the exchange energy between the second lowest singlet and triplet state is around 0.01eV to 0.1eV (Fig. 1.8).
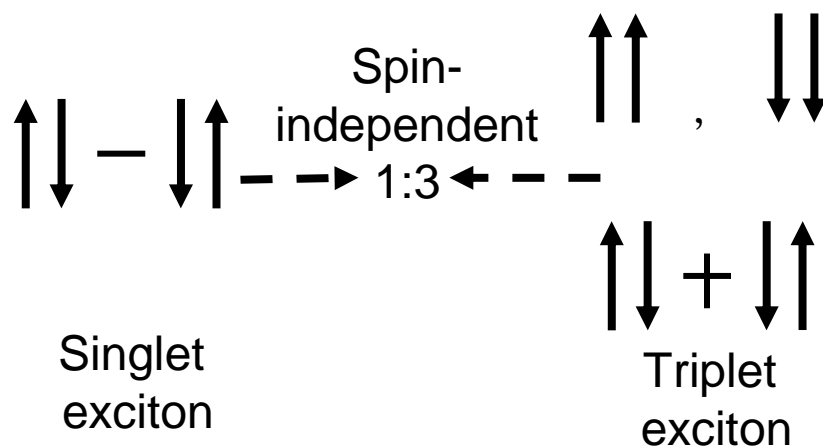
Figure 1.7: Spin singlet and triplet state. If the exciton formation is spin-independent, the singlet to triplet formation ratio is 1:3.
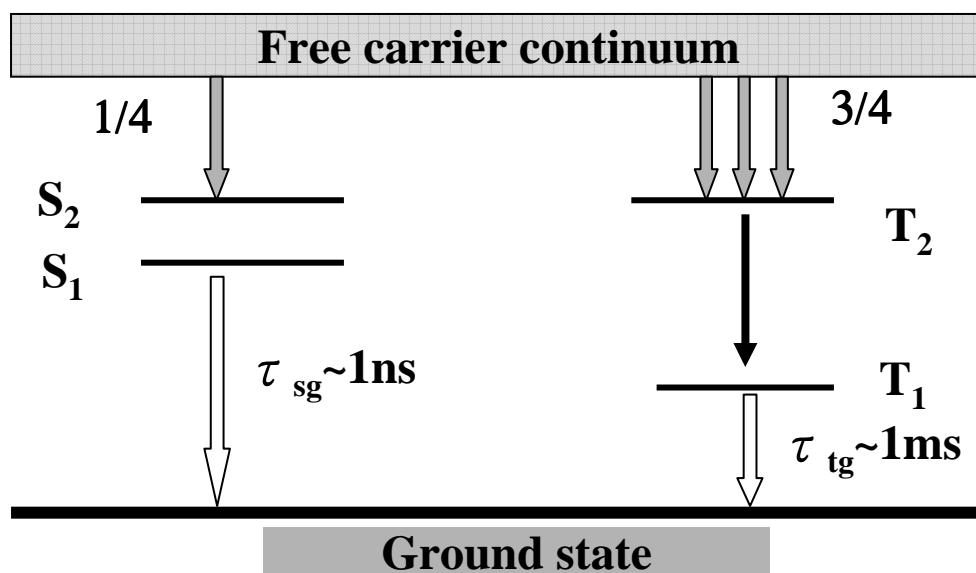
Figure 1.8: The schematic energy structure for organic materials.

1.1.2   Transport properties

So far the energy picture for a single conjugated segment has been presented. The energy diagram appropriate for the description of conduction through this single segment would consist of the two levels E_C and E_V. Now bring together a large number of these segments to form a solid and consider an electron traversing this solid. Motion along the conjugated segments (intra-chain motion) is much easier than the traverse from one segment to another (interchain motion). The ease of this motion depends on how well the π orbitals of the two segments overlap, the distance between the segments, and the energy difference between the conduction levels. The difficult interchain hopping forms the rate limiting step which determines the transport properties. The energy levels of the different segments vary due to distribution in conjugated length, stresses caused by the packing, fluctuations in density or other local environmental factors. Because of this variation, the transport is by hopping through manifolds of localized states which have some random energetic distribution[32–34]. The transport in conjugated organic materials has been studied by a variety of methods. Transient methods include time of flight (TOF), and time resolved current measurements[24, 35–37]. Steady state current voltage characteristics of organic diodes have also been used to determine carrier transport.[38–40]. Many such experiments on different organic materials and systems conclude that the carrier mobilities are strongly field dependent (Fig. 1.9). A possible theoretical description of the physical process leading to this field dependence has been given based on hopping conduction through a distribution of localized states[32–34]. This is the model for transport used in this work. Others describe the transport as trap and release of constant mobility carriers by a distribution of localized trapping states[41, 42]. These two pictures are likely just alternative expressions of the same physical phenomena[43].

1.1.3   Optical properties

Two methods of characterizing the optical properties of materials are by their absorption and photoluminescence spectra[15]. The absorption of a photon leads first to an exciton on a molecule, the exciton then relaxes to its lowest energy state as the molecular structure relaxes. the exciton then diffuses to the lowest energy state available before it recombines. Thus there is a splitting of the absorption and emission spectra because absorption of photons leads to excitons on an unrelaxed molecules, whereas emission is from lower energy excitons on relaxed molecules. The emission spectrum of a single molecule has lower energy than the absorption spectrum of the same
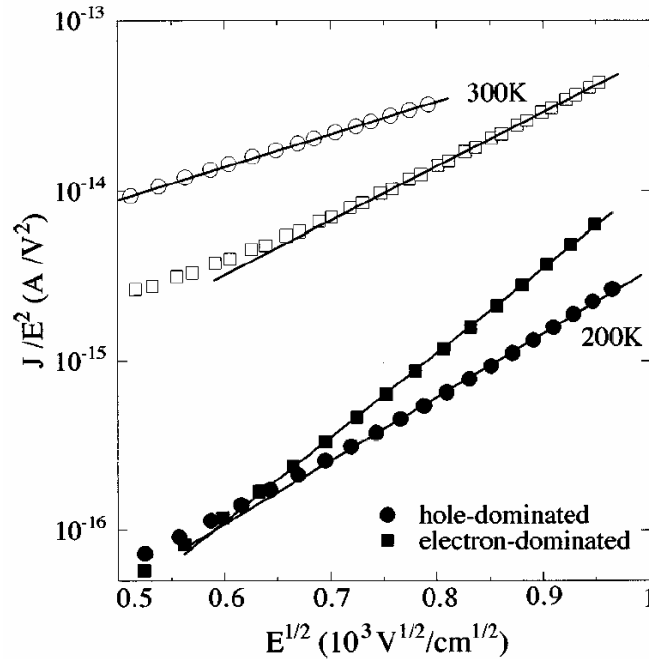
Figure 1.9: The electric field dependence of hole and electron mobilities for MEH-PPV. The calculated mobilities (lines) are considering Poole-Frenkel form mobility[4].

molecule, and has a width which is a measure of the width of the vibrational and rotational states of the molecule. The absorption spectrum is broader because transitions are possible from occupied states in the valence levels to unoccupied states in the conduction level, rather than just from the lowest energy exciton state. In a solid the spectra are broadened further by the distribution of localized states. The emission is now from the lowest energy exciton state in the local region accessible to the the exciton in its lifetime, whereas the absorption is from any full state to any empty unrelaxed state. The emission and absorption spectra are shown in Fig. 1.10 for PPV, a typical conjugated polymer[5].

1.2 Organic Light emitting diode (LED)

The first efficient organic LEDs were reported in 1987, and the first polymer LEDs were reported in 1990[9, 10]. In 1991 the improvement of the injecting electrodes was reported for polymer LEDs[44]. The electronic and optical
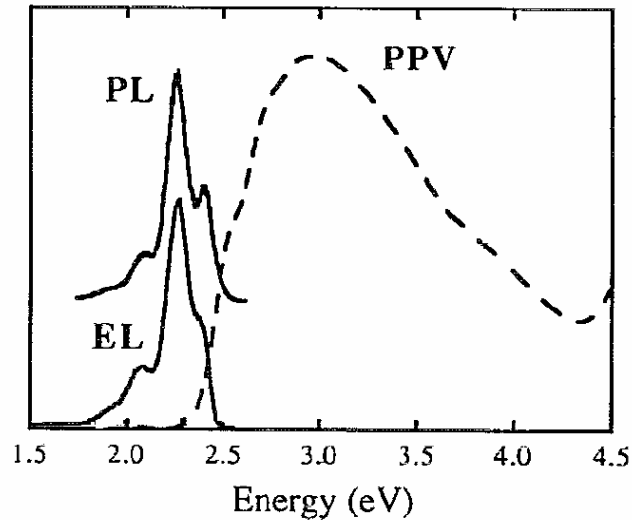
Figure 1.10: Photoluminescence (PL), Electroluminescence (EL), and absorption (dashed line) spectra for a thin film of PPV, a typical conjugated organic polymer[5].

properties of organic LEDs can be varied over wide ranges depending on their chemical composition. Organic molecules interact by weak van der Waals interactions and are relatively insensitive to the nature of the substrate they are deposited on. Polymers can be solution deposited by spin casting or ink jet printing, permitting large area deposition, and substantially lower production costs. Processing temperatures are low, allowing the use of thin, flexible and cheap plastic substrates[14, 15].

The simplest organic LED is a single layer of organic material (PPV) sandwiched between two electrodes as illustrated in Fig. 1.11[15]. The injection of carriers is determined by the barrier between the metal fermi level and the carrier energy level in the organic. For small barriers the contact is easily able to supply carriers, and current is determined by the bulk transport properties of organic material. This is the space charge limited regime[25]. If the barrier is sufficient large, then the organic is able to transport carriers more efficiently than the contact can inject them, and the current is determined by the processes at the contact. This is the contact limited regime. For organic LEDs the contacts are chosen so that one contact can easily inject electrons, and the other can easily inject holes into the organic material. Large work function metals such as platinum or gold are better hole injectors, whereas low work function metals such as calcium or magnesium are better electron
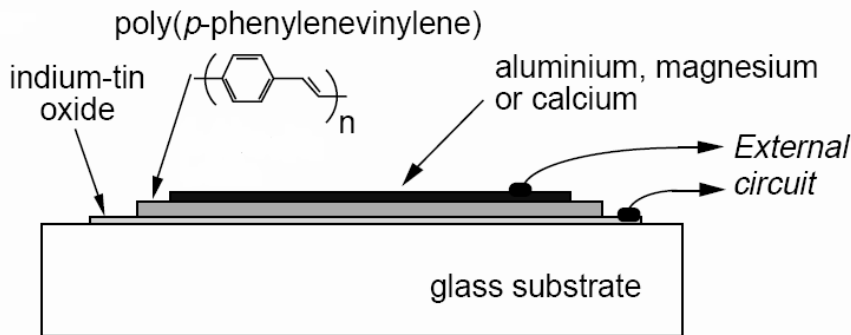
Figure 1.11: Structure of a single-layer polymer LED (ITO/PPV/(Al, Mg, or Ca))[1].

injectors. When a suitable voltage bias is applied across the device the contacts are able to inject holes and electrons into polaron states. The electron and hole polarons drift across the device, and if they meet can form an exciton which may recombine radiatively. If the opposite bias is applied, so that holes are drawn from the contact which easily injects electron, and electrons from the contact which easily injects holes, then essentially no current flows through the device, and no light is emitted. This is illustrated in Fig. 1.12.

The physical processes of interest in an organic LED are injection of carriers at the contacts, transport of carriers across the device, and recombination of carriers in the device[19, 40, 45]. The injection is from the metal into the distribution of localized conduction or valence states. The injection processes, illustrated in Fig. 1.13, are: thermionic emission from the metal into the distribution of localized states in the organic; the time reversed process of thermionic emission which is a backflowing current from the organic material into the contact; and tunneling of carriers from the metal into the organic. Image force lowering of the barrier to injection must be taken into account. It has been shown that for devices of interest tunneling is negligible, and further that thermionic emission and its time reversed process are nearly equal and much larger than the device current at the injecting contact, so that quasithermal equilibrium is established at that contact[45]. This is a nice result because it means that the device characteristics are determined by the quasithermal equilibrium carrier densities at the contact, and the specific forms for the injecting and backflowing current which establish this quasithermal
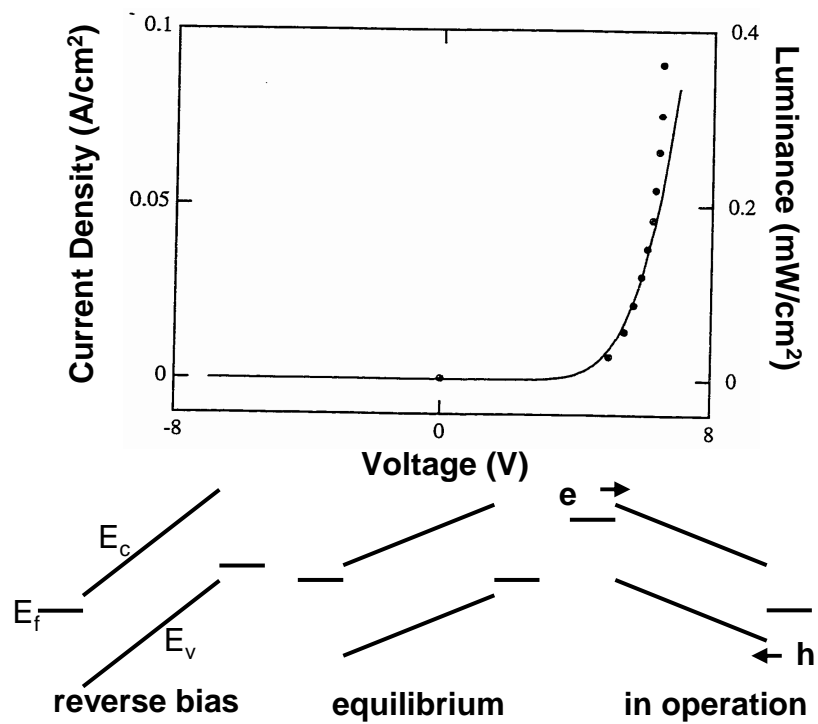
Figure 1.12: Current density (solid line) and luminance (filled circles) for a 100 nm thick Pt/MEH-PPV/Ca device. The schematic energy diagrams below the plot illustrated device operation in equilibrium, reverse bias and in operation[6].
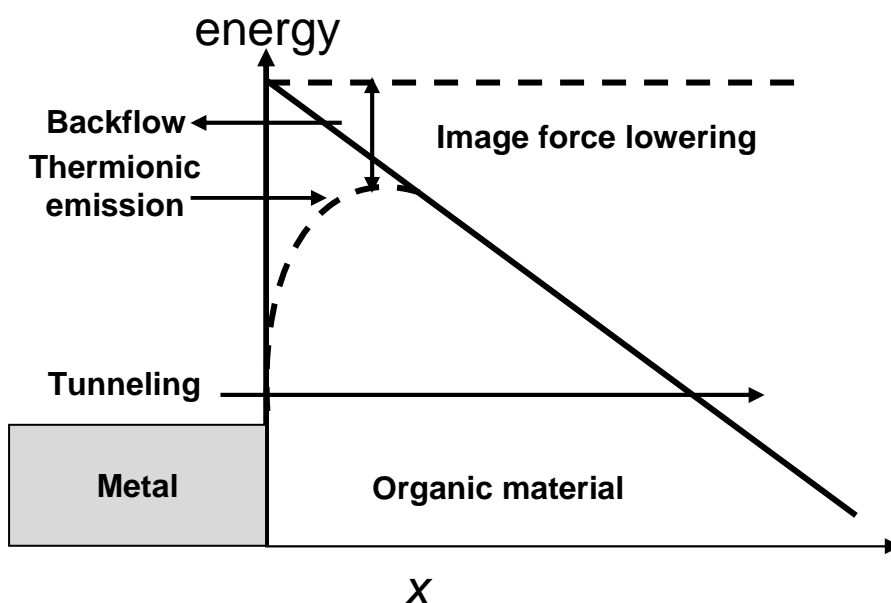
Figure 1.13: Schematic of carrier injection processes at a metal / organic material interface[6].

equilibrium are not important. The energy barrier to injection is very important in determining the injection. These barriers have been measured for a variety of systems. The energy barriers for a variety of metals contacting the polymer MEH-PPV were measured using internal photoemission and electroabsorption and found to follow the ideal Schottky picture[46]. Using these same techniques, the energy barriers for a variety of metals contacting the molecular organic Alq3 has been studied and found to only follow the ideal Schottky picture in some cases[38]. UPS studies of the molecular organic PTCDA on titanium, gold, and indium, show that interface reactions are possible which could destroy the ideal Schottky picture[21, 22]. The transport of carriers across the device through the distribution of localized states is described by a field dependent mobility of the form seen in time of flight measurements. The theory for carrier recombination in low carrier mobility materials has been investigated previously[47, 48]. The result is a bimolecular recombination rate with a Langevin form for the kinetic coefficient. The physical model in organic is of two polarons moving towards each other under the influence of their mutual coulomb attraction and forming an exciton when they meet which quickly recombines.

Multilayer devices are useful for improving the efficiency of organic LEDs when the organic material chosen for emission layer has certain characteris-
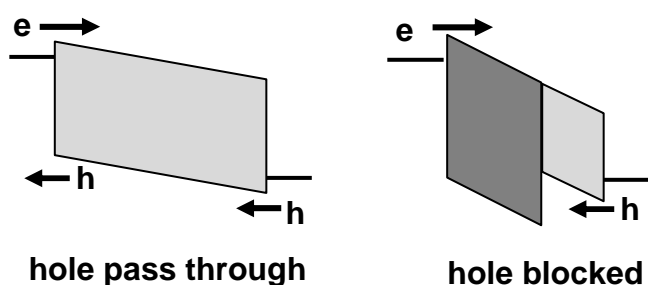
Figure 1.14: Schematic energy diagram of the use of a heterojunction device to prevent holes from traversing the device without recombining[6].

tics that make single layer devices inefficient[14, 15]. These characteristics could be the inability to make space charge limited contact for injection of one or both carriers, or poor transport properties for one or both carriers. The problems that these characteristics can cause in a single layer device are incomplete recombination of one carrier, carrier recombination very near a metal contact where nonradiative losses can occur, and high drive voltages needed to obtain a given light output. Multilayer devices address this problems by including carrier blocking layer to prevent carriers from traversing the device without recombining, or to locate recombination away from the contact, and by electron or hole transport layers which lower the required voltages needed for a given light output. The use of a multilayer device to prevent holes from traversing a devices is illustrated schematically in Fig. 1.14. The physical precesses of concern here are again charge injection from the contacts, charge transport through the organic layers, and carrier recombination in the device, however now charge injection processes at the heterojunction must also be considered. Then injection processes considered at the heterojunction are thermionic emission and its time reversed process, however the barrier lowering and tunneling do not occur.

1.3   Present status for organic LED

The current technological status of organic LEDs are as follows[1, 11, 15]. Single layer polymer LEDs have been reported with external quantum efficiency of about 2%. Multilayer molecular based LEDs have been reported with external quantum efficiency of about 4%. With fluorescence combined with top emission,[49] external quantum efficiency of from 5% to 8% are achievable[50, 51]. The very highest efficiencies are accesible only through the use of electro-phosphorescence, which allows for 100% of the injected

electron-hole pairs to result in emissive triplet exciton[52, 53]. OLEDs based on small molecular weight metallorganic iridium complexes have internal quantum efficiency approaching 100%, resulting in 20-40% external efficiency, depending on whether substrate or top emission schemes are employed[54, 55]. Phosphorescence has not been fully exploited in polymer based systems, significant progress in this direction has been made recently in demonstrating high efficiency red, green, and blue triplet emission in modified forms of poly(vinylcarbazole). The highly external quantum efficiencies of 5.5%, 9%, and 3.5% in respective red, green, and blue PLEDs were achieved by selecting the electron transport material for the emissive layer and optimizing the content of the iridium-complexes unit in the phosphorescent polymer chain[56].

For display applications more useful metrics are power efficiency and luminance. Extremely rapid advances in OLED efficiencies have been made since the early 1990s, with peak efficiencies of 70 (10, 8) lm/W in the green (red, blue) for molecular PHOLEDs (Phosphorescent OLEDs). The operational lifetime of electrophosphorescent devices is as long as, or even exceeds that of fluorescent OLEDs, thereby meeting the needs of many current display platforms[57]. Single layer polymer LEDs with yellow/green emission have been reported with luminous efficiencies of about 2lm/W, peak brightness in excess of 5×10^6cd/m^2, lifetimes at 100 cd/m^2 exceeding 1400 hours, and drive voltages below $4V$ required for brightness of 100 cd/m^2[58]. For multilayer based LEDs luminous efficiencies of about 15 lm/W have been reported for green LEDs. The highest luminances obtained are 10^5cd/m^2, about 3 order brighter than a computer screen. Estimated lifetimes exceeding 50000 hours for a brightness of 100 cd/m^2 have been reported.[14].

Progress in white OLEDs has continued apace, with the highest PHOLED efficiencies reported near 15 lm/W, comparable to that of an unfiltered incandescent lamp[59]. An external quantum yield of 4.5% for white emission in PLED by using blue-phosphorescent and red-phosphorescent polymers was obtained[56].

Note that the OLED efficiencies are measured for devices on flat glass substrates, where the total out-coupling is only 20%. This is compared to ultra-high brightness inorganic AlInGaP red LEDs, where nearly all emitted light is projected into the viewing direction, leading to external efficiencies approximately equal to their internal efficiencies.

Tables. 1.1, 1.2, and 1.3 demonstrate comparisons for the characteristics of performance for the luminescence materials for OLED, the phosphorescence materials for OLED, and the luminescence materials for PLED respectively around two years ago. Although the data are not all updated results for these devices, the trends for the power efficiencies and the lifetime are

still the same. The power efficiency of the green material for these devices are the highest, and that of the red and blue materials are all much lower. The reason for this result is that the sensitivity to light for human eyes is a function of the wave length of the light. The sensitivity strength for the green light is the highest, say 100%, and that for the red and blue light are lower than that for the green, say 35% and 10% respectively. The efficiency for the green material meets the requirement for commercialization, however much labor is needed to be paid to the efficiencies improvement for the red and blue color material. Lifetime for the red light material is longer than that of the green the blue materials. The exact mechanism for this lifetime difference among these materials is still a puzzle. One possible reason for this lifetime difference is the energy gap difference for these materials. In principle, the materials with larger energy gap can transfer more energy into radiations and heats. The heats may cause some chemical interactions for the material, which will make the ability for the transport and the light emission of the materials decaying.

1.4   The structure of this dissertation

Chapter 2 of this dissertation starts from the process on dark current induced by photo-excited below bandgap. Auger exciton dissociation through deep level defects was proposed as the possible mechanism. The inverse process of Auger process, impact ionization, was calculated also. A feasible electroluminescence for unipolar light-emitting diode based on the impact ionization process is presented[60].

Chapter 3 presents a method to improve electroluminescence efficiency of conjugated polymer LED theoretically. Doping magnetic complexes into polymer LED can turn on the transition channel between radiative singlet exciton and nonradiative triplet exciton. With suitable concentration for the doped magnetic complexes, it is possible for the singlet exciton ratio being up to 80% higher than 25% for the spin independent value[61].

Chapter 4 shows device simulation for multilayer organic light-emitting diode. Some structures are shown to have possibility to tune the luminescence color from red, green, then to blue as bias voltage increasing. These structures provide some possible solutions for full-color display with organic material other than the common technology by ink-jet printing method[62].

Color	Characteristics	Kodak 2001	Pioneer 2002	IDEMITSU 2002
R	Efficiency	6 cd/A	2.6 cd/A	3.5 cd/A
R	CIE	(0.67,0.33)	(0.62,0.38)	(0.64,0.36)
R	Lifetime	35,000 hrs @5mA/cm2	10,000 hrs @250 nits	10,000 @500 nits
G	Efficiency	15 cd/A	16 cd/A	--
G	CIE	(0.25,0.62)		--
G	Lifetime	12,000 hrs @5mA/cm2	10,000 hrs @300 nits	--
B	Efficiency	3.5 cd/A	3.9 cd/A	4.7 cd/A
B	CIE	(0.15,0.15)	(0.14,0.12)	(0.15,0.17)
B	Lifetime	12,000 hrs @5mA/cm2	10,000 hrs @100 nits	10,000 hrs @200 nits

Luminescence for OLED

Table 1.1: Device specifications for the luminescence materials of OLED[8].

color	Characteristics	UDC 2001	Pioneer	
R	Efficiency	8.2 cd/A	3.2 cd/A	
R	CIE	(0.65,0.34)	(0.66,0.32)	
R	Lifetime	5000 hrs @ 300 nits	30,000 hrs @ 135 nits	
G	Efficiency	29 lm/W	59 cd/A	25 cd/A
G	CIE	(0.30,0.63)	(0.30,0.64)	(0.30,0.63)
G	Lifetime	> 50,000 hrs	< 1000 hrs @500 nits	3300hrs @818 nits
B	Efficiency	6.3 lm/W	--	
B	CIE	(0.16,0.29)	--	
B	Lifetime	< 1000 hrs	--	

Phosphorescence for OLED

Table 1.2: Device specifications for the phosphorescence materials of OLED[8].

Color	Characteristics	CDT 2001	Dow 2001	Covion 2002
R	Efficiency	2.3 lm/W @100 nits @2.4V	1 lm/W	1.6 cd/A
	CIE	(0.68,0.31)	(0.67,0.33)	(0.67,0.33)
	Lifetime	> 50,000 hrs	10,000 hrs @100 nits	>10,000 hrs @70 Nits
G	Efficiency	15 lm/W @100 nits @2.7V	15.7 lm/W	14 cd/A
	CIE	(0.39,0.58)	(0.39,0.56)	(0.32,0.60)
	Lifetime	~ 10,000 hrs	>10,000 hrs @90 Nits	--
B	Efficiency	2.5 lm/W @100 nits @3.5V	0.4 lm/W	2.7 cd/A
	CIE	(0.16,0.14)	(0.22,0.27)	(0.15,0.12)
	Lifetime	> 2,500	--	10,000 hrs @200 nits
W	Efficiency	1.5 lm/W @100 nits @4.3V	--	~ 7 cd/A
	CIE	--	--	(0.34,0.40)
	Lifetime	> 7,000 hrs	--	--

Luminescence for PLED

Table 1.3: Device specifications for the luminescence materials of PLED[8].

Chapter 2

Defect Auger exciton dissociation and impact ionization in conjugated polymers

2.1 Exciton dissociation and generation by deep level defects

The past ten years has witnessed a tremendous progress in both the science and technologies of light-emitting devices based on conjugated polymers[1]. Yet many fundamental questions regarding the two single important properties, electroluminescence (EL) and photoconductivity (PC), remain unanswered. The defects in the polymer chain, either structural or chemical, are believed to play an important role in both EL and PC. The deep electronic levels associated with the defects provide a convenient way to facilitate the dissociation of the exciton, and limit the luminescence quantum yield in EL. On the other hand, excitons must be dissociated in order to produce charge carriers for PC for excitation below the continuum threshold[63]. Even though the enhancement of PC and reduction of EL by oxidation, presumably due to exciton dissociation at the carbonyl defects, has been reported experimentally[24], the microscopic mechanism which controls the dissociation rate is not well understood.

A new exciton dissociation mechanism, the defect Auger process, is studied in this work. In this process the electron (hole) in the exciton drops into the empty (occupied) deep level while the hole (electron) is released by Coulomb scattering and becomes a free charge carrier with high kinetic energy as required by energy conservation. The corresponding Coulomb matrix element is shown in Fig. 2.1(a) and Fig. 2.1(b). The defect Auger process for exciton is in sharp contrast with the usual free carrier Auger process, which occurs only at high carrier concentrations because the relaxation energy of one free carrier is carried away by the kinetic energy of another nearby free carrier. Therefore the Auger rate usually depends strongly on the free carrier density and consequently the excitation level. On the other hand, in conjugated polymers the electron-hole pair remains bound to form exciton even at room temperature. So when one of the carrier relaxes there is always another oppositely charged carrier nearby to carry away the relaxation energy. In other words, each exicton can act alone and the dissociation rate is independent of the exciton density. This unique mechanism is expected to be quite efficient because the effective carrier distance, the exciton Bohr radius, is very small compared with the mean distance among the excited free carriers. If we use the material parameters suitable for poly(*para*-phenylene vinylene)(PPV) and assume, as in the case of inorganic semiconductor, that each exciton samples the average defect density by interacting with many defects within its lifetime (the volume dissociation regime), our calculation shows that the rate is of the order of $10^{16}s^{-1}$ times the number of defect per
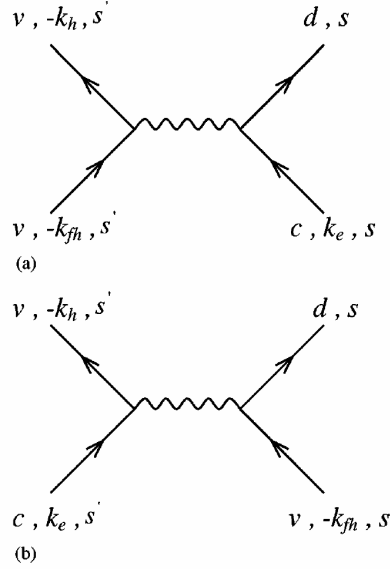
Figure 2.1: (a)Diagram for the direct Coulomb scattering term in which one conduction electron (c, k_e, s) is captured by defect (d), while one free valence electron $(v, -k_{fh}, s')$ is scattered to $(v, -k_h, s')$. k is the wave number, and s is the spin index. (b)Diagram for the exchange Coulomb scattering term in which one valence electron $(v, -k_{fh}, s)$ is captured by defect, while one conduction electron (c, k_e, s') is scattered to the valence band state $(v, -k_h, s')$.

repeat unit, which is expected to be no less than 10^{-3}. Such a high rate is three orders of magnitude faster than the more common multi-phonon emission process[63]. Moreover, it can happen even at zero temperature because no energy barrier is present, consistent with the sweep-out regime experiment[64]. The defect Auger process is therefore identified as the primary microscopic origin for the photocarrier generation and luminescence quenching in conjugated polymers. The calculated dissociation rate can not, however, be used naively to obtain the PL and PC yield quantitatively. For example, the dissociation rate is in the order of $10^{13}\,\text{s}^{-1}$ with defect density equal to one per 400 repeat unit. The corresponding non-radiative lifetime would be around 0.1 picosecond (ps). This value is four order of magnitude shorter than the radiative lifetime of the excitons, and implies that the light emission would be completely quenched if the decay were in the volume dissociation regime. This is, however, inconsistent with the experiment that the PL yield is reduced to only half at such defect density.[65] The reason is that the exciton dissociation process is not in the volume capture regime, in

which each exciton encounters many defects before decay and a uniform exciton density is maintained throughout the system volume. Instead, the decay is in the diffusion regime[65], in which the excitons do not have the chance to sample the average defect density but are immediately quenched by the first defect they hit along the path of their diffusive motion in the chain. In this case, the deep levels act as a black hole and no exciton can pass through it. Unlike the volume dissociation regime, in the diffusion regime the steady state exciton density is not uniform along the chain but vanishes at the defect positions. The decay dynamics of the total number of excitons, controlled not only by the the transition matrix element but also the diffusion coefficient of the excitons, is therefore not a simple exponential. We confirm this picture by calculating the dissociation probability of one single passage of the exciton through the defect with arbitrary incident velocity. The result is indeed close to one for excitons with thermal velocity.

In addition to the Auger process, we also study the rate of its reverse process, the defect impact ionization, by slightly modifying the calculations. Interestingly, in defect impact ionization the incident hot hole can kick out the electron in the deep level and form a neutral exciton with itself when the incident kinetic energy reaches the threshold. The number of charge carriers is reduced from one to zero, in sharp contrast with the usual impact ionization for which the number of carriers multiplies and causes avalanche breakdown eventually. If the kinetic energy of the incident hot hole is increased further, it becomes possible to create a free electron-hole pair and the number of carriers multiplies as usual. In this circumstance the channel for carrier decrease (exicton production) and increase (free pair production) compete. Impact ionization coefficient to neutral exciton is found to be around 10^8/cm times the number of defect per repeat unit when holes are driven by the electric field around 10^5 V/cm. Exicton production by impact ionization opens the possibility of light emission under unipolar charge injection.

In section 2.2, the defect Auger dissociation rate for exciton as a function of the incident exciton momentum is calculated. The matrix element is derived in Appendix A. In section 2.3, the rate for defect impact ionization as a function of the incident hot hole momentum is calculated. Two possible final states, the exciton (2.3.1) and the free electron-hole pair (2.3.2), with different impact thresholds are considered. Averaged impact ionization coefficient for holes under high electric field is calculated in 2.3.3 We discuss and conclude in section 2.4 and 2.5, respectively.

2.2 Defect Auger dissociation of exciton

We start with the total Hamiltonian $H = H_0 + V$ for the π-electrons of a conjugated polymer chain with one deep level, where the one-particle part is

$$H_0 = \sum_{\mu,k} E_\mu(k) a^\dagger_{\mu,k} a_{\mu,k} + E_d a^\dagger_d a_d \,, \qquad (2.1)$$

and the two-body Coulomb interaction is

$$V = \frac{1}{2} \int d^3\mathbf{r}_1 d^3\mathbf{r}_2 \hat\psi^\dagger(\mathbf{r}_1) \hat\psi^\dagger(\mathbf{r}_2) \frac{e^2}{4\pi\epsilon\epsilon_0 |\mathbf{r}_1 - \mathbf{r}_2|} \hat\psi(\mathbf{r}_1) \hat\psi(\mathbf{r}_2) \,. \qquad (2.2)$$

The field operator $\hat\psi$ can be expanded as $\hat\psi(\mathbf{r}) \equiv \sum_{\mu,k} \psi_{\mu,k}(\mathbf{r}) a_{\mu,k} + \psi_d(\mathbf{r}) a_d$. k is the allowed wave number in the Brillouin zone, and $\mu = c, v$ is the band index for conduction and valence bands, respectively. $E_\mu(k)$ is the band disperson. E_d is the deep level energy. $\psi_{\mu,k}(\mathbf{r})$ is the Bloch wavefunction, and $\psi_d(\mathbf{r})$ is the deep level wavefunction. $a_{\mu,k}$, $a^\dagger_{\mu,k}$, and a_d, $a^\dagger_d$ are the corresponding annihilation and creation operators. After substituting the expansion of $\hat\psi(\mathbf{r})$ into V, the Coulomb interaction V can be divided into two parts : $V = V_f + V_d$, where V_f contains only the terms with Bloch state operators, while V_d contains the terms that involve at least one defect operators. It is well known that V_f is strong in conjugated polymers and causes the large exciton binding energy of the excitons. On the other hand, the residual Coulomb interaction V_d involving scattering of Bloch states into and out of the deep level is expected to be weak. Consequently we consider the free part of the Hamiltonian as $H_0 + V_f$, and treat V_d as the perturbation which cause transitions between degenerate eigenstates of $H_0 + V_f$.

2.2.1 Free carrier matrix element

Neglecting the free carrier Coulomb interaction V_f and therefore the exciton effect first. The defect Auger process is a two-body electron-hole Coulomb scattering $e(k_e) + h(k_h) \longrightarrow e(d) + h(k_{fh})$, in which one free electron (e) with wave number k_e drops into the deep defect level(d) while a hole (h) with wave number k_h is scattered to k_{fh} to compensate the energy lost by the electron. "fh" denotes free hole. It can be expressed by the equivalent electron-electron scattering: $e_c(k_e) + e_v(-k_{fh}) \longrightarrow e(d) + e_v(-k_h)$, where c, v denote conduction and valence band, respectively. The transition matrix element of this process is $M_{e-h} = \langle d, -k_{fh} | V_d | k_e, -k_h \rangle$, where $|k', k\rangle \equiv a^\dagger_{c,k'} a_{v,k} |g\rangle$ for the initial state, and $|d, k\rangle \equiv a^\dagger_d a_{v,k} |g\rangle$ for the final state. $|g\rangle$ is the ground state with filled valence band and empty conduction band. The spin indices are

omitted first, and considered afterwards. After substituting the expansion of $\hat{\psi}$ into V_d in M_{e-h}, only two combinations, the direct term and the exchange term, survive. For a spin singlet initial electron-hole pair, the direct term is (Fig. 2.1(a))

$$M_D(k_e, k_h, k_{fh}) = \frac{1}{2} \int \psi_d^*(\mathbf{r}_1)\psi_{v,-k_h}^*(\mathbf{r}_2) \frac{e^2}{4\pi\epsilon\epsilon_0|\mathbf{r}_1 - \mathbf{r}_2|} \psi_{v,-k_{fh}}(\mathbf{r}_2)\psi_{c,k_e}(\mathbf{r}_1)d^3\mathbf{r}_1 d^3\mathbf{r}_2 ,$$

(2.3)

and the exchange term is (Fig. 2.1(b))

$$M_E(k_e, k_h, k_{fh}) = \frac{1}{2} \int \psi_d^*(\mathbf{r}_1)\psi_{v,-k_h}^*(\mathbf{r}_2) \frac{e^2}{4\pi\epsilon\epsilon_0|\mathbf{r}_1 - \mathbf{r}_2|} \psi_{c,k_e}(\mathbf{r}_2)\psi_{v,-k_{fh}}(\mathbf{r}_1)d^3\mathbf{r}_1 d^3\mathbf{r}_2 .$$

(2.4)

The $\mathbf{r}_1$ and $\mathbf{r}_2$ integrals are performed in Appendix A. After some approximations, the final results are

$$M_D(K, k_h, k_{fh}) = \frac{\alpha_c}{\sqrt{N}} \frac{e^2}{4\pi\epsilon\epsilon_0 aN} e^{-i(k_{fh}-K+\frac{\pi}{a})R_d} m_D(k_{fh}, k_h) , \quad (2.5)$$

$$m_D(k_{fh}, k_h) = \frac{4\pi\epsilon\epsilon_0 a}{2e^2} U - \ln\left[2\left|\sin\frac{(k_{fh}-k_h)a}{2}\right|\right] ; \quad (2.6)$$

and

$$M_E(K, k_{fh}) = \frac{2\alpha_v}{\sqrt{N}} \frac{e^2}{4\pi\epsilon\epsilon_0 aN} e^{-i(k_{fh}-K+\frac{\pi}{a})R_d} m_E(K) , \quad (2.7)$$

$$m_E(K) = \gamma\left\{\frac{4\pi\epsilon\epsilon_0 a}{2e^2} U - \ln\left[2\left|\sin(\frac{Ka}{2})\right|\right]\right\} . \quad (2.8)$$

$K \equiv k_e + k_h$ is the total momentum of the electron-hole pair in the initial state divided by $\hbar$. R_d is the position of the defect. U is the on-site Coulomb repulsion energy for the direct term. For the exchange term, the matrix element is reduced by an overall factor γ, as defined in Eq.(A.9). ϵ is the effective dielectric constant along the chain. a is the lattice constant. N is the total number of repeat unit of the chain. The expression for the overlaps $\alpha_{c,v}$ between the defect and Bloch states can be found in Eqs.(A.5) and (A.8) within the "zero-radius potential" approximation. π/a is the wave number at the direct band gap. For a triplet pair, the result of M_E is zero. We consider only the singlet pair below because it is more relevent for the PC and EL processes. Adding M_D and M_E together we get the matrix element M_{e-h} for a electron-hole pair

$$
\begin{aligned}
M_{e-h}(K, k_h, k_{fh}) &= M_D(K, k_h, k_{fh}) + M_E(K, k_{fh}) \\
&= \frac{2e^2}{4\pi\epsilon\epsilon_0 a N^{3/2}} e^{-i(k_{fh} - K + \frac{\pi}{a})R_d} \\
&\quad \{\alpha_c m_D(k_{fh}, k_h) + 2\alpha_v m_E(K)\} \, . \quad (2.9)
\end{aligned}
$$

2.2.2 Exciton matrix element

Due to the Coulomb attraction V_f between the electron and the hole, the elementary excitation of the free part of the Hamiltonian $H_0 + V_f$ is no longer a free electron-hole pair but a superposition of them, i.e. the exciton state, labelled by $|ex; K\rangle$. $K = k_e + k_h$ is the new exciton center of mass wave number. $|ex; K\rangle$ is the initial state of the dissociation process, while the final state is still $|d, -k_{fh}\rangle$ as in Appendix A. The exciton state $|ex; K\rangle$ can be expanded as $\sum_{k_e} \phi(K, k_e)|k_e, k_e - K\rangle$. The envelope function ϕ is approximated by a normalized Lorenzian factor[66]

$$
\phi(K, k_e) \equiv \frac{2}{a_0\sqrt{Na_0 a}} \left[(\frac{1}{a_0})^2 + (k_e - \frac{\pi}{a} - \frac{W_v}{W_{ex}}K)^2 \right]^{-1} . \quad (2.10)
$$

W_v and W_{ex} are the bandwidth of the valence and exciton bands, respectively. a_0 is the exciton Bohr radius. In order to get the exciton matrix element, we need to multiply the matrix element for each electron-hole pair by the corresponding envelope function, and sum over all pairs with a given exciton wave number K. Matrix element M_{ex}^A for defect Auger dissociation of exciton through Coulomb scattering is

$$
\begin{aligned}
M_{ex}^A(K, k_{fh}) &\equiv \langle d, -k_{fh}|V_d|ex; K\rangle = \sum_{k_e} \phi(K, k_e)\langle d, -k_{fh}|V_d|k_e, k_e - K\rangle \\
&= \sum_{k_e=0}^{2\pi/a} \frac{2}{a_0\sqrt{Na_0 a}} \\
&\quad \left[(\frac{1}{a_0})^2 + (k_e - \frac{\pi}{a} - \frac{W_v}{W_{ex}}K)^2 \right]^{-1} M_{e-h}(K, k_h, k_{fh}) . \quad (2.11)
\end{aligned}
$$

M_{e-h} is given in Eq.(2.9).

2.2.3 Exciton dissociation rate

The rates $W^A(K)$ of defect Auger dissociation for initial exciton wave number K in a chain with N repeat units and one defect can be obtained by summing

over all possible final free hole momenta:

$$W^A(K) = \frac{2\pi}{\hbar} \sum_{k_{fh}} |M_{ex}^A(K, k_{fh})|^2 \delta \left\{ E_{ex}(K) - \left[\frac{1}{2}\varepsilon_g + \Delta\varepsilon - E_v(k_{fh})\right]\right\} .$$

(2.12)

The $\delta-$function imposes the energy conservation condition. Set the origin of energy at the valence band top, $\Delta\varepsilon$ is the deviation of deep level energy E_d from the mid-gap at $\frac{1}{2}\varepsilon_g$. $E_v(k)$, $E_c(k)$ and $E_{ex}(K)$ are the dispersions for the valence, conduction and exciton bands, respectively. They are approximated as $E_v(k) = -\frac{W_v}{2} - \frac{W_v}{2}\cos(ka)$, $E_c(k) = \varepsilon_g + \frac{W_c}{2} + \frac{W_c}{2}\cos(ka)$, and $E_{ex}(K) = \varepsilon_g - \varepsilon_B + \frac{W_{ex}}{2} + \frac{W_{ex}}{2}\cos(Ka)$. The corresponding kinetic energy for the bands are defined as $\varepsilon_v(k) \equiv -E_v(k)$, $\varepsilon_c(k) \equiv E_c(k) - \varepsilon_g$, and $\varepsilon_{ex}(K) \equiv E_{ex}(K) - \varepsilon_g + \varepsilon_B$. Their densities of states $\mathcal{G}(\varepsilon) = (\pi|\varepsilon'(k)|)^{-1}$ are $\mathcal{G}_v(\varepsilon) = \left(\pi a\sqrt{(\frac{W_v}{2})^2 - (E_v(k) + \frac{W_v}{2})^2}\right)^{-1}$, $\mathcal{G}_c(\varepsilon) = \left(\pi a\sqrt{(\frac{W_c}{2})^2 - (E_c(k) - \varepsilon_g - \frac{W_c}{2})^2}\right)^{-1}$, and $\mathcal{G}_{ex}(\varepsilon) = \left(\pi a\sqrt{(\frac{W_{ex}}{2})^2 - (E_{ex}(Ka) - \varepsilon_g + \varepsilon_B - \frac{W_{ex}}{2})^2}\right)^{-1}$. W_{ex} is equal to $(1/W_c + 1/W_v)^{-1}$ within the effective mass approximation. With these expressions, we can change variable from k_{fh} to ε_{fh}, the final hole kinetic energy, with two-fold degeneracy at $+k_{fh}$ and $-k_{fh}$. The rate $W^A(K)$ becomes

$$\begin{aligned}
W^A(K) &= \frac{4a_0 e^4}{(2\pi)^2\hbar(4\pi\epsilon\epsilon_0)^2 N} \frac{1}{\pi a\sqrt{(\frac{W_v}{2})^2 - (\frac{1}{2}\varepsilon_g + \Delta\varepsilon - E_{ex}(K) + \frac{W_v}{2})^2}} \times \\
&\left\{ \left(\int_0^{2\pi/a} dk_e \phi'(K, k_e)[\alpha_c m_{D+}(K, k_e) + 2\alpha_v m_E(K)]\right)^2 + \right. \\
&\left. \left(\int_0^{2\pi/a} dk_e \phi'(K, k_e)[\alpha_c m_{D-}(K, k_e) + 2\alpha_v m_E(K)]\right)^2 \right\} ,
\end{aligned}$$

(2.13)

where $\phi'(K, k_e) = \left[1 + (k_e - \frac{\pi}{a} - \frac{W_v}{W_{ex}}K)^2 a_0^2\right]^{-1}$, and

$$\begin{aligned}
m_{D\pm}(K, k_e) &= \frac{4\pi\epsilon\epsilon_0 a}{2e^2}U \\
&- \ln\left\{ 2\left|\sin\left[(\frac{\pi}{a} \pm \frac{1}{a}\cos^{-1}(\frac{W_v + 2(-E_{ex}(K) + \frac{1}{2}\varepsilon_g + \Delta\varepsilon)}{W_v}) + k_e - K)\frac{a}{2}\right]\right|\right\} .
\end{aligned}$$

(2.14)

Note that when the argument of the sin function in Eq.(2.14) is zero, i.e. $k_{fh} = k_h$ in Eq.(2.6), $m_{D\pm}$ meets logarithmic singularity, which is integrable in the expression for $W^A(K)$. The rate W^A is, however, not the most convenient quantity to characterize the dissociation efficiency of the defect because

Parameter	Value	Description
a_0	50 Å[67]	Bohr-radius of exciton
a	6.5 Å	Lattice constant
ϵ	2.75[68]	Single chain dielectric constant
W_v	2.3 eV[68]	Band width for valance band
W_c	2.0 eV[68]	Band width for conduction band
W_{ex}	1.07 eV	Band width for exciton band
ε_g	2.8 eV[67]	Energy gap
ε_B	0.34 eV[67]	Binding energy of exciton
U	5.1 eV[68]	On-site energy
γ	0.25[68]	Correction of U for exchange term
τ_{ph}	40 fs [69]	Phonon emission time

Table 2.1: All parameters, suitable for PPV, used in the calculations are listed with references given after the values.

it is inversely proportional on the chain size N. In practice, the dissociation rate $1/\tau^A$ is equal to W^A times the number of defect in the chain, which is also proportional to N for a fixed defect density. For convenience, we define a chain size independent quantity $c^A(K)$, the volume dissociation rate, as $W^A(K)N$. The actual dissociation rate $1/\tau^A$ is therefore $c^A(K)$ multiplied by the defect density, defined as the average number of defect per repeat unit. $c^A(K)$ is shown in Fig. 2.2. The singularity of at $K = 0$ is due to the logarithmic divergence of the exchange term $m_E(K)$. Temperature(T) dependence for the thermal averaged rate $c^A(T)$ can obtained by averaging $c^A(K)$ over the exciton wavenumber K, with the Boltzman weighting factor $\exp -\beta\hbar^2K^2/2M$, where M is the sum over electron and hole masses. $c^A(T)$ is shown in Fig. 2.3. The values of all the parameters used in this paper are listed in Table 2.1. They are designated for PPV.

2.2.4 Capture probability for one passage

So far we suppose the center-of-mass wavefunction of the exciton is a plane wave extended all over the chain. In reality, it is more reasonable to describe the exciton as a wave packet with finite size in the real space. The wave packet diffuses randomly on the polymer chain due to thermal fluctuations. Whether they will be captured (dissociated) by the defect they encounter depends on both the transition rate $1/\tau$, and the interaction time t during which the wave packet covers the defect. t is in turn determined by the
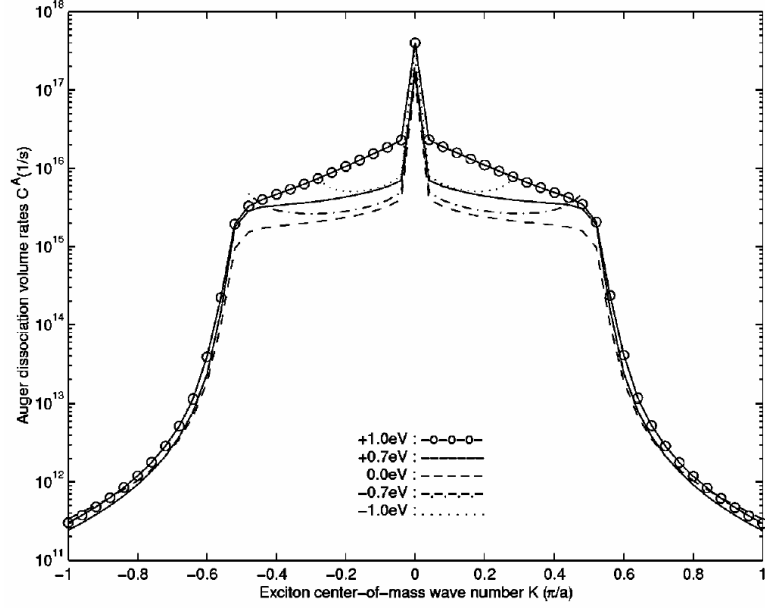
Figure 2.2: Volume exciton dissociation rate $c^A(K)$ (see text) for defect Auger process is plotted as a function of the exciton center-of-mass wave number K for various defect level energy $\Delta\varepsilon$ measured from the midgap. The curves for $\Delta\varepsilon = -0.7$ and -1.0 eV stop at $K \approx \pm 0.5\pi/a$ and $\pm 0.3\pi/a$, beyond which the energy released to the free hole exceeds the valence band width.

incident group velocity $v_g(K) = \partial E_{ex}/\hbar\partial K$. The capture probability $P^A(t)$ is given by $P^A(t) = 1 - e^{-t/\tau}$. Note that $P^A(t) = 0$ for $t = 0$ when the exciton wave packet just starts to hit the defect, and $P^A(t) \simeq 1$ when $t \gg \tau$. The interaction time t is equal to $\xi/|v_g|$, where ξ is the exciton wave packet size alone the chain. On the other hand, the transition rate $1/\tau$ is equal to $c^A(K)a/\xi$, where $c^A(K)$ is the volume dissociation rate, and a/ξ is the effective defect density for the wave packet. t/τ can be then replaced by $c^A(K)a/|v_g(K)|$, in which the unspecified exciton size ξ is cancelled. The passage capture probability is finally given by the simple result $P^A(K) = 1 - \exp\left[-c^A(K)a/|v_g(K)|\right]$. $P^A(K)$ is shown in Fig. 2.4. It is close to one when the incident velocity v_g is equal to the thermal velocity of 10^5 cm/s at room temperature. The deep levels therefore act as efficient quenching centers, which are crucial for the 1D diffusion model of PL decay dynamics.[65] $P^A(K)$ drops for higher K because of the decrease of interaction time t for fast exciton passage.
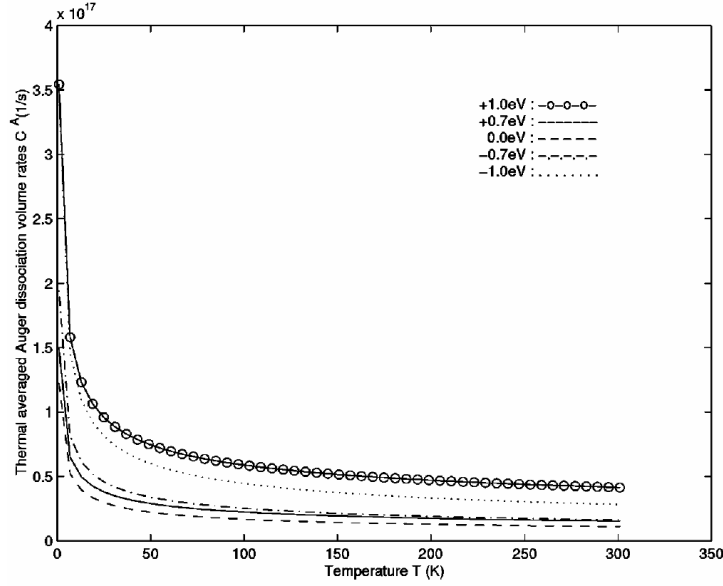
Figure 2.3: Thermal averaged volume transition rates c^A of defect Auger exciton dissociation, shown as a function of temperature.

2.3 Impact ionization

The above calculations can be slightly modified to obtain the rate for defect impact ionization, which is the reverse process of defect Auger dissociation. Now the initial state $|d, -k_{fh}\rangle$ has a free hole with large wave number k_{fh} and a electron in the defect level. There are two possible final states, an exciton $|ex; K\rangle$ with lower threshold and a single electron-hole pair $|k_e, k_{fh}\rangle$ with higher threshold. They are considered in order below.

2.3.1 Exciton production

The matrix element M_{ex}^I for the creation of an exciton by a hot hole is $\langle ex, K|V_d|d, -k_{fh}\rangle$. Summing over all possible final states and use the proper density of state $\mathcal{G}_{ex}(\varepsilon_{ex})$ for the exciton, we get the expression for the rate of impact ionization:

$$
\begin{aligned}
W_{ex}^I(k_{fh}) &= \frac{2\pi}{\hbar} \sum_K |M_{ex}^I(K, k_{fh})|^2 \delta\left\{\left[\frac{1}{2}\varepsilon_g + \Delta\varepsilon - E_v(k_{fh})\right] - E_{ex}(K)\right\} \\
&= \frac{4a_0 e^4}{(2\pi)^2 \hbar (4\pi\epsilon\epsilon_0)^2 N} \frac{1}{\pi a \sqrt{(\frac{W_{ex}}{2})^2 - (\frac{1}{2}\varepsilon_g + \Delta\varepsilon - E_v(k_{fh}) - \varepsilon_g + \varepsilon_B - \frac{W_{ex}}{2})^2}}
\end{aligned}
$$
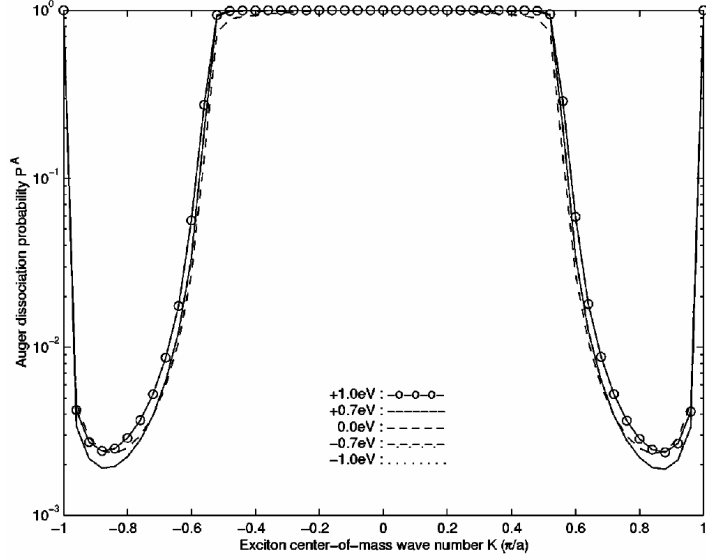
Figure 2.4: Dissociation probability $P^A(K)$ of an exciton passing through the defect is plotted as a function of center-of-mass wavenumber K of exciton. Rise at large K near the zone boundary is due to the smaller group velocity and longer interaction time.

$$\left\{ \left(\int_0^{2\pi/a} dk_e \phi'(K, k_e)[\alpha_c M_{exD+}^I(k_e, k_{fh}) + 2\alpha_v M_{exE+}^I(k_{fh})] \right)^2 + \right.$$

$$\left. \left(\int_0^{2\pi/a} dk_e \phi'(K, k_e)[\alpha_c M_{exD-}^I(k_e, k_{fh}) + 2\alpha_v M_{exE-}^I(k_{fh})] \right)^2 \right\} ,$$

where

$$M_{exD\pm}^I(k_e, k_{fh}) = \frac{4\pi\epsilon\epsilon_0 a}{2e^2} U$$

$$-\ln\left\{ 2\left| \sin\left[\left(k_{fh} + k_e - (\pm\frac{1}{a}\cos^{-1}(\frac{\varepsilon_g + 2\Delta\varepsilon - 2E_v(k_{fh}) - 2\varepsilon_g + 2\varepsilon_B - W_{ex}}{W_{ex}})) \right) \frac{a}{2} \right] \right| \right\} ,$$

and

$$M_{exE\pm}^I(k_{fh}) = \frac{4\pi\epsilon\epsilon_0 a}{2e^2}$$

$$\gamma U - \gamma\ln\left\{ 2\left| \sin\left[\pm\frac{1}{2}\cos^{-1}(\frac{\varepsilon_g + 2\Delta\varepsilon - 2E_v(k_{fh}) - 2\varepsilon_g + 2\varepsilon_B - W_{ex}}{W_{ex}}) \right] \right| \right\} .$$

Similar to Section 2.2.3, with the above result we get volume ionization rate $c_{ex}^I \equiv W_{ex}^I N$, which is shown in Fig. 2.5. The corresponding passage probability for impact ionization P_{ex}^I is shown in Fig. 2.6.
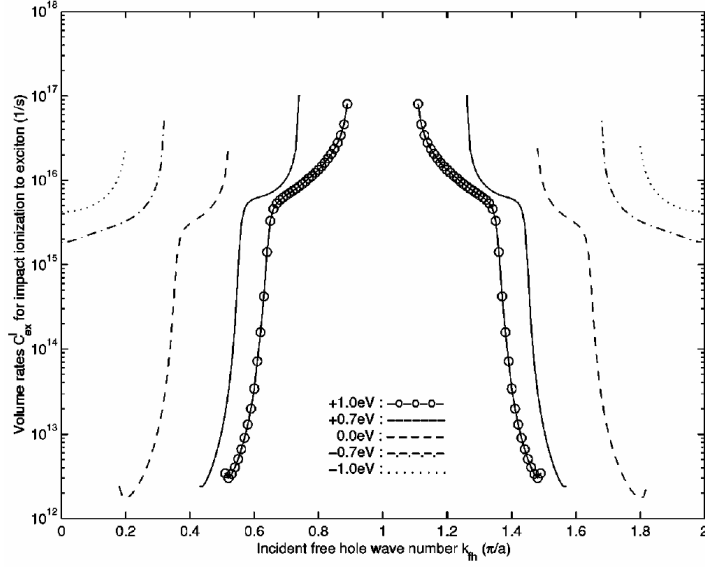
Figure 2.5: Volume transition rate c_{ex}^I of defect impact ionization to exciton is shown as a function of incident hot hole momentum $\hbar k_{fh}$. All curves have threshold momentum required by the energy difference between the defect energy and the exciton energy. The curves of +1.0 eV, +0.7 eV and 0.0 eV stop at certain momenta, beyond which no final exciton state satisfies the energy conservation. This is because the exciton band width 1.1 eV is smaller than valence band width 2.3 eV for the incident free hole.

2.3.2 Electron hole pair production

Matrix element M_{e-h}^I for the creation of a free electron-hole pair is equal to $\langle k_e, k_h | V_d | d, k_{fh} \rangle$. We sum over k_e and k_h to include all combinations of electron hole pair, and impose the proper energy conservation condition. Integrating over k_h first, we obtain

$$
\begin{aligned}
W_{e-h}^I(k_{fh}) &= \frac{2\pi}{\hbar} \sum_{k_e, k_h=0}^{\frac{2\pi}{a}} |M_{e-h}^I(k_e, k_{fh})|^2 \delta \left\{ (E_c(k_e) - E_v(k_h) - \left[\frac{1}{2}\varepsilon_g + \Delta\varepsilon - E_v(k_{fh}) \right] \right\} \\
&= \frac{e^4}{2\pi^2 \hbar (4\pi\epsilon\epsilon_0 a)^2 N} \\
&\quad \left\{ \left[\int_0^{2\pi} dk_e \mathcal{G}_v'(k_e, k_{fh}) \left(\alpha_c M_{ehD+}^I(k_e, k_{fh}) + 2\alpha_v M_{ehE+}^I(k_e, k_{fh}) \right)^2 \right] + \right. \\
&\quad \left. \left[\int_0^{2\pi} dk_e \mathcal{G}_v'(k_e, k_{fh}) \left(\alpha_c M_{ehD+}^I(k_e, k_{fh}) + 2\alpha_v M_{ehE-}^I(k_e, k_{fh}) \right)^2 \right] \right\} ,
\end{aligned}
$$
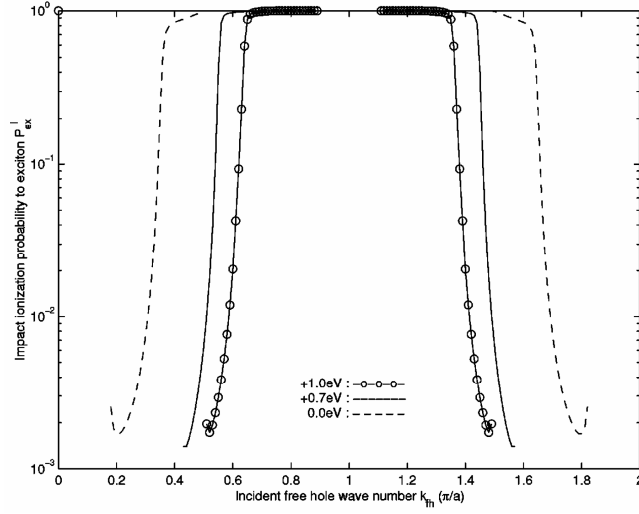
Figure 2.6: Probability for the defect impact ionization to exciton state by a hole which passes through the defect with momentum $\hbar k_{fh}$.

where

$$\mathcal{G}'_v(k_e, k_{fh}) = \frac{1}{\sqrt{(\frac{W_h}{2})^2 - (E_c(k_e) + E_v(k_{fh}) - \frac{1}{2}\varepsilon_g - \Delta\varepsilon + \frac{W_v}{2})^2}} \;,$$

$$M^I_{ehD\pm}(k_e, k_{fh}) = \frac{4\pi\epsilon\epsilon_0 a}{2e^2} U$$

$$-\ln\left\{2\left|\sin\left[\left(\frac{\pi}{a} \pm \frac{1}{a}\cos^{-1}(\frac{2E_c(k_e) + 2E_v(k_{fh}) - 2\varepsilon_g - 2\Delta\varepsilon + W_v}{W_v}) - k_{fh}\right)\frac{a}{2}\right]\right|\right\} \;,$$

and

$$M^I_{ehE\pm}(k_e, k_{fh}) = \frac{4\pi\epsilon\epsilon_0 a}{2e^2}\gamma U$$

$$-\gamma\ln\left\{2\left|\sin\left[\left(\frac{\pi}{a} \pm \frac{1}{a}\cos^{-1}(\frac{2E_c(k_e) + 2E_v(k_{fh}) - 2\varepsilon_g - 2\Delta\varepsilon + W_v}{W_v}) + k_e\right)\frac{a}{2}\right]\right|\right\} \;.$$

We then perform the k_e integration numerically to get the final result for W^I_{e-h} . Again, we define the volume ionization rate $c^I_{e-h}(k_{fh}) \equiv W^I_{e-h}(k_{fh})N$, which is shown in Fig. 2.7. The passage probability is not shown, because it is practically one for all wave number above the threshold.
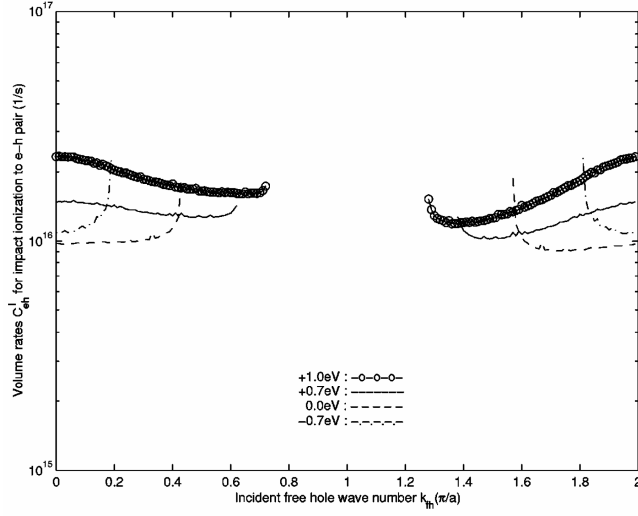
Figure 2.7: Volume transition rate c_{e-h}^I of defect impact ionization to free electron-hole pair by an incident hole with momentum $\hbar k_{fh}$.

2.3.3 Impact ionization coefficient under high electric field

Impact ionization coefficient $\alpha(E)$, defined as the ionization probability per unit drift length of the hot hole, is equal to $W^I(E)/v_d$, where $W^I(E)$ is the averaged impact ionization rate and v_d is the drift velocity for a given electric field E. $W^I(E)$ is obtained from the ensemble average of $W^I(k)$ over the $k-$distribution function $f_E(k)$ under electric field. Instead of solving the Boltzmann equation for $f_E(k)$ directly, we use the balanced-energy relation to approximate it. The distribution function is assumed it to be in the form of a shifted Boltzmann distribution $f_E(k) = \exp\left[-\varepsilon_v(k - k^*)/(k_B T^*)\right]$, with two parameters k^* and T^* to be determined self-consistently. k^* is the wave number shift due to the electric field, and is related to the drift velocity v_d by $k^* = m_h v_d/\hbar$. m_h is the hole mass at $k = \pi/a$, the band maximum. The drift velocity v_d is related to the electric field E by $v_d = \mu E$, where the mobility μ is assumed to obey the Drude form $\mu = e\tau_{ph}/m_h$. τ_{ph} is the optical phonon emission life time. The effective temperature T^*, which is much larger than the surrounding lattice temperature at high field, is determined by the energy balanced equation $eEv_d = k_B T^*/\tau_{ph}$[70]. eEv_d is the Joule heating per unit time per unit volume provided by applied field, while $k_B T^*/\tau_{ph}$ is the thermal power transferred from the electron system to the lattice environment per unit volume. These two quantities must be balanced in steady state. We
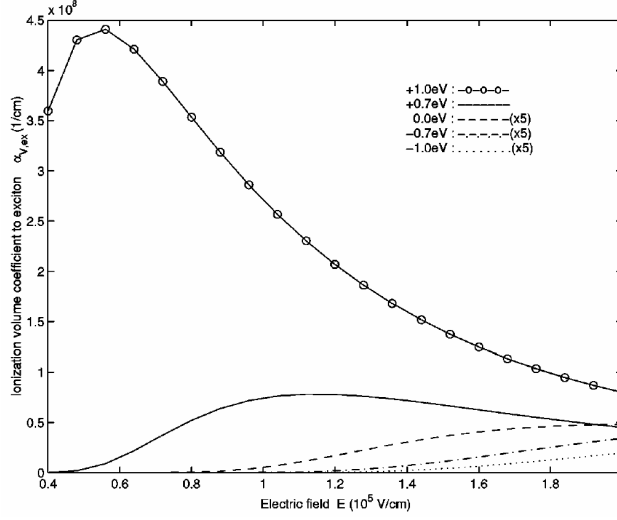
Figure 2.8: Impact ionization volume coefficient $\alpha_{V,ex}$ by a hot hole to exciton under electric field E. The rate grows rapidly as the deep level energy deviation $\Delta\varepsilon$ goes from -1.0 eV to $+1.0$ eV. In order to distinguish them, we magnify curves for -1.0 eV, -0.7 eV and 0.0 eV by 5 times.

assume that the all heat comes from optical phonons emitted by the hot holes accelerated by the applied electric field. As W^I discussed above, the impact ionization coefficient α is inversely proportional to the chain size N because there is only one defect on the chain. For convenience, we define the volume ionization coefficient α_V as αN, such that the actual ionization coefficient on the chain with many defects is equal to α_V times the defect density. $\alpha_{V,ex}$ and $\alpha_{V,e-h}$ for the production of excitons and free electron-hole pairs are shown in Fig. 2.8 and Fig. 2.9, respectively. The free carrier number decreases by one in the former process, and increases by one in the latter. Their difference $\alpha_{V,net}$, the net carrier production coefficient, is shown in Fig. 2.10. It is negative when $E \preceq 2 \times 10^5$ V/cm, for which the excitons are the predominant products of the defect impact ionization process, and the net carrier density decreases along the direction of the carrier drift . Light emission is expected from the radiative decay of the excitons.

2.4 Discussion

Defect Auger process is well known in inorganic semiconductors[71], but important only at high carrier densities due to the requirement of the proximity
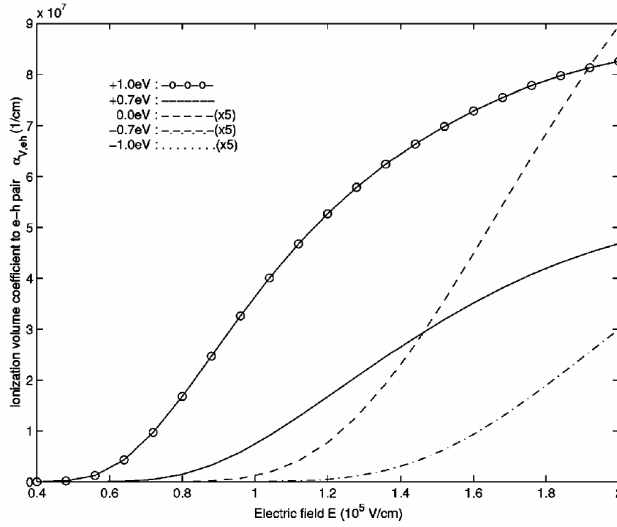
Figure 2.9: Impact ionization volume coefficient $\alpha_{V,e-h}$ to free electron-hole pair by a hot hole under electric field E.

of the second carrier when the first carrier is trapped by the defect. What is special about the similar process in conjugated polymer is that the large binding exciton energy guarantees that each carrier always has an oppositely charged second carrier bound to it and ready to take away relaxation energy, implying an effective high carrier density to facilitate the Auger process. Even though the idea is simple, such a mechanism for exciton dissociation without the need of the third carrier has never been discussed in the literature to our knowledge. Similarly, our prediction of the creation of a neural bound state instead of more free carriers by impact ionization is also completely new. These are both good examples that there exist many interesting new phenomena in organic semiconductors which are not common in their inorganic counterparts. Novel device operations taking advantage of these phenomena can be envisaged. For instance, exciton production via impact ionization leads to the possibility of light emission under unipolar (single carrier) injection with high field along the chain, i.e. a unipolar LED. When the carrier is accelerated by the field and gains enough kinetic energy to match the difference between the binding energy of the deep level and exciton, the threshold for exciton creation is reached. Our calculation shows that the ionization coefficient for the generation of excitons can be as high as 10^7 cm^{-1} times the number of defect per repeat unit when the electric is around 10^5 V/cm (Fig. 2.8). When the electric field is further increased the carrier becomes so energetic that the creation of another free carrier out of the defect
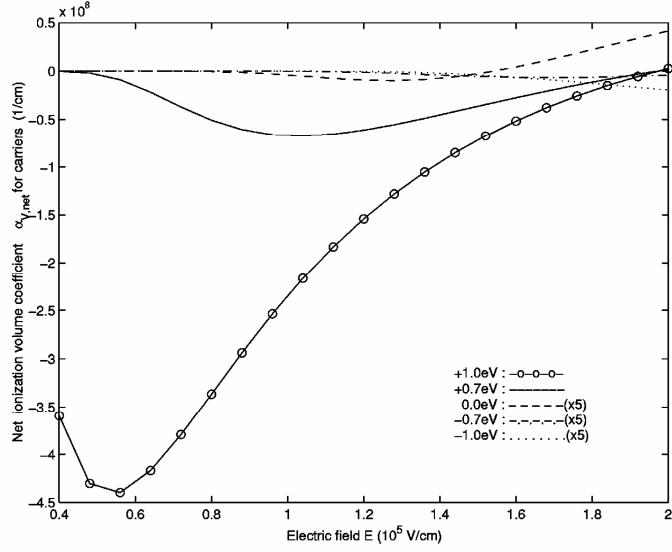
Figure 2.10: Volume coefficient $\alpha_{V,net}$ for the net carrier generation due to impact ionization. $\alpha_{V,net}$ is equal to $\alpha_{V,e-h} - \alpha_{V,ex}$ because the former produces one more carrier and the latter neutralizes the incident hole itself.

dominates the creation of excitons. Those carriers are expected to be driven away from each other under such high field and do not recombine to form excitons and emit light anymore. The unipolar light emission is therefore efficient only within a window of electric field. This peculiar behavior can be used as a direct way to verify our prediction experimentally. Such a high field along the chain can not be achieved in the conventional polymer LED with sandwich structure, in which the field is basically perpendicular to the chains. In order to realize this situation, electrodes parallel to the substrate and chain directions must be fabricated. In fact, if the field is high enough, exciton (and unipolar light emission) can be created directly from the ground state via impact ionization even without defects. This will be the subject of further study.

In this work we calculate only the rate by which the electron is captured while the hole is released as the free carrier, mainly because holes have been shown to the the dominant carriers for charge transport due to severe electron trapping in most conjugated polymers[23, 72]. The opposite case of electron release and hole trapping can be obtained in almost the same way with similar rate. Only singlet excitons are considered in this work, because the triplet excitons can neither be photo-excited nor emit light. The only difference for the corresponding rates for the triplet excitons is that the contribution from

the exchange part of the Coulomb interaction is cancelled.

There are many possible kinds of defects, either structural or chemical, with different binding energy and wavefunction. For example, the deep level associated with the chain twist varies from the midgap to the bandedge with the twist angle, while the level for oxygen (carbonyl group) is about 0.4 eV below the conduction band in the one-particle picture[63]. The deep level energy will depend on the occupancy if the Coulomb interaction is included. For the case of exciton dissociation by electron trapping, the initial occupation number of the deep level must be either zero or one(at least one vacancy for the electron to fall into). On the other hand, for the case of hole trapping the initial occupation number must be either one or two(at least one electron to drop into the hole). The impact inonization is just the reveres process of exciton dissociation. The energy of the deep level can be determined, in principle, by the Hartree-Fock self-consistent field. So when the deep level is occupied by one electron, the energy is higher than when the level is empty. Our calculations include all the cases by adjusting the deep level binding energy and the corresponding wavefunction. Results for deep levels from -1 eV to 1 eV measured from the midgap are shown in the figures. This range covers most of the deep levels revealed by the deep level transient spectroscopy[73]. As for the deep level at the midgap associated with the chain end, the discussion of impact ionization can not be properly applied. This is because the carrier, and the resulting exciton, can not travel beyond the chain end. However, the deep level associated with the chain end can still facilitate exciton dissociaton, because the exciton wavefunction is extended in the conjuagted segment and overlaps with the chain end deep level. The center-of-mass wavefunction of the exciton near the chain end should be more appropriately described by a standing wave (superposition of K and $-K$ states) instead of just a K state. However, according to our calculation the dissociation rate in symmetric under $K \leftrightarrow K$ inversion, so the result can still apply.
In calculating the impact ionization coefficient we assume that the wavefunction of the hot carrier interacts with many defects before the ionization, and each carrier experiences the same ionization rate irrespective of its position. The situation is similar to the case of the volume dissociation for exciton quenching. This can be justified because the high kinetic energy of the hot carriers makes them less likely to be localized by the disorder, so they can be described by the extended Bloch states. The excitons at thermal velocity, on the other hand, are much slower and more likely to be localized by disorders.

2.5 Conclusion

We obtain the defect Auger dissociation rate for excitons in conjugated polymers by calculating the matrix element of the Coulomb scattering among three band states and one defect state. Our results show that the defect Auger process is the dominant mechanism for exciton dissociation in EL and photocarrier generation for PC with excitation below the bandgap. The capture probability for an exciton passage through the defect is found to be close to one, consistent with the 1D diffusion model for luminescnece quenching with non-exponential PL decay. Impact ionization is studied as the reverse process. Exciton creation and the resulting light emission under unipolar carrier injection is predicted for electric field around 10^5V/cm.

Chapter 3

Enhancement of singlet exciton formation ratio in electroluminescent conjugated polymers by magnetic doping

3.1   Harvesting triplet exciton through inter-system crossing

The internal quantum yield η_{int} for electroluminescence (EL) of conjugated polymers, defined as the number of photons generated per injected electron-hole pair, is composed of three factors: $\eta_{int} = \eta_{ex}\eta_S\eta_r$. η_{ex} is the exciton formation ratio per injected pair, η_S is the recombination branching ratio through the spin singlet, and η_r is the singlet exciton radiative decay probability. η_r can be over 0.6 with improved material purity as suggested by photoluminescence efficiency[74], while η_{ex} can be increased by using multi-layer structures[1]. Therefore, η_S can be taken as the theoretical limit for η_{int}. Due to the weak spin-orbital coupling in carbon atom, it has been assumed that the Coulomb capture of an electron-hole pair to form an exciton is independent of the spin configuration[1, 23]. Considering spin statistics, one fourth of the electron-hole pairs become singlet excitons and three fourth become triplet. Because of the triplet exciton is lower in energy than the singlet for about 1 eV[75, 76], it is impossible for them to transfer back to the singlet before it decays either non-radiatively or through phosphorescence. This sets an upper bound on η_{int} at 1/4, much lower than the EL quantum yield achieved in inorganic semiconductors, and poses a serious constraint for the development of highly efficient light emitting polymer devices. Recently there have been experimental and theoretical works which suggest that the electron-hole recombination is spin-dependent [77–84]. In particular, η_S is found to be 0.57 for heavy-atom-containing polymers[85]. However, for the most promising polymers in light-emitting-diode applications, e.g. poly(p-phenylene vinylene) (PPV), polyfluorene(PFO) and their derivatives, there is no heavy atom in the backbone and a large proportion of triplet excitons is expected to form and seriously limits the efficiency. Doping of small-molecule triplet emitters containing heavy-atom has been used to harvest the triplet excitons[85]. However, the triplet emitters can only raise phosphorescence but not EL which results exclusively from the radiative decay of the singlet excitons. It is therefore highly desirable to identify a physical mechanism which redirects the triplet electron-hole pair into the singlet exciton and contributes to the EL efficiency.

In this paper we propose theoretically that a triplet electron-hole pair can be redirected into a singlet exciton by introducing transition metal complexes into the conjugated polymer films. The transition metal ion with partially filled d-shell carries a magnetic moment, which is coupled to the π-electrons in the conjugated polymer through the exchange interaction and causes intersystem crossing between the singlet and triplet excitons in the

polymer. With such magnetic doping the electron-hole capture and exciton formation process become spin-dependent and the upper limit of 1/4 for η_S can be lifted. The main effect of the magnetic moment is not to cause inter-system crossing between the lowest triplet and singlet exctions, but between the nearly degenerate second lowest triplet and singlet excitons. In fact, triplet excitons have to be intercepted and redirected into the singlet sector before it relaxes into the lowest triplet exciton, which is much lower than any other excitons due to the large exchange splitting[76]. The spin-dependent relaxation process is shown in Fig. 3.1. $S1$ and $T1$ are the lowest singlet and triplet excitons. $S2$ and $T2$ are the second lowest singlet and triplet excitons. $S1$ decays radiatively with probability η_r, while $T1$ decays mainly non-radiatively. The energy splitting around 1.5 eV between $T2$ and $T1$ is nine times larger than the optical phonon energy of 0.17 eV. So the relaxation between $T2$ and $T1$ is limited by the slow multi-phonon emission. In the presence of magnetic doping, the spin-forbidden channel between nearly degenerate $S2$ and $T2$ is opened, such that $T2$ excitons can make a transition to $S2$ then rapidly relax to $S1$ and decay radiatively. The transition from $S2$ to $T2$ is, however, negligible due to the fast relaxation from $S2$ to $S1$. $S1$ exciton may be also transformed to $T1$ by the dopants then decays non-radiatively. Therefore the quantum efficiency is the result of the competition between the two channels $T2 \rightarrow S2$ and $S1 \rightarrow T1$. Our calculation shows that there exists range of the doping density in which the singlet branching ratio η_S is considerably larger than 1/4.

In section 3.2, we formulate the Hamiltonian for the exchange interaction between π-electron in conjugated polymer and d-electron in the dopant. In section 3.2, we calculate the spin-flip matrix element and transition rate between singlet and triplet excitons. In section 3.4, we substitute the transition rates in section 3.3 into the rate equations for the spin-dependent exciton formation, and obtain the singlet branching ratio η_S as a function of the magnetic doping density. Discussion and conclusion are given in section 3.5 and 3.6, respectively.

3.2 Exchange interaction between extended π electrons and localized d electrons

We formulate the Hamiltonian for the exchange interaction between the π electron in conjugated polymer and the d electron in the dopant.

Ground State
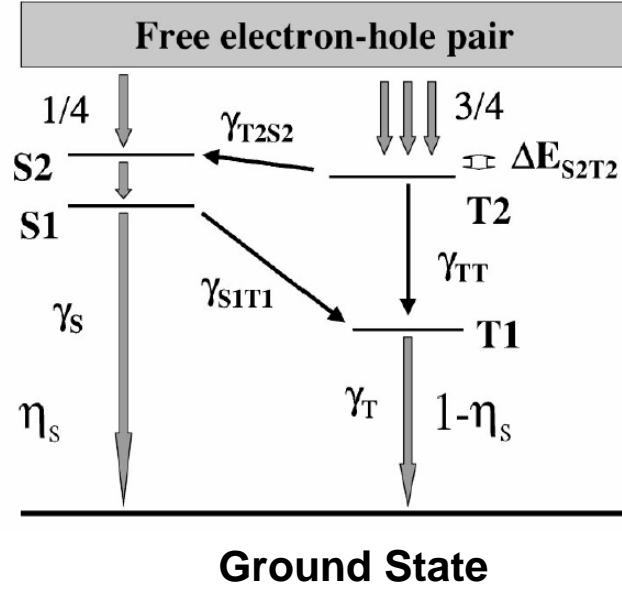
Figure 3.1: The energy levels and relaxation channels for the singlet excitons (S1,S2) and triplet excitons (T1,T2) are shown. The decay from S2 and S1 is so fast that S2 → T2 transition can be neglected. Due to the large energy splitting between S1 and T1, the T1 → S1 transition is also neglected.

3.2.1   Total Hamiltonian

The total Hamiltonian H for the π-electrons in one infinite conjugated polymer chain interacting with the d-electrons in the central metal ion of a transition metal complex close to the polymer backbone is

$$H = H_0 + H_d^{cry} + H^c, \quad H^c = H_d^c + H_\pi^c + H_{d\pi}^c \, . \tag{3.1}$$

Here H_0 is the single-particle part including the π-bands and the d-orbitals of a free metal ion. H_d^{cry} is the crystal field exerted on the metal ion by the surrounding ligands[86]. Spin-orbital interaction among the d-electrons is ignored in the presence of the relatively strong crystal field. H^c is the Coulomb interaction among the electrons in the π bands, and d-orbitals. It can be decomposed as three parts: H_d^c is the intra-atomic Coulomb interaction for the d-electrons, H_π^c the Coulomb interaction among π-electrons, and $H_{d\pi}^c$ is the Coulomb interaction between the d-electrons in the metal ion and the π-electrons in the conjugated polymer. We take $H_0 + H_d^{cry} + H_d^c + H_\pi^c$ as the unperturbed part whose eigenstates are the singlet and triplet excitons in conjugated polymers and a local magnetic moment in the metal ion. $H_{d\pi}^c$ is

taken as the perturbation which can exchange the spin between the exciton and the ion. H_0 can be expressed in second quantized form as

$$H_0 = \sum_{m=1,\sigma=\uparrow\downarrow}^{5} \varepsilon_{dm} a_{dm\sigma}^{\dagger} a_{dm\sigma} + \sum_{k,\lambda,\sigma=\uparrow\downarrow} \varepsilon_{k\lambda} a_{k\lambda\sigma}^{\dagger} a_{k\lambda\sigma} \ . \tag{3.2}$$

$m = 1, \cdots, 5$ is the quantum number for the five d-orbitals of the transition metal ion. k is the wave number for the Bloch states of π-electron in the conjugated polymer. The band index $\lambda = c, v$ stands for the conduction and valence band, respectively. Other bands are not included because they are irrelevant to the exciton wave functions. $\sigma =\uparrow, \downarrow$ is the spin index. ε_{dm} is the energy for the d-orbitals, and $\varepsilon_{k\lambda}$ is the π-electron energy band. $a_{dm\sigma}^{\dagger}$ and $a_{dm\sigma}$ are the creation and annihilation operators for the d-electrons. $a_{k\lambda\sigma}^{\dagger}$ and $a_{k\lambda\sigma}$ are for the π-electrons. They obey the anticommutation relation: $[a_{dm\sigma}, a_{dm\sigma}^{\dagger}]_+ = 1$ and $[a_{k\lambda\sigma}, a_{k\lambda\sigma}^{\dagger}]_+ = 1$. For a free transition metal ion, its total spin angular momentum quantum number S and orbital angular momentum quantum number L for the ground state are determined by the Hund's rules after H_d^c is included. The $(2S + 1) \times (2L + 1)$-fold degeneracy is only broken by the spin-orbital interaction. However, for an ion in the complex the orbital angular momentum is usually quenched by the crystal field H_d^{cry} due to the ligands, such that only $(2S + 1)$-fold spin degeneracy is left. The electronic configurations for the d-electrons depend on the ligand number and structure. For example, there are square and tetrahedron for four ligands, trigonal bipyramid for five, and octahedron for six.[86, 87] The level splitting for the case of octahedral crystal field is shown in Fig. 3.2. The magnitude of the splitting increases from left to right in the spectrochemical series for the ligands[87]: I$^-$ < Br$^-$ < Cl$^-$ < S^{2-} < F$^-$ < OH$^-$ < C$_2$O$_4{}^{2-}$ < H$_2$O < NH$_3$ < NO$_2{}^-$ < CN$^-$. The electronic configuration in the ligand-split d-shell is determined by minimum total energy, which is a compromise between crystal field splitting due to H_d^{cry} and Coulomb repulsion energy due to H_d^c. Assume that all the lower d-orbitals are occupied by one electron. If the splitting is less than the Coulomb repulsion energy between two electrons in the same orbital, the next electron will be filled into the higher level. This is the case of high spin(Fig. 3.2(a)). On the other hand if the splitting is larger than the Coulomb repulsion, the electron will be filled into the lower level to form electron pair with spin up and down. This is the case of low spin(Fig. 3.2(b)). For an isolated metal complex with n electrons in the d-shell, the total n-particle wave function $|\psi_d\rangle$ for the d-electrons with a given ligand field contains orbital and spin parts: $|\psi_d\rangle = \mathcal{A}(|n\rangle \otimes |S, M_S\rangle)$. $\mathcal{A}$ is the total antisymmetrization operator. $|n\rangle$ is the direct product of the single-particle wave functions $\phi_{dm_1}, \cdots, \phi_{dm_5}$ of the occupied d-orbitals. The
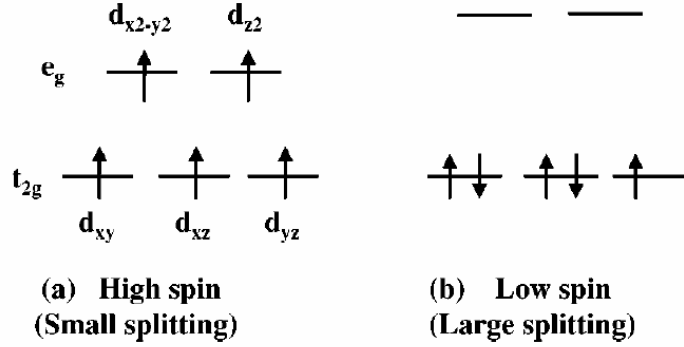
Figure 3.2: Energy splitting and electron configuration for a metal ion with five d-electrons in octahedral ligand crystal field: (a) high spin, (b) low spin.

occupation is determined by H_d^{cry} and H_d^c. $|S, M_S\rangle$ is the spin eigenfunction, which can be written as the superposition of basis states $|s_1, s_2, \ldots, s_n\rangle$. $s_i = \uparrow, \downarrow$ is the spin index for the i-th electron. $|\psi_d\rangle$ will be later expressed in second quantized form.

3.2.2 Exchange Hamiltonian

So far the Coulomb interaction $H_{d\pi}^c$ between π- and d-electrons is not considered. $H_{d\pi}^c$ is a part of the total Coulomb interaction H^c. In second quantized form H^c can be written as

$$H^c = \frac{1}{2} \int \int d^3\mathbf{r}_1 d^3\mathbf{r}_2 \hat{\psi}^\dagger(\mathbf{r}_1)\hat{\psi}^\dagger(\mathbf{r}_2)V(\mathbf{r}_1, \mathbf{r}_2)\hat{\psi}(\mathbf{r}_2)\hat{\psi}(\mathbf{r}_1) , \qquad (3.3)$$

with

$$\hat{\psi}(\mathbf{r}) = \sum_{m,\sigma} \phi_{dm}(\mathbf{r})a_{dm\sigma} + \sum_{k,\lambda,\sigma} \psi_{k\lambda}(\mathbf{r})a_{k\lambda\sigma} . \qquad (3.4)$$

$V(\mathbf{r}_1, \mathbf{r}_2) = e^2/(4\pi\epsilon\epsilon_0|\mathbf{r}_1 - \mathbf{r}_2|)$ is the Coulomb interaction between electrons, $\epsilon = 2.5$ is the relative dielectric constant of conjugated polymer,[67, 77], $\phi_{dm}(\mathbf{r})$ is the single-particle wave function of the d-electrons and $\psi_{k\lambda}(\mathbf{r})$ is the single-particle wave function of the π-electrons. After substituting Eq.(3.4) into Eq.(3.3) H^c can be organized as $H^c = H_d^c + H_\pi^c + H_{d\pi}^c$. H_d^c has been included when we consider the electronic configuration of the metal ion above. H_π^c will be included latter when we consider the exciton wave function. $H_{d\pi}^c$ is the summation of the terms having one pair of creation and annihilation operators for both d-electron and π-electron. Now we focus on $H_{d\pi}^c$, which can be separated into two parts[88]

$$
\begin{aligned}
H_{d\pi}^c &= \sum_{kk'mm'\sigma\sigma'} \langle k'm'|V|km\rangle a_{k'\sigma}^\dagger a_{dm'\sigma'}^\dagger a_{k\sigma} a_{dm\sigma'} \\
&\quad - \sum_{kk'mm'\sigma\sigma'} \langle k'm'|V|mk\rangle a_{k'\sigma}^\dagger a_{dm'\sigma'}^\dagger a_{k\sigma'} a_{dm\sigma} ,
\end{aligned}
\tag{3.5}
$$

where

$$
\langle k'm'|V|km\rangle = \int\int d^3\mathbf{r}_1 d^3\mathbf{r}_2 \psi_{k'}^*(\mathbf{r}_1)\phi_{dm'}^*(\mathbf{r}_2-\mathbf{R}_d)V(\mathbf{r}_1,\mathbf{r}_2)\phi_{dm}(\mathbf{r}_2-\mathbf{R}_d)\psi_k(\mathbf{r}_1) ,
\tag{3.6}
$$

$$
\langle k'm'|V|mk\rangle = \int\int d^3\mathbf{r}_1 d^3\mathbf{r}_2 \psi_{k'}^*(\mathbf{r}_1)\phi_{dm'}^*(\mathbf{r}_2-\mathbf{R}_d)V(\mathbf{r}_1,\mathbf{r}_2)\phi_{dm}(\mathbf{r}_1-\mathbf{R}_d)\psi_k(\mathbf{r}_2) .
\tag{3.7}
$$

The band index λ is neglected for simplicity. $\mathbf{R}_d$ is the position of the nucleus of the metal ion. The first summation of Eq.(3.5) is the direct Coulomb term $H_{d\pi}^d$ which conserves the spin for both the d and π electrons. The second summation is the exchange term $H_{d\pi}^{ex}$ in which the spins of d-electron and π-electron are exchanged(Fig. 3.3). Since we are interested in the process involving spin-flip, only the exchange term will be considered. Omitting $m \neq m'$ terms in $H_{d\pi}^{ex}$ due to smaller wave functions overlap, we collect $m' = m$ terms in Eq.(3.5) and carry out the spin summation to have

$$
\begin{aligned}
H_{d\pi}^{ex} &\simeq -\sum_{kk'm} \langle k'm|V|mk\rangle \Big[(a_{k'\uparrow}^\dagger a_{k\uparrow} - a_{k'\downarrow}^\dagger a_{k\downarrow})(\tfrac{1}{2}a_{dm\uparrow}^\dagger a_{dm\uparrow} - \tfrac{1}{2}a_{dm\downarrow}^\dagger a_{dm\downarrow}) \\
&\quad + a_{k'\downarrow}^\dagger a_{k\uparrow} a_{dm\uparrow}^\dagger a_{dm\downarrow} + a_{k'\uparrow}^\dagger a_{k\downarrow} a_{dm\downarrow}^\dagger a_{dm\uparrow}\Big] .
\end{aligned}
\tag{3.8}
$$

Replacing $\langle k'm|V|mk\rangle$ by their summation $V_{k'k}$ over m, $H_{d\pi}^{ex}$ can be further approximated as

$$
\begin{aligned}
H_{d\pi}^{ex} &\simeq -\sum_{kk'} V_{k'k}\left[(a_{k'\uparrow}^\dagger a_{k\uparrow} - a_{k'\downarrow}^\dagger a_{k\downarrow})S_{dz} + a_{k'\downarrow}^\dagger a_{k\uparrow}S_{d+} + a_{k'\uparrow}^\dagger a_{k\downarrow}S_{d-}\right] , \\
&= -\sum_{kk'} V_{k'k}(a_{k'\uparrow}^\dagger a_{k'\downarrow}^\dagger)\mathbf{S}_\pi \begin{pmatrix} a_{k\uparrow} \\ a_{k\downarrow} \end{pmatrix} \cdot \mathbf{S}_d .
\end{aligned}
\tag{3.9}
$$

The total d-electron spin operators are defined as

$$
S_{dz} = \sum_m a_{m\uparrow}^\dagger a_{m\uparrow} - a_{m\downarrow}^\dagger a_{m\downarrow} , \; S_{d+} = \sum_m a_{m\uparrow}^\dagger a_{m\downarrow} , \; S_{d-} = \sum_m a_{m\downarrow}^\dagger a_{m\uparrow} .
\tag{3.10}
$$
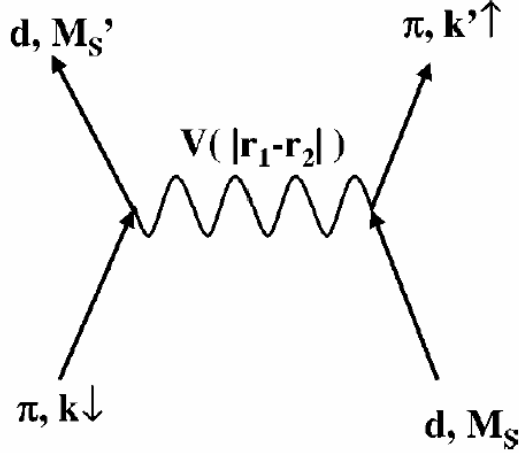
Figure 3.3: In the exchange interaction the Bloch electron in the polymer is scattered from k to k' with spin flip. There is a corresponding change in the magnetic quantum number of local moment from M_S to $M'_S = M_S - 1$.

$\mathbf{S}_\pi$ are two times the Pauli matrices.

In order to calculate the exchange integral in Eq.(3.7) we need the explicit form of the single-particle wave functions. For d-electrons we consider the quite common octahedral ligand structure, for which the five d-orbitals split into three t_{2g} orbitals and two e_g orbitals. They are labelled as $d_{xy} \to d1$, $d_{xz} \to d2$, $d_{yz} \to d3$ for t_{2g}; and $d_{x^2-y^2} \to d4$, $d_{z^2} \to d5$ for e_g. The x-y-z axes are defined by the ligands introduced below. We use hydrogenic wave function with atomic number adjusted to fit the correct ion size. For π-electrons we consider the tight-binding model for a PPV chain. The Bloch state $\psi_k(\mathbf{r})$ is expanded by the carbon atomic orbitals as

$$\psi_k(\mathbf{r}) = \sum_n e^{ikna} \phi_k(\mathbf{r} - \mathbf{R}_n) \ , \ \ \phi_k(\mathbf{r}) = \sum_{i=1}^{8} b_i(k)\psi_i(\mathbf{r}). \qquad (3.11)$$

n is the index for unit cell, $a = 6.5$Å is the lattice constant, $\mathbf{R}_n$ is the lattice point for the n-th unit cell, and $\phi_k(\mathbf{r})$ is the linear combination of the eight $2p_z$ orbitals $\psi_i(\mathbf{r})$ with coefficient $b_i(k)$. $i = 1, \cdots, 8$ is the index for carbon atoms in the repeat unit as labelled in Fig. 3.4. The energy band $\varepsilon_\lambda(k)$ and the coefficient $b_i(k)$ are calculated by diagonalizing the 8×8 matrix in tight binding method. The off-diagonal resonant integral for the bonds are indicated in Fig. 3.4. t is the resonance integral for the phenyl bond, t_1 for the single bond, and t_2 for the double bond. We use $t = -3.1$ eV, $t_1 = -2.2$ eV, and $t_2 = -3.0$ eV to fit the energy gap 2.8 eV for PPV. There are totally
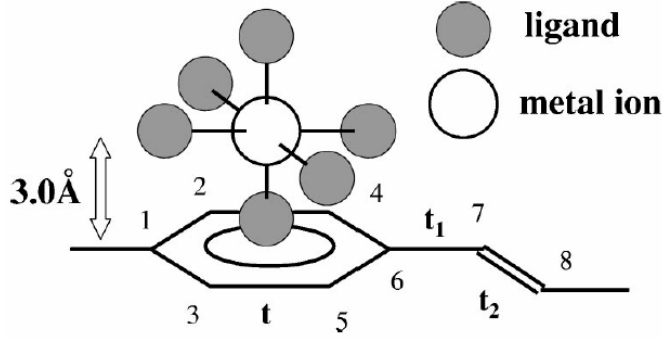
Figure 3.4: The chemical structure and resonance integrals t, t_1, and t_2 of PPV repeat unit are labeled. The relative position of the metal complex and the polymer is shown. The vertical distance between the ion nucleus and the polymer plane is 3.0 Å. The orbitals for d_{xy}, d_{xz}, and d_{yz} can stretch out of the ligands to interact with the p_z orbit of the carbon atom on the polymer chain.

eight bands. We need only the states of the conduction and valence bands.

3.3 Spin-Flip transition

We calculate the spin-flip matrix element and transition rate between singlet and triplet excitons

3.3.1 Free carrier spin flip

In the calculation below we consider an octahedral complex with five d-electrons in the central ion. The total wave function of the ion is an simultaneous eigenstate of $\mathbf{S}_d^2$ and S_{dz}, and is assumed to be in the high spin configuration $S = 5/2$. In order to flip the spin for the π-electron in the conduction band, magnetic quantum number m of the d-electron must decrease or increase by one in order to satisfy the total spin conservation. We consider the transition from $|S = 5/2, M_S = 5/2\rangle$ to $|S = 5/2, M_S' = 3/2\rangle$ first. In occupation number representation, the initial state for the combined system including π- and d-electron is

$$|S = \frac{5}{2}, M_S = \frac{5}{2}, k \downarrow\rangle = \mathcal{A}[\,|\uparrow, \uparrow, \uparrow, \uparrow, \uparrow\rangle \otimes |k \downarrow\rangle\,] = a_{d1\uparrow}^\dagger a_{d2\uparrow}^\dagger a_{d3\uparrow}^\dagger a_{d4\uparrow}^\dagger a_{d5\uparrow}^\dagger a_{k\downarrow}^\dagger |0\rangle\,.$$

$$(3.12)$$

The final state is

$$
\begin{aligned}
| \quad & S = \frac{5}{2}, M_S = \frac{3}{2}, k' \uparrow \rangle \\
= \quad & \mathcal{A}[\, \frac{1}{\sqrt{5}} (|\downarrow,\uparrow,\uparrow,\uparrow,\uparrow\rangle + |\uparrow,\downarrow,\uparrow,\uparrow,\uparrow\rangle + |\uparrow,\uparrow,\downarrow,\uparrow,\uparrow\rangle \\
& + |\uparrow,\uparrow,\uparrow,\downarrow,\uparrow\rangle + |\uparrow,\uparrow,\uparrow,\uparrow,\downarrow\rangle) \otimes |k' \uparrow\rangle \,] \\
= \quad & \frac{1}{\sqrt{5}} (a^\dagger_{d1\downarrow} a^\dagger_{d2\uparrow} a^\dagger_{d3\uparrow} a^\dagger_{d4\uparrow} a^\dagger_{d5\uparrow} + a^\dagger_{d1\uparrow} a^\dagger_{d2\downarrow} a^\dagger_{d3\uparrow} a^\dagger_{d4\uparrow} a^\dagger_{d5\uparrow} + a^\dagger_{d1\uparrow} a^\dagger_{d2\uparrow} a^\dagger_{d3\downarrow} a^\dagger_{d4\uparrow} a^\dagger_{d5\uparrow} \\
& + a^\dagger_{d1\uparrow} a^\dagger_{d2\uparrow} a^\dagger_{d3\uparrow} a^\dagger_{d4\downarrow} a^\dagger_{d5\uparrow} + a^\dagger_{d1\uparrow} a^\dagger_{d2\uparrow} a^\dagger_{d3\uparrow} a^\dagger_{d4\uparrow} a^\dagger_{d5\downarrow}) a^\dagger_{k'\uparrow} |0\rangle \, .
\end{aligned}
$$

Here $|S, M_S, k\sigma\rangle$ is the total wave function with total spin S and magnetic quantum number M_S for d-electron, wave number k and spin σ for conduction band π-electron. $|\sigma_1, \sigma_2, \sigma_3, \sigma_4, \sigma_5\rangle$ with $\sigma_i = \uparrow$ or $\downarrow$ is the direct product of five d-electron with d_{xy} having spin σ_1, d_{xz} spin σ_2, d_{yz} spin σ_3, $d_{x^2-y^2}$ spin σ_4, and d_{z^2} spin σ_5. $|0\rangle$ is the filled valence band. Using the explicit form of $H^{ex}_{d\pi}$ in Eq.(3.5-3.7), we can obtain the matrix element $\langle 5/2, 3/2, k' \uparrow | H^{ex}_{d\pi} | 5/2, 5/2, k \downarrow\rangle$. After certain algebra for the Fermion operators, the result for other initial m can be obtained by similar procedure as above in principle. A simpler way is to exploit the rotation symmetry in spin space and relate them to the result for $M_S = 5/2$ and $M'_S = 3/2$. Using Eq.(3.9), we have

$$
\langle \frac{5}{2}, M'_S, k' \uparrow | H^{ex}_{d\pi} | \frac{5}{2}, M_S, k \downarrow\rangle \;=\; V_{kk'} \langle \frac{5}{2}, M'_S | S_{d-} | \frac{5}{2}, M_S\rangle \qquad (3.13)
$$

for any M_S, M'_S. The spin matrix element is $\langle S, M_S \pm 1 | S_{d\pm} | S, M_S\rangle = \sqrt{(S \mp M_S)(S \pm M_S + 1)}$. The value for $V_{kk'}$ is independent of the angular momentum quantum number for d-electron and π-electron. For given π-electron initial state $|k, \sigma\rangle$ and $|k', \sigma'\rangle$, the transition matrix element for all d-electron initial and final moment, M_S and M'_S, can be obtained through Eq.(3.13) once any one of them is calculated by performing the exchange integral in Eq.(3.7). For the spin-flip of holes, we can simply replace the conduction band creation operator by the valence band annihilation operator.

3.3.2   Transition rate between singlet and triplet excitons

The wave functions for the lowest (S1,T1) and second lowest (S2,T2) singlet and triplet excitons can be expanded by electron-hole pairs as[66]

$$|S1(2)\rangle = \sum_{k_e,k_h} S_{1(2)}(k_e, k_h)(|k_{e\uparrow}, k_{h\uparrow}\rangle + |k_{e\downarrow}, k_{h\downarrow}\rangle), \qquad (3.14)$$

$$|T1(2)_{-1}\rangle = \sum_{k_e,k_h} T_{1(2)}(k_e, k_h)(|k_{e\downarrow}, k_{h\uparrow}\rangle), \qquad (3.15)$$

$$|T1(2)_0\rangle = \sum_{k_e,k_h} T_{1(2)}(k_e, k_h)(|k_{e\uparrow}, k_{h\uparrow}\rangle - |k_{e\downarrow}, k_{h\downarrow}\rangle), \qquad (3.16)$$

$$|T1(2)_{+1}\rangle = \sum_{k_e,k_h} T_{1(2)}(k_e, k_h)(|k_{e\uparrow}, k_{h\downarrow}\rangle), \qquad (3.17)$$

where $|k_{e\,\sigma}, k_{h\,\sigma'}\rangle = a^\dagger_{k_e c\sigma} a_{-k_h v -\sigma'}|0\rangle$ is the electron-hole pair wave function. $S^{1(2)}(k_e, k_h)$ and $T^{1(2)}(k_e, k_h)$ are the exciton envelope functions. The exciton wave functions are exponential in the real space, so in terms of the total wave number of exciton $K = k_e + k_h$ we approximate their momentum space envelope functions as Lorentzians[66]

$$S_1(k_e, k_h = K - k_e) = \frac{2}{a_{S1}\sqrt{N a_{S1} a}}\left[\left(\frac{1}{a_{S1}}\right)^2 + \left(k_e - \frac{\pi}{a} - \frac{w_{ex}}{w_v}K\right)^2\right]^{-1},$$

$$T_1(k_e, k_h) = \frac{2}{a_{T1}\sqrt{N a_{T1} a}}\left[\left(\frac{1}{a_{T1}}\right)^2 + \left(k_e - \frac{\pi}{a} - \frac{w_{ex}}{w_v}K\right)^2\right]^{-1}.$$

N is the number of the repeat units, $w_c = 2.0$ eV and $w_v = 2.3$ eV[76] are the band width for conduction and valence band, respectively. $w_{ex} = 1/(1/w_c + 1/w_v) = 1.07$ eV the width of the exciton band. $a_{S1} = 20$ Å[89] is the Bohr radius for the lowest singlet state, $a_{T1} = 13$ Å for the lowest triplet state. $T_2(k_e, k_h)$ is obtained from $T_1(k_e, k_h)$ by replacing a_{T1} by $a_{T2} = 30$ Å, then taking the partial derivative with k_e with proper normalization. The result is

$$T_2(k_e, k_h) = \frac{2}{a_{T2}^2}\sqrt{\frac{2}{N a_{T2} a}}\frac{-2\left(k_e - \frac{\pi}{a} - \frac{w_{ex}}{w_v}K\right)}{\left[\left(\frac{1}{a_{T2}}\right)^2 + \left(k_e - \frac{\pi}{a} - \frac{w_{ex}}{w_v}K\right)^2\right]^2}. \qquad (3.18)$$

Due to the exchange energy for the π-electrons, $S1$ is higher than $T1$ so a_{T1} is smaller than a_{S1}. Exchange energy does not cause energy splitting between $S2$ and $T2$ within single-configuration-interaction approximation[90], and there is near degeneracy between them. We take their Bohr radius and wave functions to be the same, i.e. $S_2(k_e, k_h) = T_2(k_e, k_h)$.

With the expressions for the singlet and triplet excitons in terms of electron-hole pairs and the transition matrix element for the free carriers

in the last section, the intersystem crossing rate between triplet and singlet excitons, $W_{S1T1}(K_{S1})$ and $W_{T2S2}(K_{T2})$, can be calculated from Fermi Golden rule

$$
\begin{aligned}
&W_{S1T1}(K_{S1}) = \\
&\frac{2\pi}{\hbar}\frac{1}{6}\sum_{M_S=-5/2}^{5/2}\sum_{K_{T1}}\sum_{\Delta M_S=\pm 1}|\langle M_S + \Delta M_S, T1_M|H_{d\pi}^{ex}|M_S, S1\rangle|^2\,\delta\left[E(K_{S1}) - E(K_{T1})\right]\ , \\
&W_{T2S2}(K_{T2}) = \\
&\frac{2\pi}{\hbar}\frac{1}{6}\sum_{M_S=-5/2}^{5/2}\sum_{K_{S2}}\sum_{\Delta M_S=\pm 1}|\langle M_S + \Delta M_S, S2|H_{d\pi}^{ex}|M_S, T2_M\rangle|^2\delta\left[E(K_{T2}) - E(K_{S2})\right]\ .
\end{aligned}
$$

$M = 0, \pm 1$ is the magnetic quantum number of the triplet exciton. The results are independent of M. $1/6$ is due to average over M_S. K_{S1}, K_{S2}, K_{T1}, and K_{T2} are total wave numbers of the corresponding excitons. The exciton energy dispersions are $E_{S1}(K) = E_{S1} + w_{ex}/2 + (w_{ex}/2)\cos(Ka)$, $E_{S2}(K) = E_{S2} + w_{ex}/2 + (w_{ex}/2)\cos(Ka)$, $E_{T1}(K) = E_{T1} + w_{ex}/2 + (w_{ex}/2)\cos(Ka)$, and $E_{T2}(K) = E_{T2} + w_{ex}/2 + (w_{ex}/2)\cos(Ka)$. E_{S1} =2.4 eV[76], E_{S2} =2.8 eV, E_{T1} =1.5 eV, and E_{T2} =2.7 eV are the the minimum energy for each exciton band measured from the ground state. W_{S1T1} and W_{T2S2} are inversely proportional to the number of repeat units N in the chain because there is only one dopant for the whole chain. In practice, there are many dopants and the transition rate γ_{S1T1} and γ_{T2S2} are equal to W_{S1T1} and W_{T2S2} times the number of dopants in the chain NN_d. The doping density N_d is the average number of dopant per repeat unit. For convenience, we define two chain size independent volume transition rates $w_{S1T1} \equiv W_{S1T1}N$ and $w_{T2S2} \equiv W_{T2S2}N$. The actual transition rates can be expressed as $\gamma_{T2S2} = w_{T2S2}N_d$, $\gamma_{S1T1} = 3w_{S1T1}N_d$. The factor of 3 is due to the three possible final states with equal rate. At finite temperature, we need to make a thermal average over the exciton wave numbers K for the initial state

$$
\gamma_{S1T1}(T) = \frac{\sum_{K_{S1}} e^{-\beta E_{S1}(K_{S1})}\gamma_{S1T1}(K_{S1})}{\sum_{K_{S1}} e^{-\beta E_{S1}(K_{S1})}}\ , \tag{3.19}
$$

and

$$
\gamma_{T2S2}(T) = \frac{\sum_{K_{T2}} e^{-\beta E_{T2}(K_{T2})}\gamma_{T2S2}(K_{T2})}{\sum_{K_{T2}} e^{-\beta E_{T2}(K_{T2})}}\ . \tag{3.20}
$$

β is $1/k_B T$, k_B is Boltzmann constant and T is the temperature.

We take the position $\mathbf{R}_d$ of the central metal ion in the dopant to be right above the center of the phenyl ring. The rate does not change significantly as $\mathbf{R}_d$ moves horizontally with fixed vertical distance from the chain.

In practice the vertical distance R_d between the metal ion and the polymer plane depends, of course, on the size of the ligands surrounding the metal ion. For large ligands it is impossible for the wave function of the metal d-electron and the polymer π-electrons to overlap and have exchange coupling. So we concentrate on the case of metal complexes with smaller ligands like halogen atoms like $MnCl^{-4}$. In order to show the strong effect of R_d on the exchange coupling, we plot in Fig. 3.5 the system-size independent exchange integral $NV_{k,k'}$ with $k = k' = 0$ and the volume intersystem crossing rate w_{T2S2} as a function of R_d. The exchange integral $NV_{0,0}$ varies from 0.2 eV to 0.08 eV as R_d increase from 1.5 Å to 2 Å. This is close to exchange integral of 0.18 to 0.26 eV for the substitutional magnetic ion in inorganic semiconductors[91] whose bond length is around 2 Å. In our case the dopant is not chemically bonded to the polymer chain and the distance is larger. As R_d increases and the wave function overlap diminishes both $NV_{0,0}$ and w_{T2S2} decay exponentially as expected. For the small ligand complexes the size of the whole complex is around 3-4 Å, so in the following we take R_d to be fixed at 3 Å unless otherwise specified. For R_d beyond 3.5 Å the effect of the dopant becomes negligible. In Fig. 3.6, the thermally averaged intersystem crossing rates γ_{S1T1} and γ_{T2S2} are shown as a function of temperature for various ΔE_{S2T2}. $\gamma_{T2S2}(T)$ increases as T increases or ΔE_{S2T2} decreases because more carriers can be thermally excited above the small barrier between $S2$ and $T2$. It is generally agreed that the energy splitting between $T2$ and $S2$ is smaller than 0.1 eV, but there is an uncertainty on its actual value since it is difficult to be measured directly. When ΔE_{S2T2} is below 0.05 eV, $\gamma_{T2S2}(T)$ becomes higher than $\gamma_{S1T1}(T)$. Larger $\gamma_{T2S2}(T)$ will cause more T2 $\rightarrow$ S2 $\rightarrow$ S1 transition which increases the efficiency, as discussed in the next section.

3.4 Rate equations and the singlet formation ratio

We substitute the transition rates in section 3.3 into the rate equations for the spin-dependent exciton formation, and obtain the singlet branching ratio η_S as a function of magnetic doping density

Using the intersystem crossing rates in the last section, we can formulate a set of spin-dependent rate equations for exciton formation and calculate the singlet formation ratio η_S. The intersystem crossing rate from $S2$ to $T2$ is much smaller than the spin and one-phonon allowed sub-picosecond relaxation from $S2$ to $S1$[92]. So $S2$ to $T2$ transition can be neglected in the rate equations. The rate from $T1$ to $S1$ is also negligible because $S1$ is
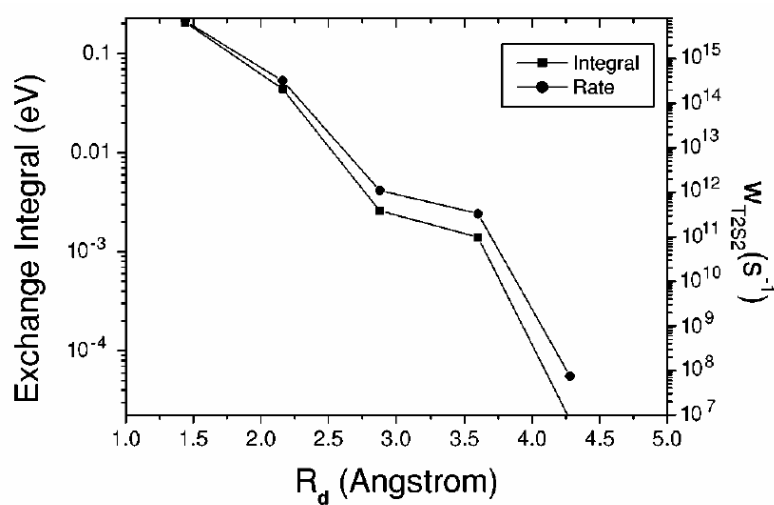
Figure 3.5: The effect of the metal-polymer distance R_d on the strength of the exchange coupling is shown. Both the exchange integral and the resulting intersystem crossing rate w_{T2S2} decrease exponentially as R_d increases due to reduced wavefunction overlap. For w_{T2S2} the temperature is 300K, there is no energy splitting between S2 and T2 levels, and the total spin S of the metal ion is 5/2.
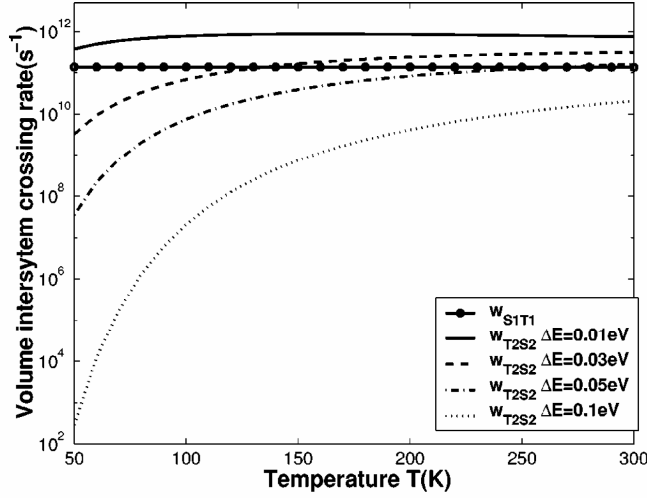
Figure 3.6: The volume intersystem crossing rate w_{S1T1} and w_{T2S2} for various T2/S2 energy splitting ΔE_{S2T2} are plotted as functions of temperature T. The total spin quantum number S for the metal ions is assumed to be 5/2. The actual transition rate is the volume rate times the number of dopant per repeat unit. w_{S1T1} is independent of T because the T1/S1 energy splitting is much large than the thermal energy.

much higher in energy[75, 76]. Due to the fast relaxation between $S2$ and $S1$ there is no need to distinguish them in the rate equation. So the total singlet exciton density is labeled as N_S. N_{T2} and N_{T1} are the densities for $T2$ and $T1$ triplet excitons.

The considerations in the previous sections are restricted to one single perfect polymer chain. In practice, the number of repeat unit N_c of a conjugation segment is about ten[93]. Instead of delocalized in an infinite perfect chain, the excitons hop among the conjugation segments due to the Forster or Dexter energy transfer mechanisms. The time scale τ_{tr} for the transfer is sub-picosecond[92]. For an exciton in a conjugation segment with $N_c = 10$ and containing a dopant, the intersystem crossing time is about $10/w_{T2S2} \sim 100$ ps, which is much slower than the transfer time. In other words, the excitons experience many segments and sample an averaged doping concentration. Consider a finite time Δt which is much longer than τ_{tr} but much shorter than the intersystem crossing time. Within Δt the excitons visit $\Delta t/\tau_{tr}$ of conjugation segments. For each segment the probability that there is a dopant is $N_c N_d$. If the exciton is in one such segment, the probability that it makes an intersystem crossing is $\tau_{tr} w/N_c$. So the

probability ΔP that an exicton makes an intersystem crossing within Δt is $(\Delta t / \tau_{tr})(N_c N_d)(\tau_{tr} w / N_c) = N_d w \Delta t$. Therefore the averaged effective intersystem crossing rate is $\Delta P / \Delta t = w N_d$, irrespective of the conjugation length N_c. The relation $\gamma = w N_d$ in the previous section between the actual intersystem crossing rate γ and the volume rate w is thus justified for a film of many polymer chains with finite conjugation length. The above consideration is not valid if the doping is so low that many excitons do not have the chance change to encounter a dopant before they decay. The exciton diffusion volume is l_{ex}^3, where l_{ex} is the exciton diffusion length and v is the primitive cell volume. The singlet exciton diffusion length is about 100 Å[94]. so we can take it as the lower bound for the diffusion length of the longer-lived triplet exciton. There are totally l_{ex}^3 / v repeat units in the diffusion length. The probability q that at least one of the repeat units contains a dopant is $1 - \exp(-N_d l_{ex}^3 / v)$. Effectively this corresponds to a modification $\gamma_{T2S2} \to q\gamma_{T2S2}$ for the intersystem crossing rate. q is actually almost equal to one for the physically interested doping regime. Finally the rate equations for the exciton densities in a realistic polymer film are

$$\frac{d}{dt} N_S = \frac{1}{4} G + q\gamma_{T2S2} N_{T2} - \gamma_S N_S - \gamma_{S1T1} N_S , \qquad (3.21)$$

$$\frac{d}{dt} N_{T2} = \frac{3}{4} G - \gamma_{TT} N_{T2} - q\gamma_{T2S2} N_{T2} , \qquad (3.22)$$

$$\frac{d}{dt} N_{T1} = \gamma_{TT} N_{T2} + \gamma_{S1T1} N_S - \gamma_T N_{T1} . \qquad (3.23)$$

γ_S is the singlet exciton decay rate. γ_T is the triplet exciton decay rate. G is the rate of the initial electron-hole capture which is assumed to be spin-independent. So one quarter of the electron-hole pairs become $S2$, and three quarters become $T2$ initially. There are then two possible ways to go from T2. The first is T2 $\to$ T1, the second is T2 $\to$ S2 $\to$ S1. The branching ratio between the above two ways is equal to the ratio of their rates $\gamma_{T2S2}/\gamma_{TT}$. Because the T2/T1 energy splitting around 1.5 eV is nine times larger than the optical phonon energy 0.17 eV, there is expected to be a phonon bottleneck[77] between T2 and T1 and the rate γ_{TT} can be as low as 2.7×10^8 s^{-1}. There is therefore the chance to control the branching ratio by raising γ_{T2S2} above γ_{TT} through magnetic doping. As for the S2 exciton, there are also two possible ways to go. The first is S2 $\to$ S1 $\to$ ground state, and the second is S2 $\to$ S1 $\to$ T1. The magnetic doping enhances the second possibility. The ratio R_{TS} between recombination through the triplet and singlet is given by $[\gamma_T N_{T1}]/[\gamma_S N_S]$, which can be obtained from steady state solution of the rate equation
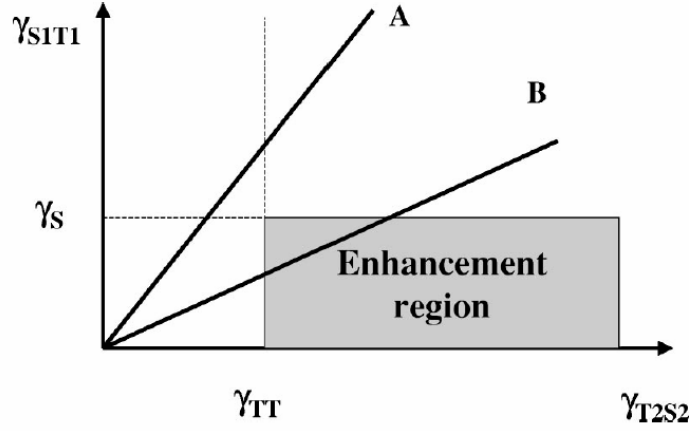
Figure 3.7: γ_{T2S2} and γ_{S1T1} have to be in the shaded region in order to raise the singlet formation ratio η_S. The straight lines A and B are mapped by changing the doping density N_d. Only in the case of line B there is a doping region for which the net effect of magnetic dopants is positive to the yield.

$$R_{TS} \equiv \frac{\gamma_T N_{T1}}{\gamma_S N_S}$$

$$= \frac{\frac{3}{4}\left(1 + q\gamma_{T2S2}/\gamma_{TT}\right)^{-1}}{\left\{\frac{1}{4} + \frac{3}{4}[1 + \gamma_{TT}/(q\gamma_{T2S2})]^{-1}\right\}\left(1 + \gamma_{S1T1}/\gamma_S\right)^{-1}} + \frac{\left(1 + \gamma_S/\gamma_{S1T1}\right)^{-1}}{\left(1 + \gamma_{S1T1}/\gamma_S\right)^{-1}} \ .$$

The singlet recombination branching ratio η_S is related to R_{TS} by $\eta_S = 1/(1 + R_{TS})$. $\eta_S = 1/4(R_{TS} = 3)$ if there is no intersystem crossing. If intersystem crossing is introduced by magnetic doping, η_S will deviate from 1/4. In order to redirect the triplet electron-hole pair into the singlet exciton, two requirements need to be satisfied: $\gamma_{T2S2} > \gamma_{TT}$ and $\gamma_{S1T1} < \gamma_S$. The former condition makes the redirection from $T2$ to $S2$ possible, while the latter condition ensures that most of the $S1$ excitons do not decay non-radiatively through the intersystem crossing to $T1$. γ_{TT} and γ_S are intrinsic material parameters, while γ_{T2S2} and γ_{S1T1} are proportional to the density N_d of the magnetic doping. Increasing the doping density favors the former requirement but disfavors the latter. One of the main purposes of our theoretical calculation is to decide whether these two requirements can be satisfied simultaneously or not. The picture is qualitatively illustrated in Fig. 3.7. These two requirements define a shaded region in the γ_{T2S2}-γ_{S1T1} plane where the yield can be raised. As the doping density N_d changes, a

straight line is mapped from the origin. The slope of the line $\gamma_{S1T1}/\gamma_{T2S2}$ is an intrinsic property of the d-π exchange coupling and is independent of the doping density. For larger slope we have line A and the yield can never be raised. For smaller slope we have line B and the yield can be raised in an optimal range of doping density. The range of N_d where $\eta_S > 1/4$ corresponds to the case that the line passes through the dark region. The minimum requirement for the magnetic doping to work is $\gamma_{S1T1}/\gamma_{T2S2} < \gamma_S/\gamma_{TT}$. Our calculation shows that it is indeed the case. η_S as a function of N_d for various ΔE_{S2T2} is plotted in Fig. 3.8. For $\gamma_S = 3 \times 10^9 \; s^{-1}$ and $\gamma_{TT} = 2.7 \times 10^8$ s^{-1}, η_S rises initially with doping density N_d due to more redirection of $T2$ excitions. After reaching a maximum η_S decreases with N_d due to strong intersystem crossing from $S1$ to $T1$. There is a range of N_d where η_S is well above 1/4. Smaller energy barrier ΔE_{S2T2} implies larger γ_{T2S2}, which in turn implies more efficient $T2$ to $S2$ redirection (smaller slope for the line in Fig. 3.7) and stronger enhancement effect. η_S as a function of N_d for various $\tau_{TT} = 1/\gamma_{TT}$ is shown in Fig. 3.9. η_S rises then decreases with N_d because of the same reason as in Fig. 3.8. Larger τ_{TT} (tighter triplet bottleneck) makes the redirection from $T2$ to $S2$ easier (larger shaded region in Fig. 3.7) and the enhancement effect stronger. From Fig. 3.8 and 3.9 one can clearly see that the fast intersystem crossing between $T2$ and $S2$ excitons due to near degeneracy and slow decay from $T2$ to $T1$ excitons due to large energy gap are the two key conditions for the mechanism to succeed. In Fig. 3.10, η_S is plotted for various metal-polymer vertical distance R_d. The optimum doping density shifts to higher values as R_d increases and the strength of the dopants decreases. The physically relevant range of R_d is between 3 to 3.5 Å. Due to the ligand surrounding the metal ion it is impossible for have $R_d < 3$Å. For $R_d > 3.5$ Åthe exchange coupling is so weak that there is no effect of doping on η_S.

3.5   Discussion

Ligands are ignored in our calculation except for introducing crystal field. The ligands may block the overlap between the wave functions of the π- and d- electrons. In order to let the d-orbitals overlap with the π-orbitals easily, a transition metal complex with square planar geometry appears to be a proper choice. But such complexes usually contains eight d-electrons which occupy four d-orbitals. Since there is no unpaired electron, flipping the spin of one electron will violate the Pauli exclusion principle. Therefore, even though the ion is not shielded by the ligand in the out-of-plane direction, metal complexes with square planar geometry do not provide free moment to cause
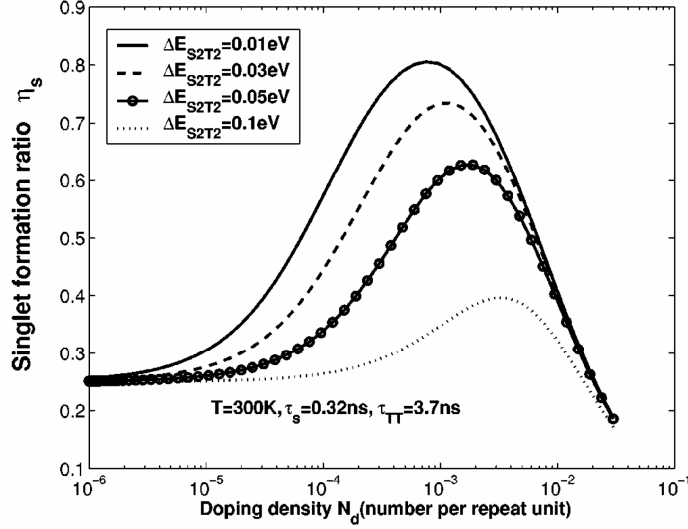
Figure 3.8: The singlet formation ratio η_S as the function of the doping density N_d for different ΔE_{S2T2}. τ_{TT} is fixed at 3.7 ns.
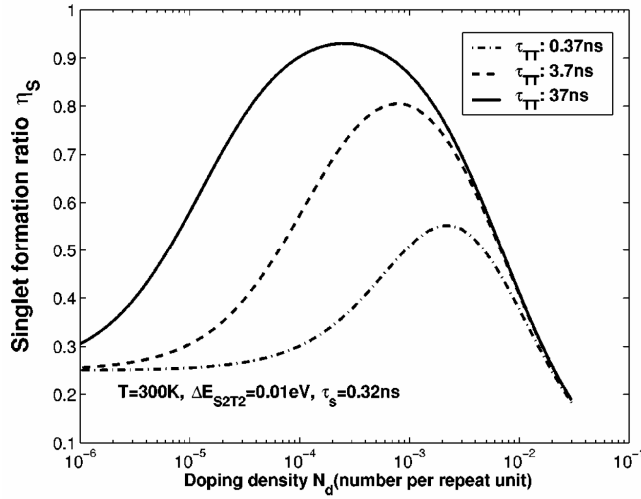
Figure 3.9: The singlet formation ratio η_S as the function of the doping density N_d for different T1 $\rightarrow$ T2 relaxation time τ_{TT}. ΔE_{S2T2} is fixed at 0.01eV. Tighter triplet bottleneck (larger τ_{TT}) redirects more triplet electron-hole pairs and causes higher singlet ratio.
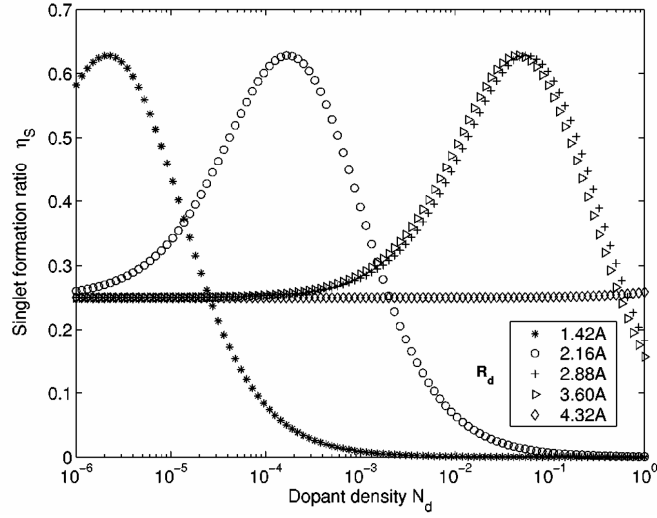
Figure 3.10: The singlet formation ratio η_S is shown for various metal-polymer distance R_d. It is easier to enhance the singlet formation when R_d is smaller and the exchange coupling is stronger. The physically relevant range for R_d is between 3 and 3.5 Å.

the desired spin-flip for the π-electron. On the other hand, complexes with octahedral or tetrahedral geometry usually have five or six d-electrons and provide free moments to flip the π-electron spin. Although the d-electrons appear to be enclosed inside the octahedron or tetrahedral by the ligands, the wave function can actually stretch out to interact with the π-electron on the polymer chain[86]. The measurement of ESR signal of π-electron in polyaniline doped with the tetrahedral $FeCl_4^-$ ion provides an evidence that there is still strong wave functions overlap between π-electron in the polymer and the d-electron in Fe^{3+} ion despite of the enclosure of the ion inside the tetrahedron[95]. It is therefore possible to use a non-planar complex as a dopant. The actual positions of the complexes in the polymer matrix are difficult to predict, considering the amorphous nature of the spin-coated film. The distance R_d between the metal ion and the polymer plane has been chosen to be about half of the polymer interchain distance in the calculation. In practice, the distance may be more than that because of the ligands surrounding the ion. In general, complexes with small ligands are expected to have a higher chance to come close to the polymer backbone. In addition to geometry, the spin configuration also affects the exchange coupling strength. Depending on the magnitude of the energy splitting for the d-electrons due to the ligand crystal field, the electrons will take either high spin or low

spin configuration. We present only the high-spin case, which offers larger magnetic moment and stronger exchange coupling to the π-electron. But the intersystem crossing rate for the low-spin case in our calculation is in the same order of magnitude. In other words, η_S can be raised or lowered as long as there is a free moment in the ion no matter how large the moment is.

The most convenient way to introduce the complexes into conjugated polymer film is to resolve both the complex and the polymer in the same solution then spin-coat to form the film. Good solubility of the complex in the solution is therefore required for uniform doping. After being mixed into the solution, some complexes may change their structure and properties due to the physical and chemical interaction between them and the solution. For example, planar complex tend to stack together, and $FeCl_3$ is highly reactive with the polymer itself. Such instability should be avoided in order to preserve the validity of this mechanism. Organic ferromagnetic materials[96] may also be used as dopants. Another way to introduce magnetic interaction is to synthesize new conjugated polymers with transition metal ions attached to the side groups. This will make the relative position between the magnetic and polymer chain closer and more stable.

3.6 Conclusion

It is predicted theoretically that doping transition metal complexes into conjugated polymer film can effectively enhance the intersystem crossing during exciton relaxation through the exchange coupling. With optimal doping density about $10^{-4} \sim 10^{-3}$ per repeat unit, the singlet exciton formation ratio in a LED can be raised from the spin-independent value 0.25 to 0.9. Slow triplet relaxation time τ_{TT} due to large energy gap between the lowest and the second lowest triplet excitons and fast intersystem crossing from the second lowest triplet to the second lowest singlet excitons due to near degeneracy make this enhancement mechanism possible.

Chapter 4

Recombination Distribution and Color Tuning of Multilayer Light-Emitting Diodes

4.1   Motivation

Organic semiconductors have been used as the emissive materials for efficient light-emitting diodes (LED)[1], which cover the whole visible spectra range. It will be highly desirable if one single LED can emit light with a wide range of color, continuously tuned by the applied voltage. Such tunable LED can be applied in the full-color display, signaling, and illumination. There have been reports of organic voltage-tuning color-tunable LEDs in polymer blends[97, 98], organic-inorganic composites[99, 100]. Recently we show the feasibility of wide-range low-voltage color tuning in polymer LED with multiple emissive layers[101]. But, without theoretical understanding in details, further improvement for each structure is difficult. Multilayer structures have been commonly used for organic LEDs. However, in most cases there is only one emissive layers while the other layers serves for carrier transport and blocking in order to improve the efficiency. There have been some reports on device simulation for multilayer organic LEDs, which are focused on the quantitative verification of the exciton recombination efficiency improvement owing to heterolayer interface[102–104]. In order to study the color-tunability, in this work we perform detailed calculation on the carrier and recombination distribution of OLED with multiple emissive layers. In particular, we calculate the continuous evolution of the recombination distribution as the voltage increases.

Due to the relatively low electron mobility, the recombination concentrates in the layer next to the cathode. As the voltage increases, the electron mobility increases rapidly with the electric field and the electrons moves through the heterojunctions and recombine with the holes in the other layers. The overall results are the continuous shift of the recombination distribution away from the cathode and the change of the ratio among the integrated recombination in each layer. This investigation systematically studies how several device parameters (namely, interface energy barrier for electron, mobility, and layer thickness) for multilayer organic LED influence the recombination current ratio (and therefore the color) among the layers. According to the effects on the recombination current profile derived from the parameters studied systematically, device structures are proposed to have color-tuning from red to green and finally to blue as the voltage increases.

We starts from device simulation for single layer organic LED (Sec.4.1). The device model includes injection, transport, and recombination. In section 4.2, the method to treat the heterojunction as internal boundary condition is included to calculate the device with two layers. Then the color-tunable devices with four layers are proposed in section 4.3. In section 4.4, we present fabrication for the color-tunable polymer LED.

Wide-range low-voltage continuous color tuning is achieved in multilayer light-emitting diodes based exclusively on the commonly used high-efficiency electroluminescent conjugated polymers. There are three layers for red, green, and blue emission, and one extra layer for electron blocking. The color of the emitted photon depends on the position of the electron-hole recombination. Due to the stronger field dependence of the electron mobility relative to the hole mobility, the recombination zone is pushed away from the cathode and concentrated in different emissive layers as the voltage increases.

4.1.1 Potential of spin-on technology for multilayer PLED

Conjugated polymers have been used as the emissive materials for efficient light-emitting diodes (LED)[1], which cover the whole visible spectra range. The emission color is fixed by the band gap of the particular polymer. Poly(p-phenylene vinylene) (PPV) and polyfluorene (PF) are the two most important families of conjugated polymers used in LED. PPV derivatives cover the red to green spectra range, while PF derivatives cover the whole visible range. It will be highly desirable if one single LED can emit light with a wide range of color, continuously tuned by the applied voltage. Such tunable LED can be applied in the full-color display, signaling, and illumination. There is currently a tremendous amount of effort on the PPV and PF display. In order to achieve a full-color pixel, ink-jet and other techniques are being developed to deposit accurately three different kinds of polymers for red, green, and blue in small areas[105, 106]. In addition to technical difficulties, such approaches sacrifice one great advantage of the conjugated polymers, namely, ease of direct spin-coating to form large-area uniform films. It will be much simpler if the polymer film is uniformly formed while the color of each pixel is controlled by the voltage. Apparently the capability of such continuous color tuning will also be highly desirable for solid-state illumination in the future. There have been reports of organic color-tunable LED involving small molecules[107], a combination of polymers and small molecules[108–110], CdSe nano-particle/polymer composites[99, 100], dye-doped polythiophene[111], polythiophene blends[97, 98], and n-type polymers[112]. In this letter, we propose a mechanism which enables wide-range color-tuning for multilayer polymer LED based on PPV and PF with tuning voltage as low as 4 V.

4.1.2 Disparate electron-hole transport

Color-tuning can be realized in a multilayer LED if the electron-hole recombination zone is controlled by the volt-age. Due to the presence of electron

traps in most conjugated polymers including PPV and PF, the electron mobility μ_e is much smaller than the hole mobility μ_h . So the holes can easily move away from the anode while the electrons hardly move far from the cathode. The carrier mobility depends on the electric field E in the PooleVFrenkel form: $\mu = m_0 e^{\gamma \sqrt{E}}$. The parameter γ determines how rapidly the mobility increases with E. As the voltage bias increases, the electron traps are gradually filled by the injected current and me increases strongly[23]. This corresponds effectively to a larger γ for μ_e than for μ_h[4]. For the typical case of poly [2-methoxy-5 (2'-ethyl-hexyloxy)-1,4-phenylene vinylene] (MEH-PPV), it is shown that $\mu_h = 37\mu_e$ at zero field, while $\mu_h = 2.2\mu_e$ at $E = 2 \times 10^8$ V/m[4]. Light emission is due to the recombination of the holes and electrons. At low bias, the electron distribution concentrates near the cathode, while the hole distribution is more extended from the anode due to the higher mobility. So most of the recombination takes place near the cathode. As the bias increases, the electron distribu-tion become more extended, and the recombination moves from the cathode toward the anode[23]. In single-layer LED, such motion of the recombination zone does not alter the emission color. However, the color does vary due to such zone motion in multilayer LED whose layers emit with different colors. At low bias, recombination occurs only in the layer nearest to the cathode. As bias increases, electrons be-come able to move out of the nearest layer and recombination takes place in other layers successively. An electron blocking layer is needed to enhance the electron density and recombination in the farthest layer from the cathode at high bias by confining the electrons near the interface with the blocking layer. It is expected that in such multilayer LEDs the motion of the recombination zone through different layers causes a continuous change in the weighting of the emission from each layer. The overall color can therefore be con-trolled by the voltage.

4.2   Single Layer Devices

The device characteristics of organic LEDs are determined by the injection of charge from the contacts into the material, the transport of charge through the material, and the carrier recombination inside the device. The energetics which determine charge injection can be determined by experimentally[46]. Once the energetics are understood, the transport can be studied by modeling the current voltage characteristics of devices[38, 39]. This section presents studies of injection and transport in single layer devices[6].
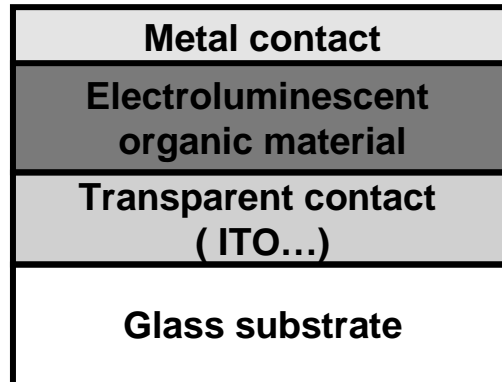
Figure 4.1: Schematic of single layer LED structure[6].

4.2.1 Overview of organic LED operation

A simple device structure for study of charge injection and transport in organic light emitting diodes is shown in Fig. 4.1[15]. It consists of a substrate, and an organic material layer sandwiched between two electrodes. Single carrier single layer devices are the simplest organic diode structure. With the appropriate choice of electrodes they allow the study of charge injection and transport in organic LEDs for each carrier type separately[38, 39].

Organic LEDs consist of a layer of organic material sandwiched between two charge injecting electrodes, as seen in Fig. 4.1. The operating principle of a single carrier single layer organic diode is shown in Fig. 4.2. Contacts are chosen so that the energy barrier for injection of holes is relatively small, but the energy barrier for injection of electrons is sufficiently large that a negligible number of electrons are injected. Fig. 4.2 shows a case where the right electrode provides a smaller barrier than the left electrode. At zero voltage bias the devices is in equilibrium and there is no current flow. As a positive voltage is applied to the right contact a field develops across the device which sweeps holes injected at the right contact across the device to give a current. When a negative bias is applied across the device a field develops which sweeps holes injected at the left contact across the device giving rise to a current of the opposite sign. Because the contacts provide different barriers for hole injection to current voltage characteristic are not symmetric. The contact with the smaller energy barrier requires less voltage for the same current.

The current voltage characteristics are determined by the injection of charges at the contacts, and the transport of charge through the device. There are two limiting cases for charge injection. If the barriers to charge
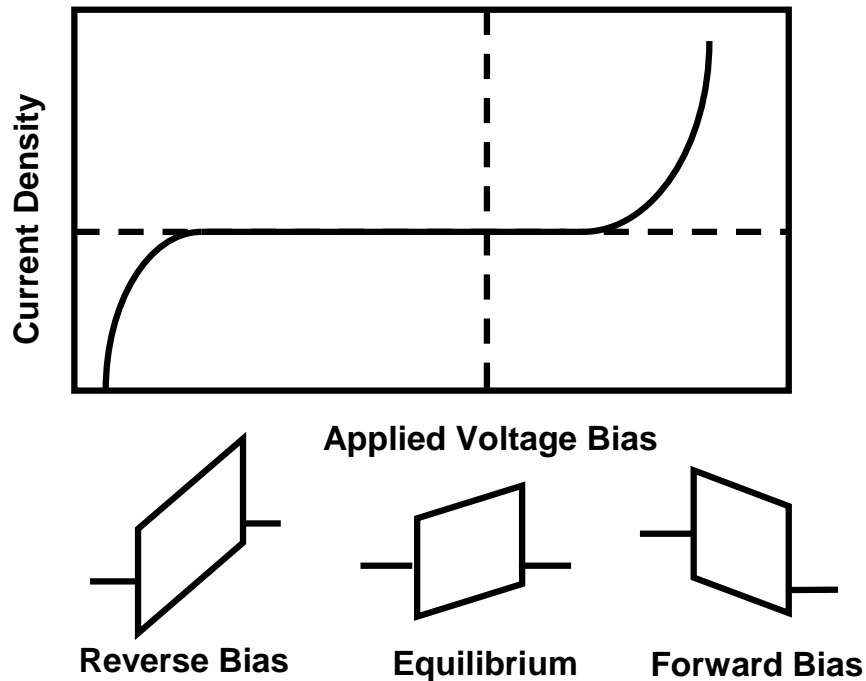
Figure 4.2: Single Carrier Device Operation. The asymmetry of the current voltage curve is due to the difference in Schottky energy barriers to injection of holes, shown in the energy diagrams[6].

injection are relatively large then the carrier densities are relatively small in the device. In this case, the charge density are too small to affect the electric field, which is uniform across the device, and the carrier density is also uniform to insure a constant current density. This is the injection limited regime[25]. If the barriers to charge injection are small, then the carrier density at the injecting contact is larger, and affects the electric field, which is no longer constant across the device. The charge density decreases across the device and the electric field increases, in such a way that the current density is constant. The injected charge accumulates at the injecting constant. This is the space charge limited regime[25]. An efficient LED requires large carrier densities to drive recombination and low drive voltage, so contacts which are space charge limited and provide an energy barrier to injection as small as possible are desired.
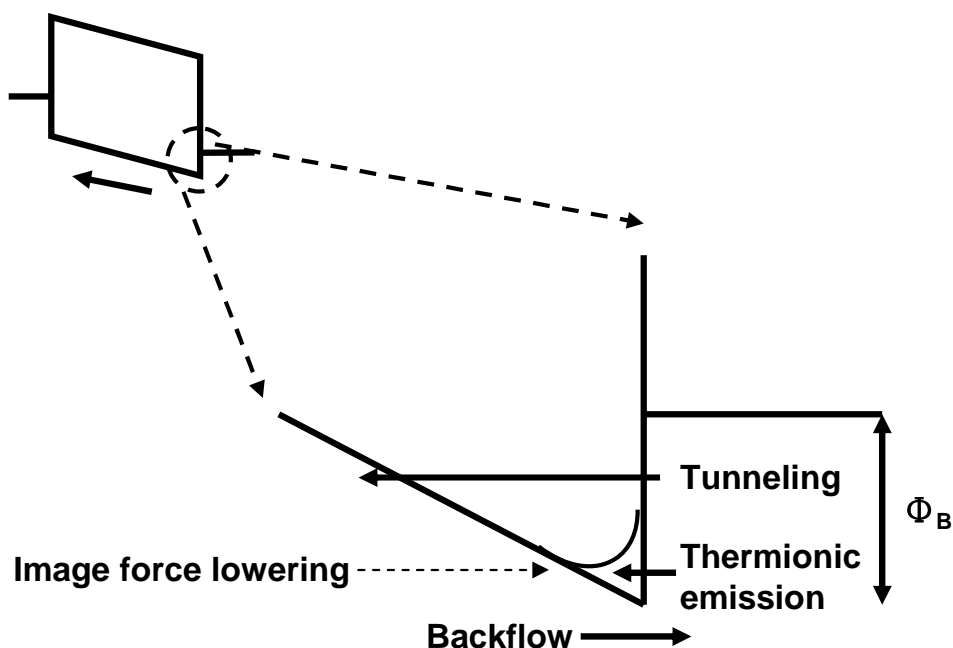
Figure 4.3: Energy diagram illustrating transport and injection in a hole only device[6].

4.2.2 Physical model

In single carrier devices, one must consider model with injection and transport; in bipolar device, the recombination process needed to be included. The most significant difference between organic and inorganic materials is the electric field dependence of the carrier mobilities. The electric field dependence of the mobility for organic material is deduced from theoretical and experimental aspects. We discuss the necessity for numeric solution while considering this form of mobility.

Injection and Transport

To model the characteristics of a single carrier single layer organic diode, one must consider injection of charge from the contacts into the material, and transport of charge through the material. The problem is illustrated schematically in Fig. 4.3. The transport of charge through the material depends on bulk properties of the organic and is determined by the solution of Poisson's equation coupled with the continuity equation, using a drift-diffusion form for the current and a field dependent mobility as seen in TOF measurements. Carrier injection at the contacts provides boundary conditions.

The physical model used in this work is as follows[45]. A polymer is made up of a series of conjugated chain segments which are terminated by twists or other defects which break the conjugation. Nondegenerate cases are considered, so that the occupation probability of a conjugated chain segment is much less than one. The density of conjugated chain segments times the degeneracy of a conjugated chain segment (the number of ways it can be occupied by an electron or hole) is denoted n_0, so the equilibrium carrier densities are given by:

$$n_e = n_0 e^{-(E_C - e\phi(x) - \Psi)/k_B T}, \tag{4.1}$$
$$p_e = p_0 e^{(E_V - e\phi(x) - \Psi)/k_B T}, \tag{4.2}$$

where Ψ is the fermi energy, $\phi(x)$ is the electrostatic potential, and E_C and E_V are the conduction and valence levels at the contact. These equations for the equilibrium carrier densities implicitly assume that there is one energy level E_C for electrons, and one energy level E_V for holes. These level E_C and E_V are effective condition and valences levels such that the above expressions gives the same result as[18]:

$$n_e = n_0 \int \frac{D_C(E)}{e^{-(E_C - e\phi(x) - \Psi)/k_B T}}, \tag{4.3}$$
$$p_e = p_0 \int \frac{D_V(E)}{e^{(E_V - e\phi(x) - \Psi)/k_B T}}, \tag{4.4}$$

where D_C and D_V are the density of states of the conduction and valence levels.

The organic materials are relatively large bandgap undoped materials, with very low intrinsic carrier densities. The devices are fully depleted in equilibrium[16, 17]. All charges leading to current are injecting from the contacts. Electron and hole polarons (denoted electrons and holes) move through the organic material by moving along a chain segment and then hopping to the next conjugated chain segment[19, 32, 34]. The hop from one chain to the next is the rate limiting step and determines the transport properties. The conjugated chain segments have some localized energy distribution which forms the manifold the carriers hop through. This is shown in Fig. 4.4. In this work, this distribution of localized states is to be called as conduction or valence states. They are assumed to be in equilibrium. Traps are deeper states which are not in equilibrium and are not shown in the figure. Electric impedance measurements of MEH-PPV polymer LEDs estimate the trap density in MEH-PPV to be at most a few times $10^{16} cm^{-3}$[17]. The
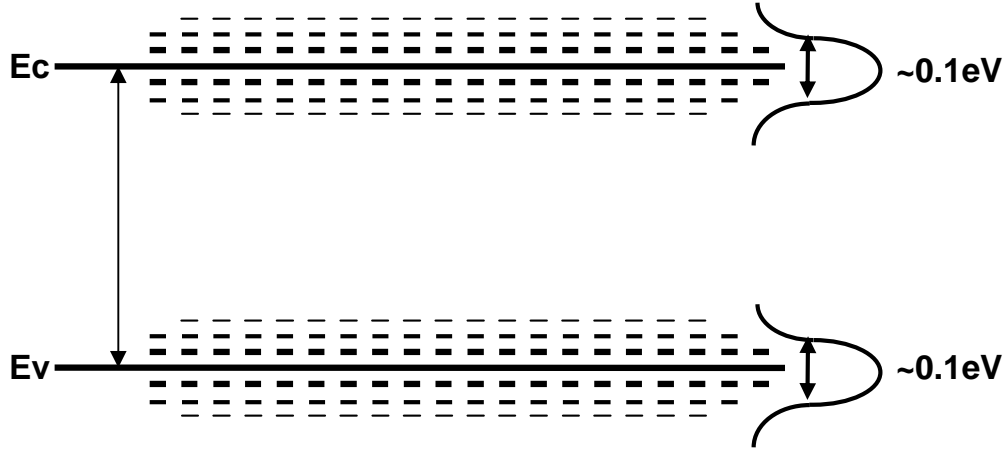
Figure 4.4: Schematic of localized density of states in organic materials[6].

transport through this localized random manifold is treated by solving the continuity equation for charge carriers, coupled to Poisson's equation, using drift-diffusion currents[18],

$$\frac{\partial n}{\partial t} - \frac{1}{e}\frac{\partial J_n}{\partial x} = G - R, \tag{4.5}$$

$$\frac{\partial p}{\partial t} + \frac{1}{e}\frac{\partial J_p}{\partial x} = G - R, \tag{4.6}$$

$$\frac{\partial E}{\partial x} = \frac{e}{\varepsilon\varepsilon_0}(p - n), \tag{4.7}$$

where

$$J_n = e\mu_n(pE - \frac{k_B T}{q}\frac{\partial n}{\partial x}), \tag{4.8}$$

and

$$J_p = e\mu_p(nE + \frac{k_B T}{q}\frac{\partial p}{\partial x}), \tag{4.9}$$

where the mobility μ is taken as the field dependent form $\mu_0 e^{\sqrt{E/E_0}}$, as seen in time of flight measurements[24, 35–37].

The injection is from the metal into the distribution of localized states in the organic. Fig. 4.5 shows a schematic of the particle currents at an interface. The are thermionic emission and tunneling currents from the metal into the organic and a backflowing current from the organic into the metal.
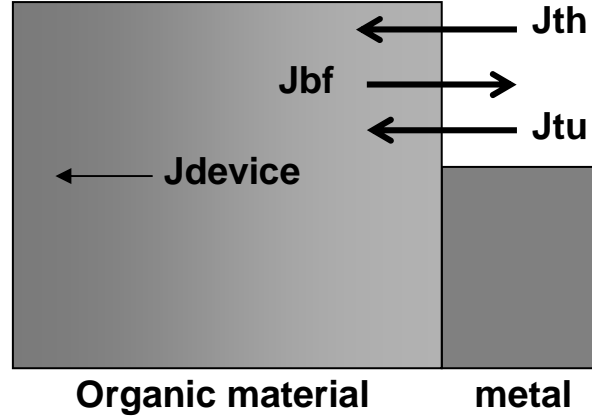
Figure 4.5: Current processes at the metal / organic interface[6].

These currents add up to the device current. In most cases of interest for organic LEDs the injecting contacts are in quasithermal equilibrium. The device current is so small compared to the thermionic emission and back-flowing current, that the carrier density is determined by the quasithermal equilibrium value.

Poole-Frenkel Form Mobility for Disordered System

Carrier mobilities in conjugated organic materials have been studied by transient methods such as time of flight(TOF), and step pulse transient current measurements, and by steady state measurements such as I-V. What is found is a carrier mobility which is field and temperature dependent. The experimental data have been parameterized using mobilities of the following forms[34]:

$$\mu = \mu_0 e^{\frac{-\Delta_0}{k_B T}} e^{\beta(\frac{1}{k_B T} - \frac{1}{k_B T_0})\sqrt{(E)}}, \tag{4.10}$$

or,

$$\mu = \mu_0 e^{-(\frac{2\sigma}{3k_B T})} e^{C((\frac{\sigma}{k_B T})^2 - \Sigma^2)\sqrt{E}}. \tag{4.11}$$

Equation 4.10 was proposed by Gill and later interpreted by others in terms of a dipole trap model, where the transport sites are dipolar traps in a transporting matrix[113, 114]. The E and T dependencies aries from the variation of the escape rate from these traps. Within this model Δ_0 and $T_0 = \Delta_0/k_B$ are determined by the trap depth. Eq.4.11 is based on the gaussian disorder model of Bässler, where transport by hopping through

the gaussian distribution (in energy) of transport sites[32]. In this measure of the represents the standard deviation of the gaussian distribution, and Σ is a measure of the variation of intersite coupling. For devices at a given temperature, both approaches give a similar Poole-Frenkel dependence of mobility on field which can be expressed more simply as:

$$\mu = \mu_0 e^{\sqrt{E/E_0}}, \tag{4.12}$$

with this field dependence the deviation of space charge limited current is not an analytic problem and requires numeric solution. Even in the simple case where the mobilities are constant with field, solution are obtainable for the limits of contact limited current and space charge limited current, but not the transition between them. Generalization to bipolar single layer devices or to multilayer devices with materials having field dependent mobilities also requires numeric solution.

Recombination Process

In single carrier device, almost all of the majority carriers traverse across the device without recombining with the minority carriers, hence recombination process can be neglected. However, in bipolar device, recombination can occur between electrons and holes. We present the physical model used for recombination as follow[47, 48]. The carriers have low mobility and move through a manifold of localized states. The electron and hole are attracted by their mutual coulomb attraction and move slowly toward each other across the device in this field. The lifetimes of singlet excitations in MEH-PPV has been measured from transient photoluminescence to be less than 1ns, and the lifetime of triplet excitations is not known[115]. The intrinsic triplet exciton lifetime is expected to be quite long, of the order of a msec, because the transition from the triplet exciton to the singlet ground state is forbidden by conservation of spin angular momentum[31, 116]. The actual triplet exciton lifetime is assumed to be of the same order of magnitude as the singlet lifetime, due to extrinsic effects which reduce the triplet lifetime. The transit time for a hole across a 100nm device at a field of 1MV/cm and mobility of 3×10^{-4}cm^2/Vs is about 30ns. The transit time for electrons is much longer. The electron and hole move slowly across the device toward each other in their mutual coulomb field, and form excitons. The excitons are able to move to the lowest energy state in their local area bofore recombining. the singlet excitations emit light, the triplet do not.

The recombination is bimolecular with a kinetic coefficient determined by the dynamics of the recombination. The physical model described above, the motion of low mobility carriers toward each other in mutual coulomb field to

form an exciton which quickly recombines, has been previously described by Langevin, and is used by others[47, 48, 117]. The results is a recombination rate of the form:

$$R = \gamma_{np} np = \frac{e\mu_R}{\varepsilon\varepsilon_0} np, \qquad (4.13)$$

where γ_{np} is the kinetic coefficient, and μ_R is an effective mobility taken as the larger of μ_n and μ_p[45].

Carriers can either recombine in the organic layer, or traverse the organic layer without recombining. To determine the fraction of carriers which recombine, consider the continuity equations for electron and holes

$$\frac{\partial n}{\partial t} - \frac{1}{e}\frac{\partial J_n}{\partial x} = G - R, \qquad (4.14)$$

$$\frac{\partial p}{\partial t} + \frac{1}{e}\frac{\partial J_p}{\partial x} = G - R, \qquad (4.15)$$

where J_n and J_p are the electron and hole current densities, respectively, e is electric charge, and G and R are the generation and recombination rates of electron hole pairs. For the energy gaps typical of organic materials used for LEDs, the generation rate is negligible under normal LED operating conditions.

At steady state, the continuity equation can be integrated spatially to obtain the recombination current J_r

$$J_r = \int_0^L eR dx = J_n(L) - J_n(0) = J_p(0) - J_p(L). \qquad (4.16)$$

From the equation above, the electrons (holes) injected at x=0 (x=L) to give $J_n(0)$ ($J_p(L)$) either recombine in the device and contribute to the recombination current J_p or completely traverse the device and contribute to $J_n(L)$ ($J_p(0)$). Both electron current at the hole injecting contact $J_n(L)$ and hole current at the electron injecting contact $J_p(0)$, result in parasitic loss which lowers quantum efficiency. In the ideal case of unity quantum efficiency $J_r = |J|$, and $J_n(L) = J_p(0) = 0$. This is shown schematically in Fig. 4.6.

4.2.3   SCLC for organic LED

Analytic models are often preferable to those that must be solved numerically because they can provide more physical insight and straightforward analysis of data. In this section, we simplify the model for both of the injection
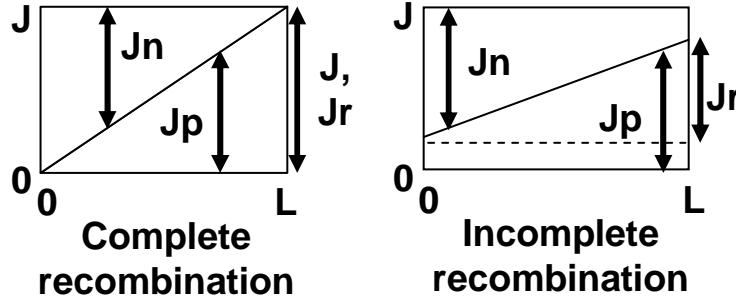
Figure 4.6: Schematic of an organic LED showing complete recombination (left) and incomplete recombination (right)[6].

limited and space charge limited cases to some case which can be solved as a analytical form. With these analytical form of solutions, we can clarify the transition from space charge limited to injection limited more clearly.

In contact (injection) limited case the carrier densities and field profiles are uniform across the device. The thermionic emission and backflow currents are much larger than the device current so the carrier density is determined by the quasithermal equilibrium value. For a hole only device, shown in Fig. 4.2, where the holes are injected from the left contact at x_{inj}, the hole density is given by:

$$p(E(x_{inj})) = n_0 e^{-\Psi_B/(k_B T)}. \tag{4.17}$$

The barrier Ψ_B includes image force lowering of the zero field barrier Ψ_h if the field has the correct sign[18]:

$$\Psi_B = \Psi_h - e\sqrt{\frac{e|E(x_{inj}))|}{4\pi\varepsilon\varepsilon_0}}. \tag{4.18}$$

So that the device current is:

$$J = e\mu p(E(x_{inj}))E = e\mu n_0 e^{-\Phi_B/(k_B T)}E. \tag{4.19}$$

To solve for the space charge limited current in a device the continuity equation and Poisson's equation are needed[25]. For the simplest case of a single carrier type(holes), constant carrier mobility, and neglecting the diffusion current, the continuity equation is:

$$\frac{\partial p}{\partial t} + \frac{1}{e}\frac{\partial J}{\partial x} = G - R \tag{4.20}$$

where p is the hole carrier density in excess of the equilibrium value, J is the hole (hence total) current, and G and R are generation and recombination rates. for single carrier devices (R=0) using insulating materials (G=0) at steady state ($\partial p/\partial t = 0$), Eq.4.20 simplifies to:

$$\frac{1}{e}\frac{\partial J}{\partial x} = 0 \quad or \ J \ = \ constant \ with \ respect \ to \ x. \tag{4.21}$$

Diffusion is neglected, so the current is from drift, and is given by:

$$J \ = \ q\mu pE, \ so \ that \ p \ = \ \frac{J}{e\mu E}, \tag{4.22}$$

where μ is the hole mobility and E is the electric field. Poisson's equation can be written:

$$\frac{\partial E}{\partial x} = \frac{e}{\varepsilon\varepsilon_0}p = \frac{1}{\mu\varepsilon\varepsilon_0}\frac{J}{E}. \tag{4.23}$$

The injected current in the space charge limited case is sufficiently high to cause a spatial variation in the electric field. The electric field and hole carrier density vary so J=eμpE=constant with respect to x. The electric field variation cab be determined by integrating Poison's equation.

$$EdE \ = \ \frac{1}{\mu\varepsilon\varepsilon_0}Jdx \ , \tag{4.24}$$

$$\int_0^E E'dE' \ = \ \frac{1}{\mu\varepsilon\varepsilon_0}J\int_0^x dx' \ , \tag{4.25}$$

$$\frac{1}{2}E^2 \ = \ \frac{1}{\mu\varepsilon\varepsilon_0}Jx \ , \tag{4.26}$$

$$E \ = \ \sqrt{\frac{2}{\mu\varepsilon\varepsilon_0}Jx} \ , \tag{4.27}$$

$$V = \int_0^L Edx \ = \ \frac{2}{3}(\frac{2}{\mu\varepsilon\varepsilon_0})^{1/2}L^{3/2} \ , \tag{4.28}$$

$$J \ = \ \frac{9}{8}\mu\varepsilon\varepsilon_0\frac{V^2}{L^3} \ . \tag{4.29}$$

Equations 4.19 and 4.29 present the transition from injection limited current to space charge limited current as the energy barrier to injection is lowered. For small barrier the current is space charge limited and given by Eq.4.29, however for large barrier it is injection limited and given by Eq.4.19.
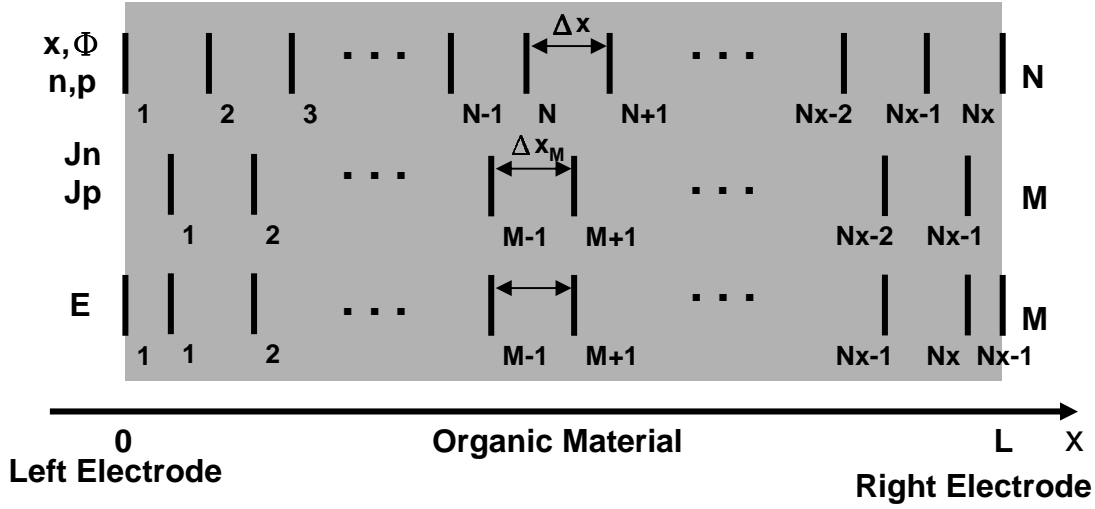
Figure 4.7: The gridding scheme used for the device model. N are grid points, M are half grid points[6].

4.2.4 Numeric method

After including diffusion current, recombination process, and Poole-Frenkel form mobility, analytical solution for the device model is impossible. We must solve the model by numeric method. This section presents the numeric model used to describe organic diodes. The structure of this section follows the procedure used in obtaining the solution. At first the physical model for the problem, presented in the previous section, is cast into a form which can be solved numerically, then the equilibrium solution is obtained, then voltage ramps are applied, and finally the time dependent forms of the equations describing device behavior are integrated forward in time, insuring that boundary conditions are met and a steady state solution is obtained.

Formulation of numeric solution

The system of equations to be solved: the continuity equation; Poisson's equation; and the drift-diffusion currents are given by Eq.4.5 through (4.9). These equations are discretized using the procudure of Scharfetter and Gummel with the gridding shown in Fig. 4.7[118]. The gridding for ϕ, n, p, and x are labelled by N. The gridding for J_n, J_p and E are labelled by M and are the midpoints of the N grids. The derivations below are applicable to uniform or nonuniform gridding. Eq.4.5 and Eq.4.6 are discretized in a simple manner to give:

$$\frac{\partial n}{\partial t}(N) = G(N) - R(N) + \frac{J_n(M) - J_n(M-1)}{\Delta x_M}, \quad (4.30)$$

$$\frac{\partial p}{\partial t}(N) = G(N) - R(N) - \frac{J_p(M) - J_p(M-1)}{\Delta x_M}, \quad (4.31)$$

where the boundary conditions, specified by J_n and J_p at the contacts, are implicit in these equations, Poisson's equation is discretized as two first order differential equations:

$$\frac{E(M+1) - E(M)}{\Delta x_M} = \frac{e}{\varepsilon\varepsilon_0}(p(N) - n(N)), \quad (4.32)$$

and, for the electrostatic potential,

$$E(M+1) = -\frac{\phi(N+1) - \phi(N)}{\Delta x}, \quad (4.33)$$

where

$$\Delta x_M = \frac{1}{2}(x(N+1) + x(N)) - \frac{1}{2}(x(N) + x(N-1)) = \frac{1}{2}(x(N+1) + x(N-1)), \quad (4.34)$$

and

$$\Delta x = x(N+1) - x(N). \quad (4.35)$$

Eq.4.32 and Eq.4.33 provide the discretization of Poisson's equation, which is used in conjunction with the expressions for equilibrium carrier densities to solve the equilibrium case. The rest of the current voltage characteristics are determined by integrating the time dependent equations describing device operation. The time dependence for the carrier densities $\partial n/\partial t$ and $\partial p/\partial t$, have been presented. Now the time dependence of the electric field $\partial E/\partial t$, which is obtained from Poisson's equation is shown as follows:

$$\frac{\partial}{\partial t}(\frac{\partial E}{\partial t} = \frac{q}{\varepsilon\varepsilon_0}(p - n)), \quad (4.36)$$

$$\frac{\partial}{\partial x}\frac{\partial}{\partial t}E = \frac{q}{\varepsilon\varepsilon_0}\frac{\partial}{\partial t}(p - n) = -\frac{1}{\varepsilon\varepsilon_0}\frac{\partial}{\partial x}J, \quad (4.37)$$

$$\frac{\partial}{\partial x}(\frac{\partial}{\partial t}E + \frac{1}{\varepsilon\varepsilon_0}J) = 0, \quad (4.38)$$

so that,

$$\frac{\partial}{\partial t}E + \frac{1}{\varepsilon\varepsilon_0}J = constant \ with \ respect \ to \ x. \tag{4.39}$$

The constant is chosen as the average value of Eq.4.39across the device, which introduce the boundary conditions $\phi(0) = 0$ and $\phi(L)$ as determined by the applied voltage ramp.

$$\frac{\partial}{\partial t}E + \frac{1}{\varepsilon\varepsilon_0}J = \frac{1}{L}\int_0^L (\frac{\partial}{\partial t}E + \frac{1}{\varepsilon\varepsilon_0}J)dx \tag{4.40}$$

so that

$$\frac{\partial}{\partial t}E(x) = -\frac{1}{L}\frac{\partial\phi(L)}{\partial t} - \frac{1}{\varepsilon\varepsilon_0}(J(x) - \frac{1}{L}\int_0^L J(x)dx). \tag{4.41}$$

Scharfetter and Gummel notices that if the drift-diffusion equations for the current are discretized in the same way as the continuity and Poisson's equations then the solutions are numerically unstable whenever the voltage change between grid points exceeds $2k_BT/e$.

The numeric solution

The solution is as follows.[45] First the equilibrium solutions is found by solving Poisson's equation. This is done numerically using the two first order equations, Eq.4.32 and Eq.4.33, using the equilibrium carrier densities given by Eq.4.1 and Eq.4.2. The relaxation method is used; that is, trial solutions for electric field and potential are given at first, iterated procedure is processed to get the solutions closer to the real solutions[119, 120]. This gives the equilibrium solution for ϕ, n, p, E, J_n, and J_p, using Eq.4.1, Eq.4.2, Eq.4.32, Eq.4.33, Eq.4.8, and Eq.4.9. To obtain a current-voltage curve a series of voltage ramps from time t_0 to t_{max} are applied, starting from the equilibrium solution already obtained, and proceeding stepwise through the biased of interest as shown in Fig. 4.8. Solution for n, p, and E are obtained by integrating Eq.4.30, Eq.4.31 for $\partial n/\partial t$, $\partial p/\partial t$, and Eq.4.41 for $\partial E/\partial t$. The equations for $\partial n/\partial t$ and $\partial p/\partial t$ include the boundary conditions for current, discussed in more detail below, and the equation for $\partial E/\partial t$ incorporates the boundary conditions for the electrostatic potential. Integration is done from time t_0 to steady state at t_{out}. In steady state, the continuity equations ($\partial n/\partial t = \partial p/\partial t = 0$) require that the total device current $J = J_n + J_p$ is constant across the device, this condition is used to verify that the time integration has reached steady state.
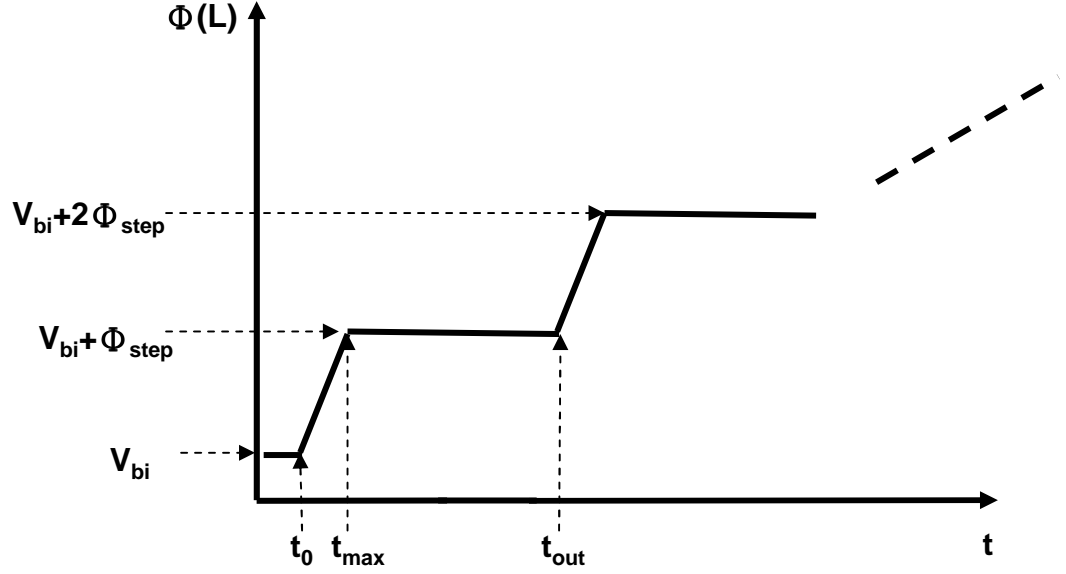
Figure 4.8: The current voltage characteristics are obtained by applying a series of voltage ramps in time to the right electrode[6].

4.2.5   Boundary conditions

The boundary conditions are determined by carrier injection processes at the contact[45]. Injection is from the metal into the distribution of states in the organic. Injection mechanisms considered, shown in Fig. 4.3, are thermionic emission of charge from the metal into the organic material, a "backflow" current from the organic into the metal which is the time reversed process of thermionic emission, and tunneling of charge from the metal into the organic. The total hole particle current J_p is given by:

$$J_p(L) = -J_{th} + J_{bf} - J_{tu} \tag{4.42}$$

where J_{th} is the thermionic emission particle current given by:

$$J_{th} = AT^2 e^{-\Psi_b/k_B T}, \tag{4.43}$$

and Ψ_B is given by Eq.4.18. The backflowing particle current J_{bf} is taken to be proportional to the hole density at contact,

$$J_{bf} = \nu p(L) \tag{4.44}$$

where the kinetic coefficient ν is determined by detailed balance between thermionic emission and the backflowing current.
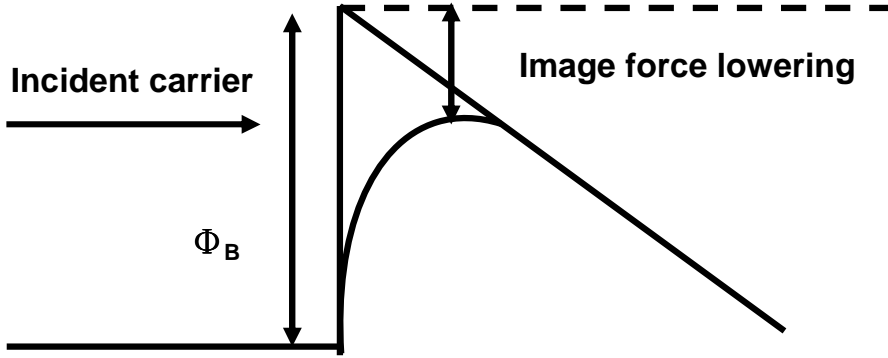
Figure 4.9: Carriers tunnel through a triangular barrier which includes image force lowering[6].

At equilibrium they must exactly cancel so that

$$\nu = \frac{AT^2}{n_0} \tag{4.45}$$

and

$$J_p(L) = \nu[p(L) - p_e(E(L))] - J_{tu}, \tag{4.46}$$

where p(E(L)) is the quasithermal equilibrium hole density at the contact and includes barrier lowering

$$p(E(L)) = n_0 e^{-\Psi_B/k_B T}. \tag{4.47}$$

Tunneling current is calculated following Fowler and Nordheim using the WKB approximation for tunneling through a triangular barrier with image force lowering[121, 122]. The physical situation is shown schematically in Fig. 4.9. Is is just the problem of high field emission from an electrode into air, but we consider emitting into a medium with dielectric permittivity ε. This is a first approximation to the actual state of affairs in an organic LED, however a better approximation would require better incorporation of the wavefunction of carriers in the organic, which are not currently well understood. It is shown that for organic LEDs of interest the tunneling current is negligible, and current is determined by thermionic emission and its time reversed process, so that further refinement of the model for tunneling is unwarranted.

(a) 3.0

5.2 | $\mu_e = \mu_h$ | 5.2

(b) 3.0

4.0 | $\mu_e = \mu_h$ | 5.2

5.3eV
Standard
Hole-only Device

5.3eV
Effective
Hole-only Device
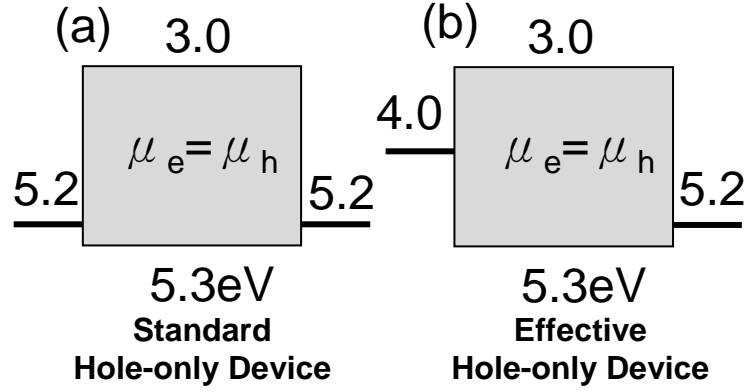
Figure 4.10: The structure of two hole-only device: (a) real hole-only device with two high work function metals on the two contact; (b) effective hole-only device with one high work function metal on the right contact and one low work function metal on the left contact.

4.2.6   Single carrier results and discussion

Calculations are presented for organic LEDs where holes dominate the current flow. The parameters used in the calculations presented here are those which were used to describe some experiments sited from other works. The electron and hole carrier levels are taken to be $E_C = 3.0$eV and $E_V = 5.3$eV giving an energy gap of 2.3eV. A dielectric constant $\varepsilon = 3$ and effective density of states $n_0 = 10^{27}$m^{-3} are used. The values used for the carrier mobility are $\mu_0 = 10^{-10}$m$^2/Vs$ and $E_0 = 4.3 \times 10^6$V/m. The calculations are done at room temperature. Injection of holes is from the right contact at x=L (100nm). The voltage is 6V.

Figure 4.10 demonstrates two types of hole only devices. Fig. 4.10(a) shows a standard holy-only device with high work function metals for both contacts. The device in Fig. 4.10(b) has a lower work function metal than that of the contact metal on the right side. As the electron barrier on the left side being 1.0eV, the electron density injected from the left contact is much less than the hole density injected from the right side, the hole current is effectively the device current. The electron zero field mobilties of both devices is lower than that of hole. However, since the injected electron is so low that the difference do not affect these two kind of hole-only devices.

Figure 4.11(a) and (b) present the electric field profiles for the two hole-only devices in Fig. 4.10 (a) and (b) respectively. Due to the low carrier density injected from the left contact, the electric field is smooth across the device. The electric field has a steep growth near the right contact, because

the hole density injected from the right side is large. The electron density injected from the left contact are much more than that of the standard hole-only device (Fig. 4.10(a)), however, the electron density is too low to compete with the hole density across the whole device, so that the electric field is determined by the hole density. Hence the electric fields for both of the two types of hole-only devices are almost the same. The main difference occurs at the left contact of both devices. The electric field at the left contact for the standard hole-only device has a very sudden change, however, the electric field at the left contact for the effective hole-only device varies quite smooth. Fig. 4.11(c) shows the potential of the standard device. There is a maximum inside the dashed circle marked at the right corner. The carriers at the left side of the maximum moves to the left direction, those at the right side of the maximum moves to the right direction. In order to stabilize the large inverse drift current for the right side, the diffusion current must be large.

Figure 4.12(a) and (b) present the electron (dashed line) and hole (solid line) density profiles for the two hole-only devices in Fig. 4.10 (a) and (b) respectively. For the standard device in Fig. 4.10(a), as the large number of holes being injected from the right contact, they accumulate near the right side owing to the low carrier mobility of the organic material. This is the space charge effect. The holes accumulate at the left side due to the space charge effect as well. However, across the device, there is no space charge effect for the hole density. The electron density in the standard hole-only device is so low that we can say there is no electron current inside the device. Although the electron density in the effective hole-only device in Fig. 4.10(b) is much more than that of the standard device in fig. 4.10(a), the electron density is still too low to affect the distribution for hole density. Hence the profile for the hole density is very similar to that of the standard hole-only device. The main difference for the electric field between these two devices described in last paragraph can be explained well by the hole distribution for the two devices. In the standard device, due to the small 0.1 eV hole barrier, high density of hole is injected from the left contact. The high density of hole causes the sudden rise of the electric field at the left contact for the standard device. On the other hand, in the effective device, due to the larger 1.3eV hole barrier and 1.0eV electron barrier, the density of electron and hole injected from the left contact are all very low, which can not affect the variation for the electric field.

Figure 4.13(a) and (b) present the recombination rate profiles for the two hole-only devices in Fig. 4.10 (a) and (b) respectively. Although the recombination rate profiles are very non-uniform across the device, the magnitude of the rates for both of these two cases is so low, which is 20 to 30 orders of magnitudes lower than that of a standard bipolar device, that no significant

Figure 4.11: The electric fields profiles for the two hole-only devices in fig. 4.10:(a) is for standard device in fig. 4.10(a); (b) is for effective device in fig. 4.10(b); (c) is the potential for the standard device.
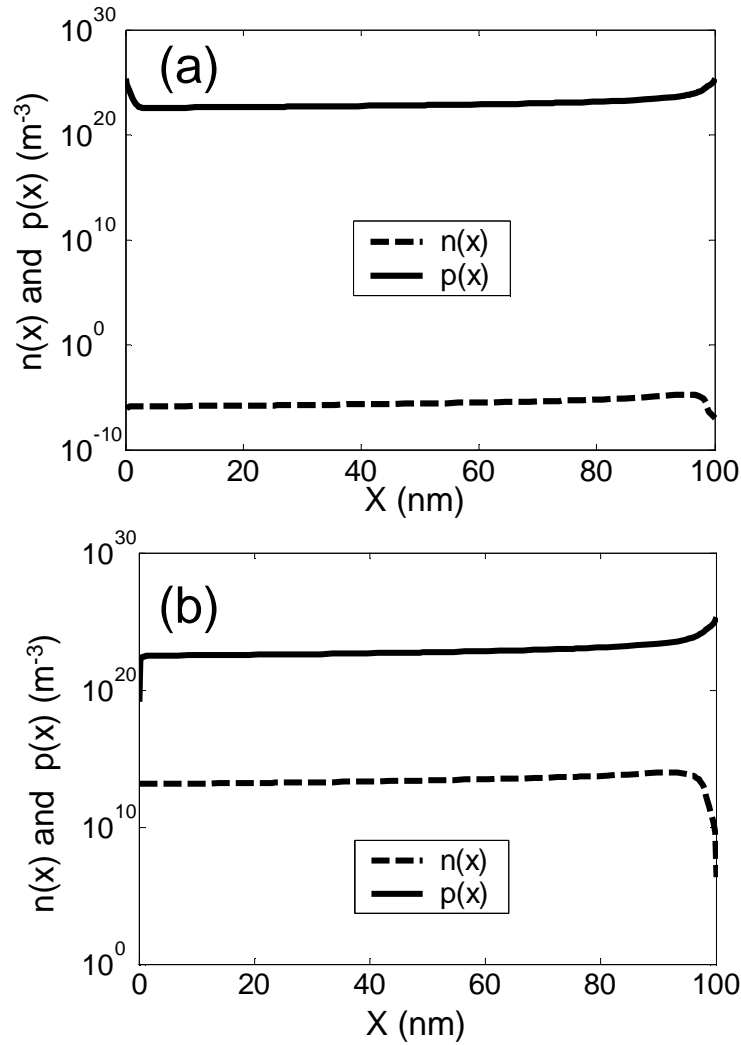
Figure 4.12: The electron (dashed line) and hole (solid line) density profiles for the two hole-only devices in fig. 4.10: (a) is for standard device in fig. 4.10(a); (b) is for standard device in fig. 4.10(b).

light can emit out of the device. Hence the unipolar device can not emit light in the sense of generating exciton from recombining the electron and hole injected from outside. We have shown another mechanism to generate excitons in unipolar device at chapter 2. Since, in the mechanism cited in the chapter 2, the exciton is generated by the impact ionization through hot hole, these two mechanisms do not conflict to each other. Since the the distribution of electron densities are uniform due to little electrons injected, the recombination distribution follows the profile of space-charged hole density.

In summary, a model which describes single carrier single layer devices has been presented. The model describes space charge limited, contact limited, and cases in between. The model provides insight into physical properties such as electric field profiles, carrier density, and recombination rate profiles. The device with small hole barrier for two contacts and the device with one large electron barrier and one small hole behave vary similarly. The space charge effect occurs at the contact with small hole barrier. Owing to the low electron density for the hole-only device, the recombination rate, which is proportional to the products of the hole density and the electron density, are so low that unipolar LED can not emit significant light.

4.2.7   Bipolar results and discussion

In order to emit light, there should be significant excitons recombined through injected electrons and holes. In unipolar LED cited in last section, the density for one type of the carriers is so low that the recombined excitons can not provide enough light to be radiated. Bipolar LED, which has the contacts with small injection barrier for electrons and holes, can provide significant recombined excitons to radiate light. Figure 4.14 shows structures for bipolar single layer devices with symmetric and asymmetric carrier mobilities. Figure 4.14(a) presents the case for symmetric carrier mobility. The zero field carrier mobility, μ_0, and the field dependence factor, E_0, for the symmetric device are $10^{-10}\text{m}^2/\text{Vs}$ and $4.3 \times 10^6\text{V/m}$ respectively. Figure 4.14(b) presents the case for asymmetric carrier mobility. The zero field hole (electron) mobility, μ_{0h} (μ_{0e}), and the field dependence factor, E_{0h} (E_{0e}), for the asymmetric device are μ_0 ($0.1 \times \mu_0$) and $4.3 \times 10^6\text{V/m}$ ($1.6 \times 10^6\text{V/m}$) respectively. The difference between the electron mobility of these two types of devices will cause vary important effects of the recombination rate profile. The recombination rate profile for the asymmetric device will shift from cathode to anode. This is the fundamental principle for color-tuning mechanism concerned mostly in this work.

Figure 4.15 demonstrates the electric field profiles for the two devices in fig. 4.14. Fig. 4.15(a) is for the symmetric case in fig. 4.14(a), fig. 4.15(b) is
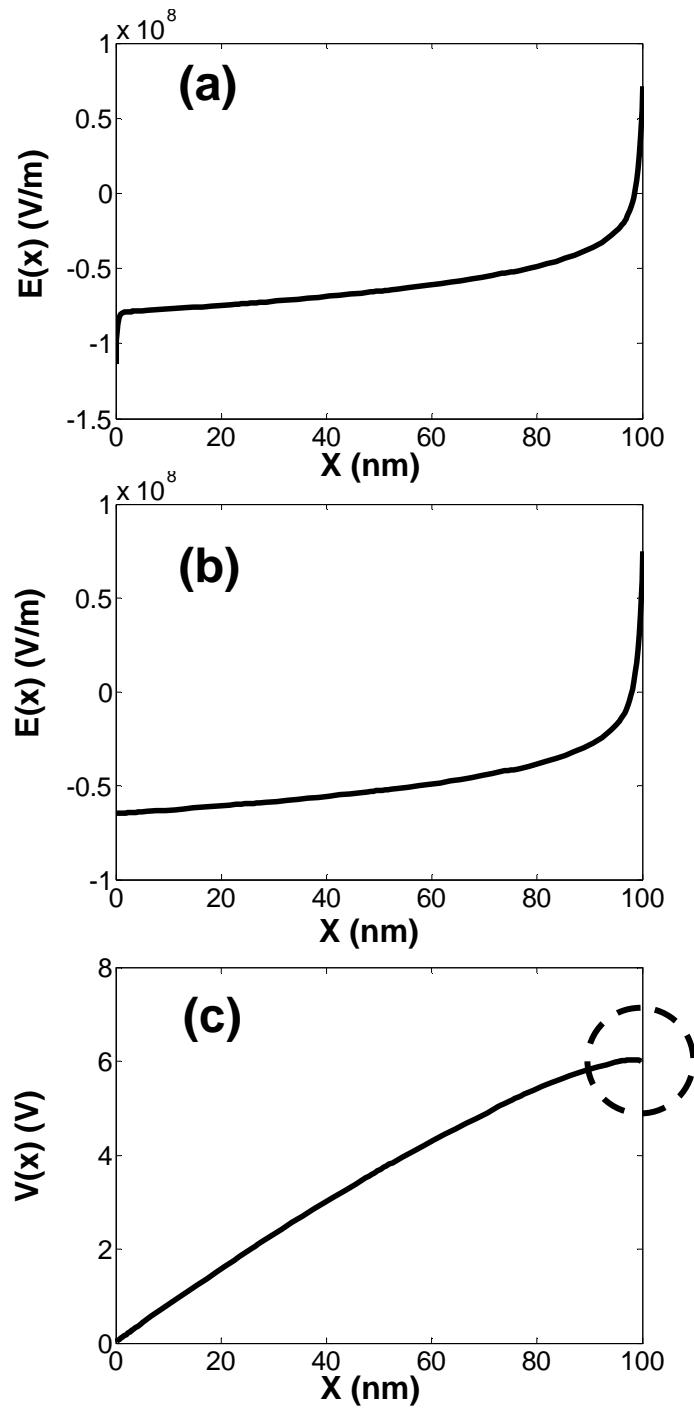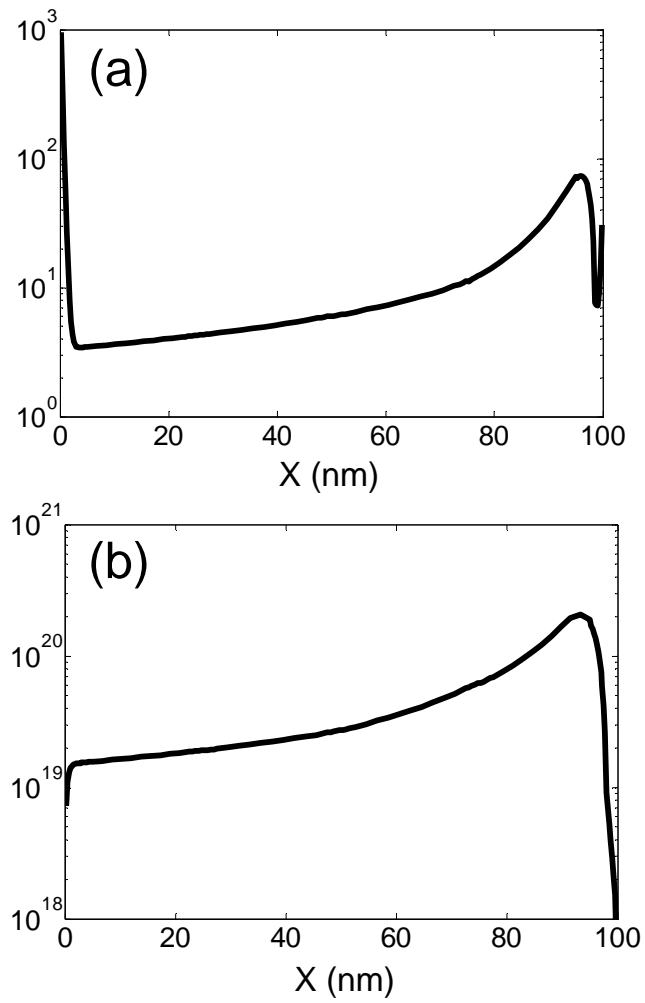
Figure 4.13: The recombination rate profiles for the two hole-only devices in fig. 4.10: (a) is for standard device in fig. 4.10(a); (b) is for standard device in fig. 4.10(b).
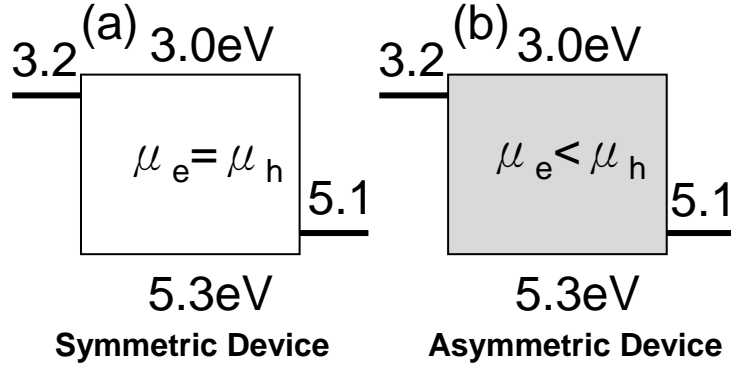
Figure 4.14: The structures of double carrier device with (a) symmetric carrier mobility and (b) Asymmetric carrier mobility.

for the asymmetric case in fig. 4.14(b). The profile variation for voltage as 3V (dotted line), 6V (dashed line), and 10V (solid line) are presented in fig. 4.15(b). The electric field for the symmetric device has a symmetric shape, that for the asymmetric device has nearly symmetric shapes for various bias voltage. In both of the cases, the electric fields near the two injected contacts are all lower than the field among the middle of the devices. The injected carrier densities from the contacts are higher than that among the middle of the device because the electric field needed to maintain the device current density steady for the parts near the contacts is lower than that for the parts among the middle of the device. As the voltage increases, the electric field profile lifts their averaged value, and the profile shape keep familiar. Fig. 4.15(c) shows the potential for the symmetric case in fig. 4.14(a). Compared with fig. 4.11(c), there is no maximum in fig. 4.15(c), it means that large diffusion current is not needed to stabilize the drift current for the bipolar case here.

Figure 4.16 presents the electron and hole density profiles for the two double carrier devices in fig. 4.14. Fig. 4.16(a) shows the electron (dashed line) and hole (solid) density for the symmetric case. Fig. 4.16(b) and (c) shows the electron and hole density variation for voltage as 3V (dotted line), 6V (dashed line), and 10V (solid line) respectively. The electron density for low voltage (3V) in the asymmetric case concentrate near the electron injecting contact. As the voltage increases, the electron mobility grows gradually higher than hole mobility that the electron density distribution tends to extend to the hole injecting contact. At the case for high voltage, the electron density on the side for hole injecting contact is even higher than that on the side for electron injecting contact. As the voltage increases, hole

Figure 4.15: The electric fields profiles for the two double carrier devices in fig. 4.14: (a) is for symmetric device in fig. 4.14(a); (b) is for asymmetric device in fig. 4.14(b). The profiles variation for voltage as 3V (dotted line), 6V (dashed line), and 10V (solid line) are presented; (c) is the potential for the symmetric case.

mobility also increases to let the distribution extend to the electron injection side. However, the field dependence for the hole mobility is weaker than that for electron, the variation of the hole density for voltage increasing is not so obvious as that of the electron.

Figure 4.17 presents the recombination rate profiles for the two double carrier devices in Fig. 4.14. Fig. 4.17(a) is for the symmetric case in Fig. 4.14(a), Fig. 4.17(b) is for the asymmetric case in Fig. 4.14(b). Fig. 4.16(b) shows the recombination rate profile variation for voltage as 3V (dotted line), 6V (dashed line), and 10V (solid line) respectively. For the case of the symmetric device in Fig. 4.17(a), the recombination rate profile has symmetric shape and distributes rather smoothly. For the case of the asymmetric device in Fig. 4.17(b), as the voltage increases, the recombination rate profile tends to extend to the hole injecting side. At high voltage, the recombination rate at the hole injecting side is even higher than that at the electron injecting side. The recombination rate profile shifting due to voltage increasing in the case for asymmetric device is the basic principle for color-tunable multilayer organic LED, which will be introduced in details at the later sections.

In summary, bipolar devices with both electrons and holes were described with a device model using carrier mobilities and Schottky energy barriers to injection determined in single carrier devices. Results of a device model for single layer organic LEDs which includes charge injection, transport, recombination, and space charge effects in the organic material have been presented. The role of transport was investigated by considering cases with field dependent mobilities those whose prefactors are both large (symmetric device), and cases where electron has a prefactor 10 times lower than hole, but the electric field dependence factor for electron is larger than that for hole (asymmetric device). Bimolecular carrier recombination was used with a Langevin form for the recombination coefficient. The results for the symmetric device are all symmetric and have no voltage variation on profile. However the results for the asymmetric device demonstrate obvious variation as voltage increases. The electron density distribution and therefore the recombination rate profile extends to the hole injection contact as the voltage increases. This distribution shifting is the basis for the color-tuning multilayer organic LEDs.

4.3   Bilayer Devices

Color-tunable multilayer device comprised with at least three emitting layers. There will be heterojunction between two layers. In this section, we investigate the case for only two layer, i.e. only one interface, especially on how to
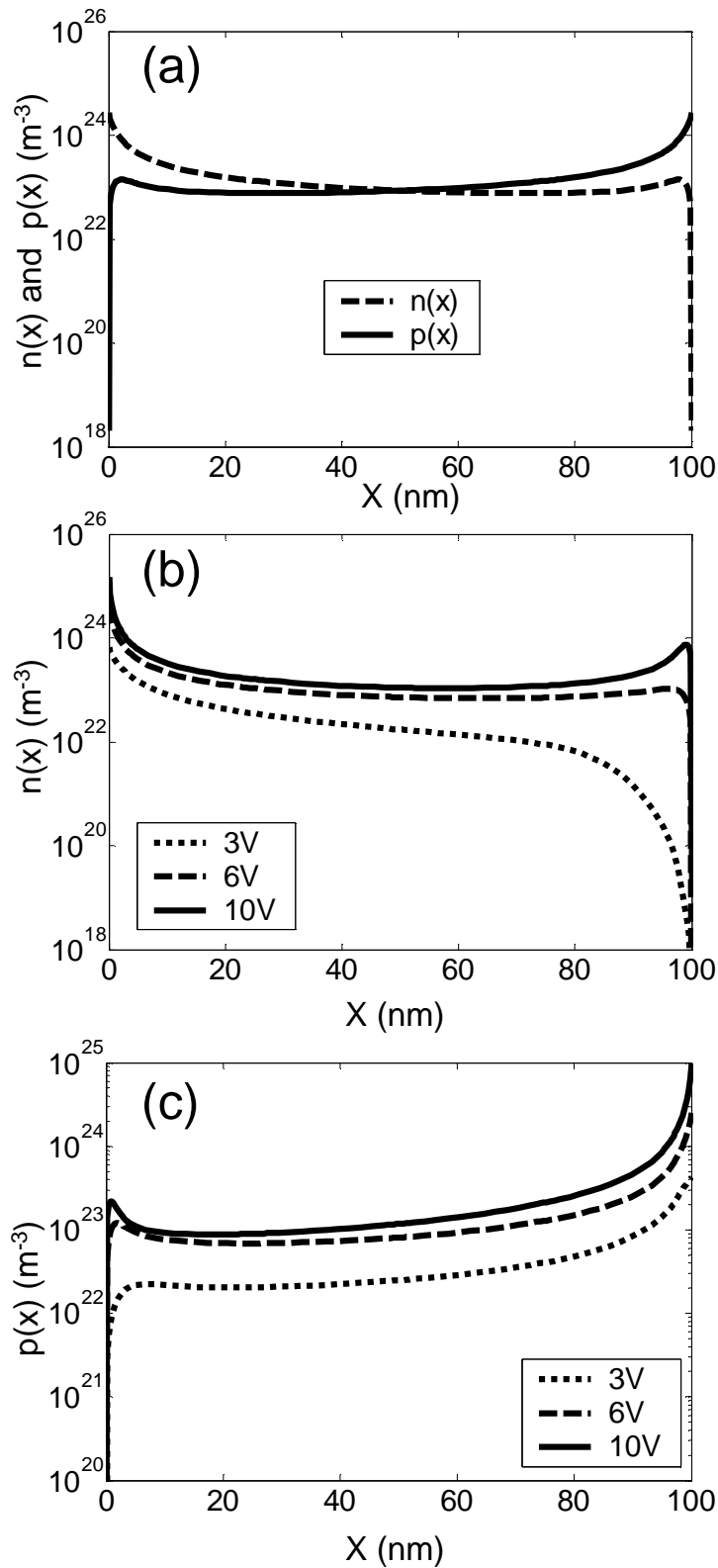
Figure 4.16: (a) The electron (dashed line) and hole (solid line) density pro-
files for the symmetric double carrier device in fig. 4.14(a); (b) the electron
and (c) hole density profile for the asymmetric double carrier device in fig.
4.14(b). The profile variation for voltage as 3V (dotted line), 6V (dashed
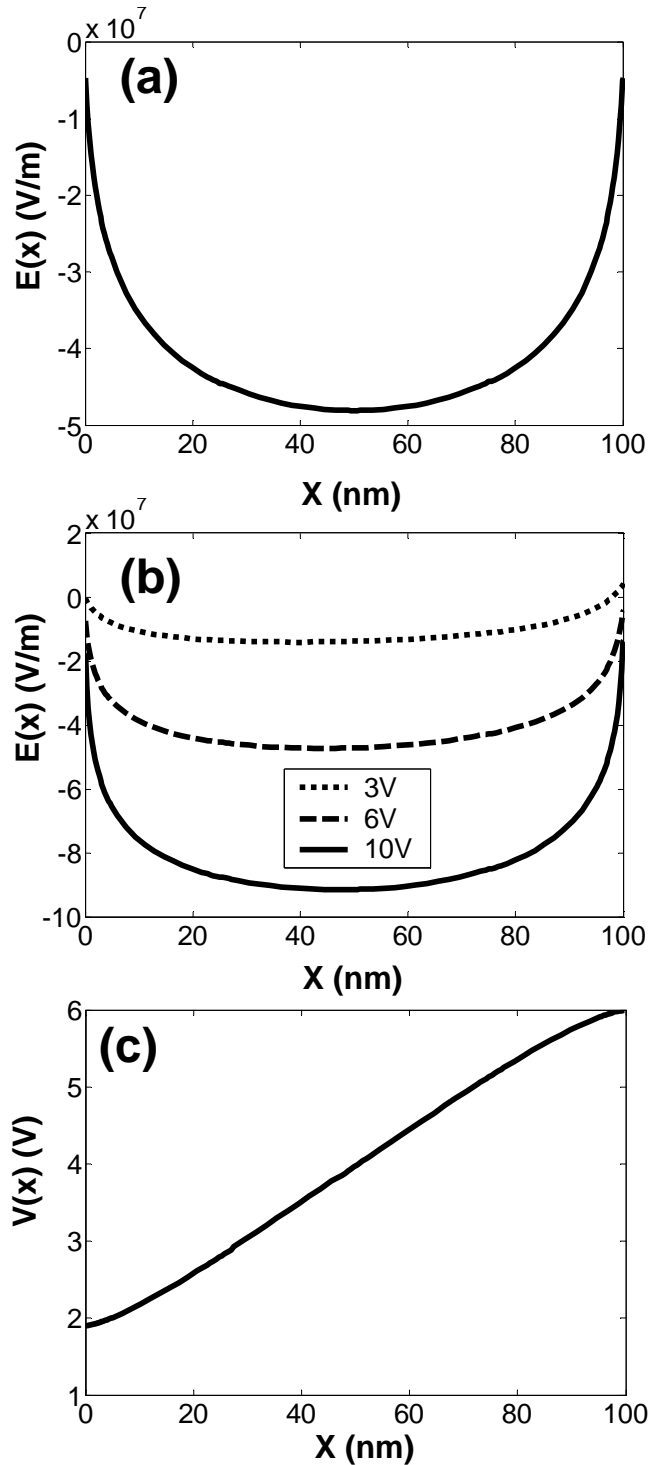line), and 10V (solid line) are presented in (b) and (c).
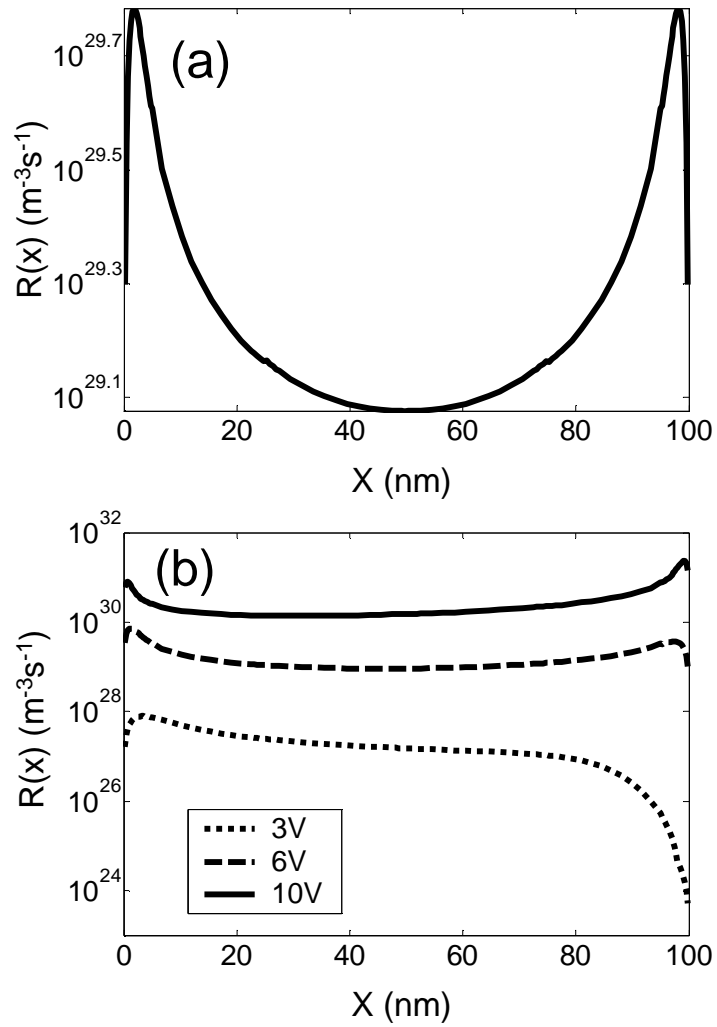
Figure 4.17: The recombination rate profiles for the double carrier devices in fig. 4.14: (a) is for symmetric device in fig. 4.14(a); (b) is for asymmetric device in fig. 4.14(b). The profile variation for voltage as 3V (dotted line), 6V (dashed line), and 10V (solid line) are presented in (b).
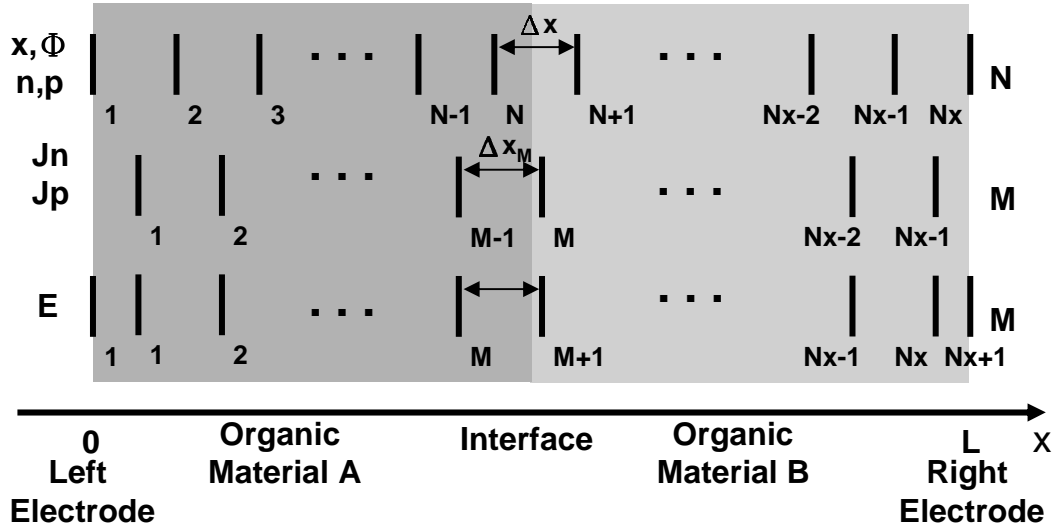
Figure 4.18: Gridding scheme for device model of multilayer devices. N labels gridpoints, and M labels half-gridpoints[6].

include interface as an internal boundary condition. The method used here can be extended to the case with more than two layers very easily.

4.3.1 Internal boundary conditions for the interfaces

Heterojunction organic LEDs are able to block the transport of carriers across the device either by an energetic barrier due to offset of the energy levels between the materials or by a transport barrier due to a disparity of carrier mobilities in the two organic materials[14, 15].

The introduction of an internal interface requires a modification in the solution of the continuity, Poisson's, and drift-diffusion equations presented in section 4.1.2. The gridding, shown in Fig. 4.18, is the same as for the single layer case[45, 118]. The equations to solve are again the continuity, Poisson's, and the drift-diffusion equations. The equations are discretized for numerical solution using the same procedure as in the single layer case presented in section 4.1.4, except for the grid element which includes the heterojunction interface. At this interface discontinuities of the material parameters can lead to discontinuities in the carrier densities, current densities, electric field, or electrostatic potential which must be included as an internal boundary condition in the solution. In this work the interface is assumed to be free of sheets of free charge, or recombination, so there is continuity of the electric displacement εE, the electrostatic potential ϕ, and the electron and hole
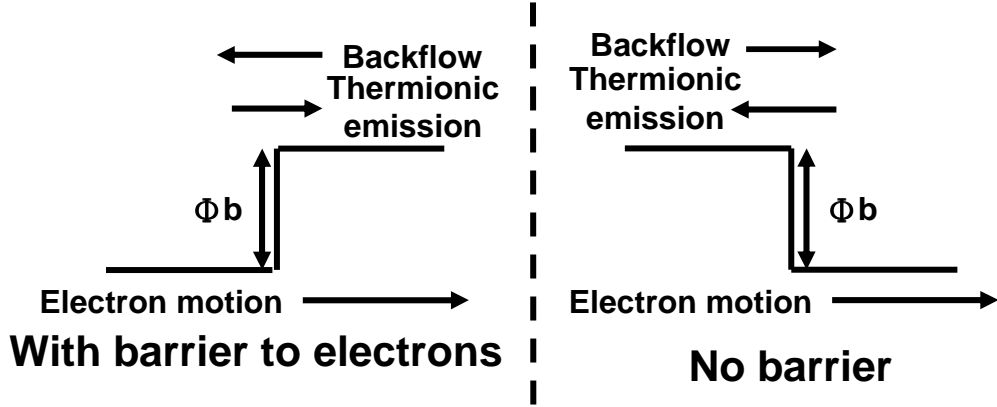
Figure 4.19: Schematic of the boundary conditions used at the heterojunction.

current densities J_n, J_p across the interface. Therefore the continuity and Poisson's equation can be discretized as for the single layer case. There is however a discontinuity in the carrier densities which must be included in discretization of the drift-diffusion relations.

4.3.2   Physical model for the internal boundary conditions

The carrier density discontinuity is obtained by considering the current processes at the interface. This is similar to the problem of the metal organic interface discussed in section 4.1.1, however since it is an organic-organic interface, tunneling and image force lowering are neglected, and only thermionic emission and backflowing currents are considered[45]. The thermionic emission and backflowing current are assumed to be fast processes which act to maintain quasithermal equilibrium at the heterojunction interface. The device current is assumed to be a relatively slow process which tends to pull the interface out of quasithermal equilibrium, but is too small to succeed. The possible barriers for electrons are illustrated in Fig. 4.19. Assuming a single energy level for injection as in section 4.1.1, the currents can be written for the two cases. for the case of no barrier the electron thermionic emission current can be written:

$$J_{th} = e\nu_2 n(x_0^+)e^{-\Phi_b/k_B T} = e\nu_2 n(x_0^+)e^{-(E_{c1}-E_{c2})/k_B T}, \qquad (4.48)$$

and the electron backflowing current is given by:

$$J_{bf} = e\nu_1 n(x_0^-), \tag{4.49}$$

so the total electron current is:

$$J_n = e^{E_{c2}/k_B T}(e\nu_2 n(x_0^+)e^{-E_{c1}/k_B T} - e\nu_1 n(x_0^-)e^{-E_{c2}/k_B T}). \tag{4.50}$$

For the case with a barrier to electrons, the electron thermionic emission current is:

$$J_{th} = e\nu_2 n(x_0^-)e^{-\Phi_b/k_B T} = e\nu_2 n(x_0^-)e^{-(E_{c2}-E_{c1})/k_B T}, \tag{4.51}$$

the electron backflow current is:

$$J_{bf} = e\nu_2 n(x_0^+), \tag{4.52}$$

resulting in a total current of:

$$J_n = e^{E_{c1}/k_B T}(e\nu_2 n(x_0^+)e^{-E_{c1}/k_B T} - e\nu_1 n(x_0^-)e^{-E_{c2}/k_B T}). \tag{4.53}$$

In either case the electron current can be written

$$J_n = e^{-E_c^>/k_B T}(e\nu_2 n(x_0^+)e^{E_{c2}/k_B T} - e\nu_1 n(x_0^-)e^{E_{c1}/k_B T}), \tag{4.54}$$

where $E_c^>$ is E_{c2} for the case of no barrier, and E_{c1} for the case of a electron barrier.

At thermal equilibrium the carrier densities just to the left and right of the interface have the ratio:

$$\frac{n(x_0^-)}{n(x_0^+)} = \frac{n_{01}e^{-(E_{c1}-E_f)/k_B T}}{n_{02}e^{-(E_{c2}-E_f)/k_B T}} = \frac{n_{01}}{n_{02}}e^{-(E_{c1}-E_{c2})/k_B T}. \tag{4.55}$$

The current density at thermal equilibrium is zero, so Eq.4.54 gives:

$$\frac{n(x_0^-)}{n(x_0^+)} = \frac{\nu_2}{\nu_1}e^{-(E_{c1}-E_{c2})/k_B T}, \tag{4.56}$$

comparing Eqs.4.55 and 4.56:

$$\frac{\nu_2}{\nu_1} = \frac{n_{01}}{n_{02}}, \Rightarrow \nu_2 = \frac{\gamma}{n_{02}}, \nu_1 = \frac{\gamma}{n_{01}}, \tag{4.57}$$

where γ is the kinetic coefficient for thermionic emission, and is taken as AT^2. As was the case for the metal organic interface, a large value of γ maintains quasithermal equilibrium at the interface, so that the carrier densities at the interface are given by the quasithermal equilibrium values, and the details of the thermionic emission and backflow processes are not important.

4.3.3   Bipolar device model results

From the results for the bipolar single layer device, we know that as the voltage increases, the recombination rate profile shifts from the cathode to the anode. In order to let the multilayer LED emit various colors, three different kinds of emitting layer with different electroluminescent spectrum must be included in the device. There will be energy barrier between heterojunction interface. Since, for most of the organic materials, the electric field dependence factor of the electron mobility is larger than that of hole, the recombination rate profile will be dominated by the profile of the electron density. In order to clarify how the interface electron barrier affect the electron density distribution, then the recombination rate profile, as voltage increase, we calculate the electric field, carrier density, and recombination rate for the bilayer device with electron barrier in the heterojunction interface. Since unipolar LED can not emit light, we examine bipolar case for bilayer device directly.

Figure 4.20 presents the structures of two double carrier bilayer devices. Each layer has the thickness of 50nm, the difference for these two layer is that the LUMO for the material of the right side is 2.8eV and that for the material of the left side is 3.0eV. Such LUMO deviation introduce a electron barrier between these two layers. Fig. 4.20(a) shows the case for the symmetric carrier mobility, Fig. 4.20(b) shows that for the asymmetric carrier mobility. The zero field carrier mobility, μ_0, and the field dependence factor, E_0, for the symmetric device (Fig. 4.20(a)) are $10^{-10}\text{m}^2/\text{Vs}$ and $4.3 \times 10^6\text{V/m}$ respectively. Fig. 4.20(b) presents the case for asymmetric carrier mobility. The zero field hole (electron) mobility, μ_{0h} (μ_{0e}), and the field dependence factor, E_{0h} (E_{0e}), for the asymmetric device are μ_0 ($0.1 \times \mu_0$) and $4.3 \times 10^6\text{V/m}$ ($1.6 \times 10^6\text{V/m}$) respectively.

Figure 4.21 demonstrates the electric field profiles for the two devices in fig. 4.20. Fig. 4.21(a) is for the case of symmetric carrier mobilities, Fig. 4.21(b) is for the case of asymmetric carrier mobilities. Fig. 4.21(b) presents the electric field profile variation for voltage as 3V (dotted line), 6V (dashed line), and 10V (solid line). Because of the discontinuities for the carrier density (electron) across the interface, the electric field around the interface shows a sudden jump. Since the electron density on the right side material is much lower than that of the left side material, higher electric field is needed to provide steady current for the right side material. In Fig. 4.21(b), the electric field jump beside the heterojunction for low voltage is smaller than that for high voltage.

Figure 4.22 shows the electron and hole density profiles for the two devices in Fig. 4.20. Fig. 4.22(a) presents the electron and hole density for the case
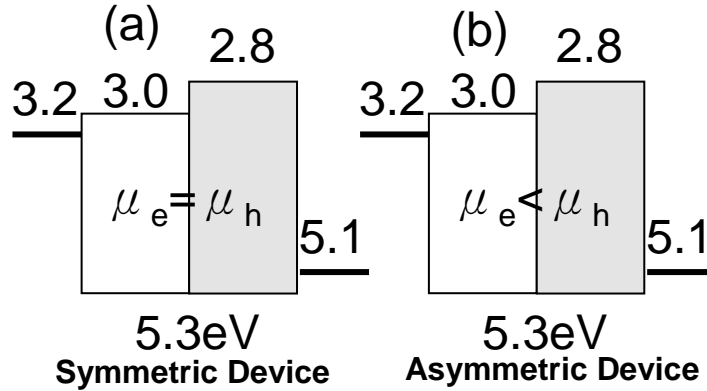
Figure 4.20: The structures of the double carrier bilayer devices with (a) symmetric and (b) asymmetric carrier mobility.

of symmetric carrier mobility. Figs. 4.22(b) and (c) show the electron and hole density for the case of asymmetric carrier mobility respectively. The carrier density profiles variation for varying voltage as 3V (dotted line), 6V (dashed line), and 10V (solid line) are shown in Figs. 4.22(b) (electron) and (c) (hole). In Fig. 4.22(a), electron density has a sudden jump in the interface due to the electron barrier introduced by the heterojunction. The hole density, which has no energy barrier beside the junction, is not smooth across the heterojunction, because the hole density must deviate from its smooth value to match the electron density to satisfy the requirement of steady state current density. In Fig. 4.22(b), the electron density for low voltage (3V) decreases rapidly on the material of the right side. As the voltage being 6V, more electrons can reach the right contact. As the voltage being even higher to 10V, the electron density is raised to about one order magnitude larger than that just across the junction, owing to the attraction from the high density of holes injected from the contact of the right side with a small injection barrier. In Fig. 4.22(c), the density of hole also demonstrate the deviation behavior to match the sudden jump of the electron density around the interface. As the voltage increases, the deviation gets larger, and more hole can reach the contact of the left side.

Figure 4.23 demonstrates the recombination rate profiles for the two devices in Fig. 4.20. Fig. 4.23(a) is for the case of symmetric carrier electron mobility, Fig. 4.22(b) is for that of asymmetric carrier electron. Fig. 4.21(b) presents the recombination rate profiles variation for voltage as 3V (dotted line), 6V (dashed line), and 10V (solid line). In Fig. 4.23(a), for the case of the symmetric carrier mobility, the recombination rate on the right side

Figure 4.21: The electric fields profiles for the two double carrier bilayer devices in fig. 4.20: (a) is for symmetric device in fig. 4.20(a); (b) is for asymmetric device in fig. 4.20(b). The profiles variation for voltage as 3V (dotted line), 6V (dashed line), and 10V (solid line) are presented.
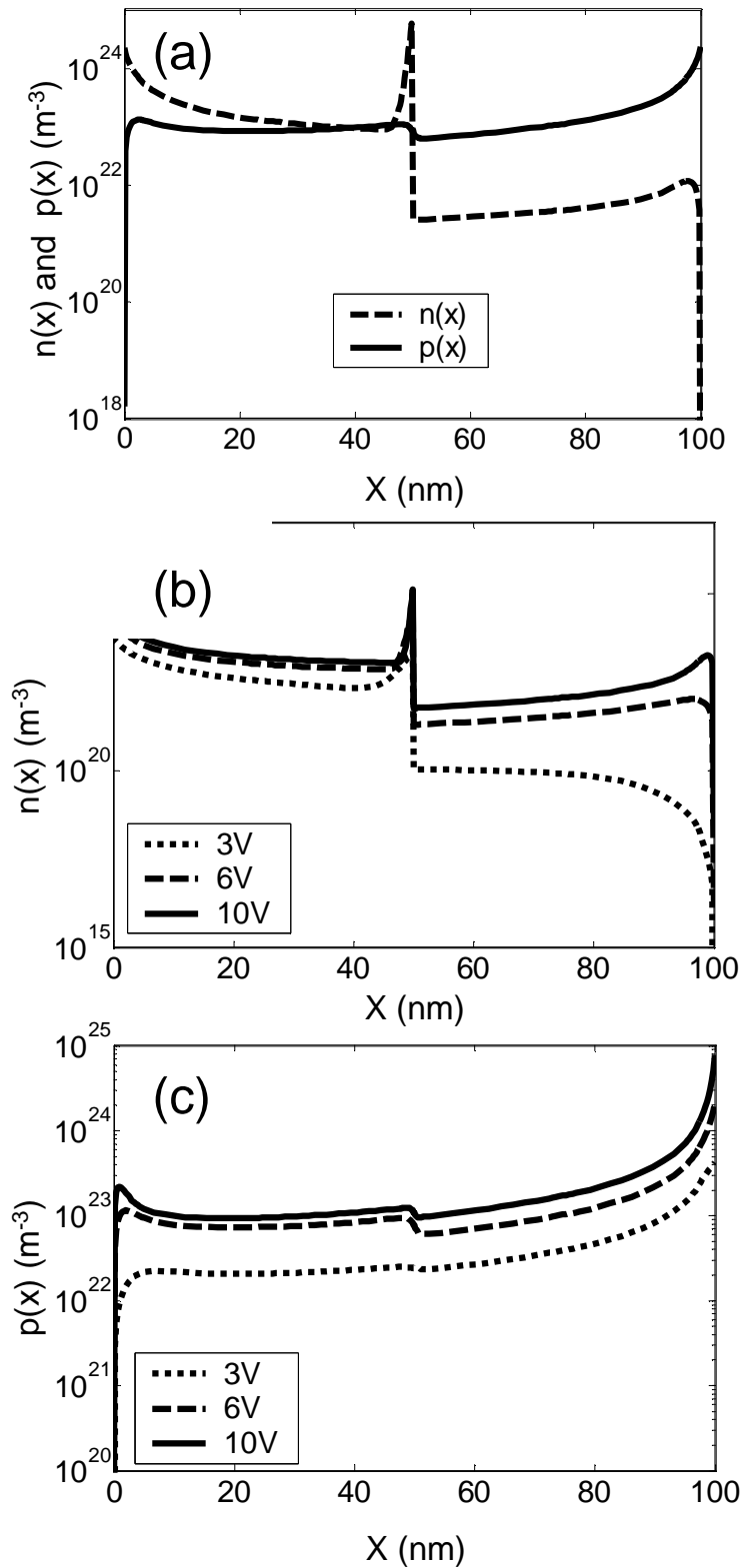
Figure 4.22: (a) The electron (dashed line) and hole (solid line) density profiles for the symmetric double carrier bilayer device in fig. 4.20(a); (b) the electron and (c) hole density profile for the asymmetric double carrier bilayer device in fig. 4.20(b). The profile variation for voltage as 3V (dotted line), 6V (dashed line), and 10V (solid line) are presented in (b) and (c).

beside the junction keeps a large fall with that on the left side beside the junction. In Fig. 4.23(b), for the case of the asymmetric carrier mobility, as the bias being low voltage (3V), the rate profile jump around the junction is broad and the rate profile on the material of the right side decays rapidly near the the contact of the right side. As the bias increases, the rate profile jump around the junction is getting more narrow and higher and the rate profile on the material of the right side is lifted to a level being able to compete with that of the left side. Hence, the recombination rate profile for the multilayer organic LED, which has asymmetric carrier mobility, can shift from cathode to anode as voltage increases.

In summary, results of device model with electron barrier heterojunction and asymmetric carrier mobility are presented. Recombination rate profiles for symmetric and asymmetric carrier mobility shows that as the device voltage increases, the jump of the rate profile is getting more narrow and higher. The higher jump of the rate profile near the junction lifts the the rate profile near the hole injection contact to a level being able to compete with that near the electron injection contact. The profile variation as increasing voltage for the case of asymmetric carrier mobility shows the exciton recombination zone shifting toward the hole injecting side. This profile shifting due to voltage increasing is the basic principle for the color-tuning mechanism of the multilayer LED.
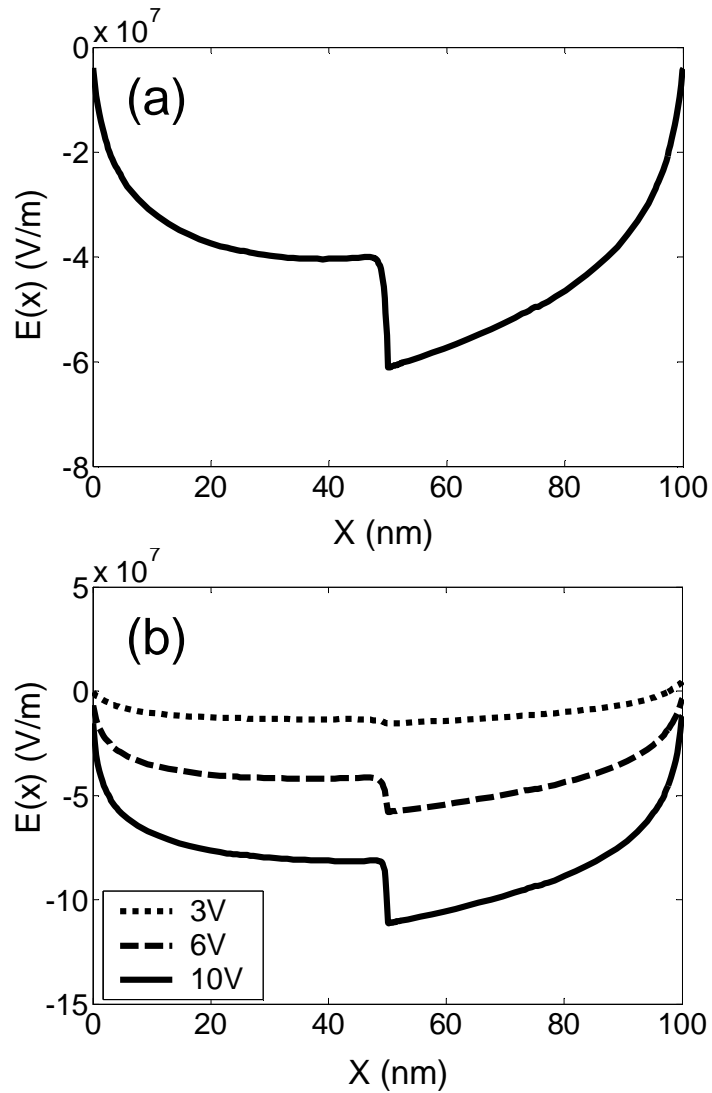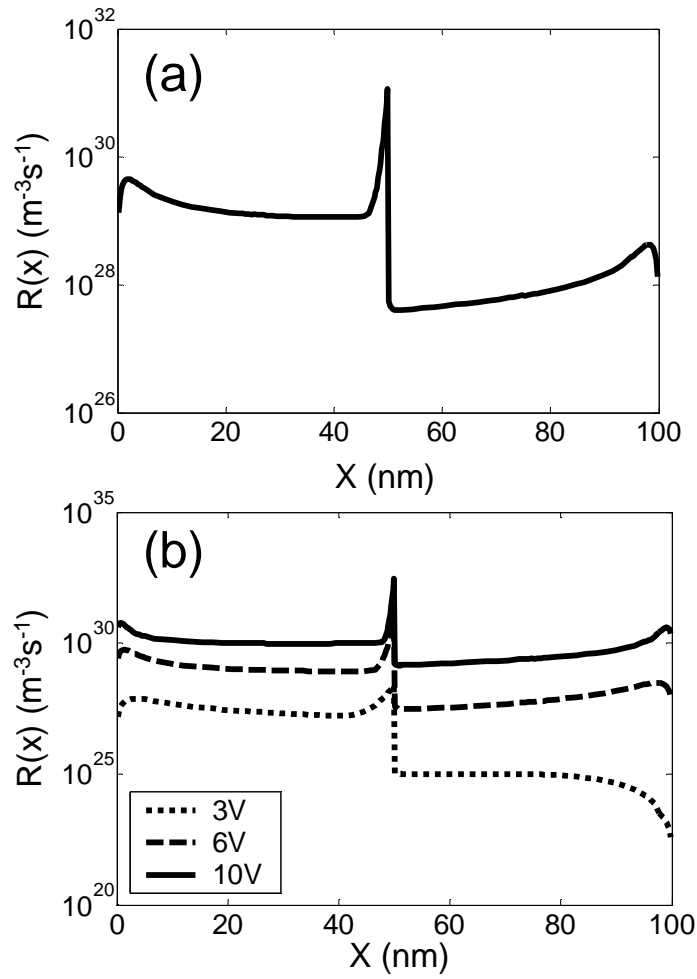
Figure 4.23: The recombination rate profiles for the double carrier bilayer devices in fig. 4.20: (a) is for symmetric device in fig. 4.20(a); (b) is for asymmetric device in fig. 4.20(b). The profile variation for voltage as 3V (dotted line), 6V (dashed line), and 10V (solid line) are presented in (b).
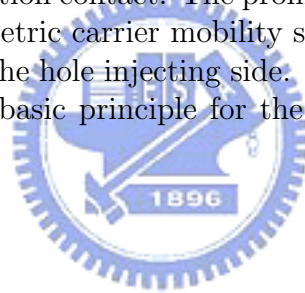
4.4   Color-tunable multilayer polymer LED

According to the results from last sections, recombination rate profile can shift from cathode to anode as voltage increases. Extending the numeric method to treat the heterojunction as internal boundary condition for the double-layer device, we can calculate the color-tunable device with four layers very easily. At first we define recombination current ratio for each layer, then examine the influences on the ratio as varying some important parameters, i.e. heterojunction energy barriers, carrier mobilities, and layer thickness. Based on the result deduced from the relation between the ratio and these parameters, we propose two device structures with color-tuning function.

The recombination current for the red, green, and blue emitting layer is expressed as

$$J_r^R = \int_0^{x_1} eR(x)dx, \tag{4.58}$$

$$J_r^G = \int_{x_1}^{x_2} eR(x)dx, \tag{4.59}$$

and

$$J_r^B = \int_{x_2}^{x_3} eR(x)dx \tag{4.60}$$

respectively, where x_1, x_2, and x_3 denote the position of the interface between the red and green layers, the green and blue layers, and the blue and electron blocking layers respectively. The relative recombination ratio for each layer to the red layer, $r_{R,G,B}$, where $r_R = J_r^R/J_r^R = 1$, $r_G = J_r^G/J_r^R$, and $r_B = J_r^B/J_r^R$, measures the relative exciton recombination efficiency of each layer. Multiplying this ratio by the relative exciton radiation efficiency, $\eta_{R,G,B}$, for each layer produces the relative internal quantum efficiency, $R_{R,G,B} = \eta_{R,G,B} \times r_{R,G,B}$, for each device layer.

4.4.1   Varying energy barrier for interface

Figure 4.24 shows the device structure to vary the electron barrier between the green and the blue layer, $\Delta\Phi_{eGB}$, and the electron barrier between the blue and the electron blocking layer, $\Delta\Phi_{eBE}$. We at first vary $\Delta\Phi_{eGB}$ from 0.1eV to 0.3eV, and keep $\Delta\Phi_{eBE}$ as 0.3eV. Then, $\Delta\Phi_{eBE}$ is varied from 0.1eV to 0.6eV, and $\Delta\Phi_{eGB}$ is kept as 0.1eV. The zero field hole (electron) mobility, μ_{0h} (μ_{0e}), and the field dependence factor, E_{0h} (E_{0e}), for device are μ_0 ($0.1 \times \mu_0$) and 4.3×10^6V/m (1.6×10^6V/m) respectively.
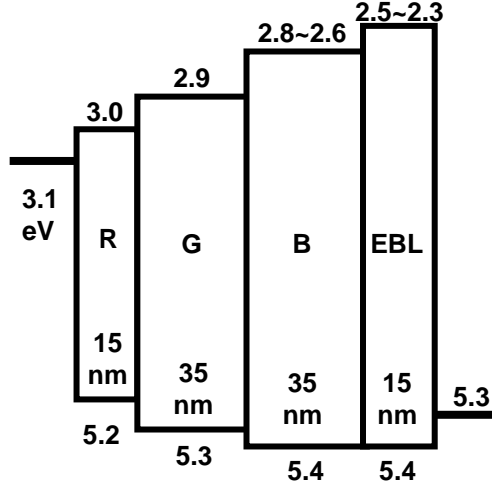
Figure 4.24: The device structures for varying the electron energy barrier between the green and blue layers, $\Delta\Phi_{eGB}$, and the blue and electron blocking layer, $\Delta\Phi_{eBE}$. As varying $\Delta\Phi_{eGB}$ from 0.1eV to 0.3eV, $\Delta\Phi_{eBE}$ is kept as 0.3eV. As varying $\Delta\Phi_{eBE}$ from 0.1eV to 0.6eV, $\Delta\Phi_{eGB}$ is kept as 0.1eV.

Because of the high mobility of the holes, and hole distribution is rather uniform through out the layers except for the sudden fall and rise at the junctions. On the other hand, the electron density decreases strongly from the cathode typical for the low-mobility space-charge-limited current and it is quite difficult for the electrons to not only reach the junction but also jump through it. The recombination distribution R(x), proportional to n(x)p(x), is therefore dominated by the behavior of n(x). Fig. 4.25(a) illustrates how the electron interface energy barrier between the green and blue layers, $\Delta\Phi_{eGB}$, influences R(x) for the device voltage 10V. As $\Delta\Phi_{eGB}$ increases from 0.1eV to 0.3eV, the R(x) for the green layer changes not much, but the R(x) for the blue layer decreases dramatically. Fig. 4.25(b) shows the relative recombination ratios, $r_{R,G,B}$, among the luminescent layers, as functions of the barrier, $\Delta\Phi_{eGB}$. As $\Delta\Phi_{eGB}$ increases from 0.1eV to 0.3eV, r_G grows from 1.2 to 2.8 and r_B decays from 1.8 to almost zero. Fig. 4.26(a) presents how the electron interface energy barrier between the blue and electron blocking layers, $\Delta\Phi_{eBE}$, influences R(x) for the device voltage 10V. As $\Delta\Phi_{eBE}$ increases from 0.1eV to 0.6eV, the R(x) for the green and blue layers change not much, but the R(x) for the electron blocking layer decreases dramatically. Fig. 4.26(b) shows the relative recombination ratios, $r_{R,G,B}$, among the luminescent layers, as functions of the barrier, $\Delta\Phi_{eBE}$. The value of r_G keeps almost constant as varying $\Delta\Phi_{eBE}$ from 0.1eV to 0.6eV. As $\Delta\Phi_{eGB}$ ranges

from 0.1eV to 0.3eV, the value of r_B grows rapidly from 1.0 to 1.75. As $\Delta\Phi_{eGB}$ ranges from 0.3eV to 0.6eV, the value of r_B changes not much. The result shows that a barrier about 0.3eV, which is introduced in the interface between the blue and electron blocking layers, is satisfied to block electron to traverse through the blue layer.

4.4.2   Varying mobilities for each layer

Even though the electron mobility is typically several orders of magnitude smaller than the hole mobility, there exist some highly emissive materials for which the mobilities are not so asymmetric. It is therefore important to know how the mobility ratio influences the color tunability. Fig. 4.28(a) demonstrates how the zero field electron mobility of the green layer, μ_{eG}, determines the R(x) of the device. Define μ_{eG}/μ_{hG} as m_G and μ_{eB}/μ_{hB} as m_B. As m_G decreases from 1.0 to 0.001, the recombination distribution zone for the green layer shifts from the right side to the left side obviously. Fig. 4.29(a) shows how m_G influences $r_{G,B}$. As m_G being around 0.1, both r_G and r_B have such values that color-tuning can be expected. Figs. 4.28(b) and 4.29(b), demonstrate how the zero field electron mobility of the blue layer, μ_{eB}, determines the R(x) and $r_{G,B}$ of the device. Increasing m_B will increases r_B approximately linearly, but the influence on r_G is suppressed owing to the faster electron mobility of the blue layer preventing the pile-up of electrons between the green and blue layers from raising r_G. Since the value of m_G is more crucial than the value of m_B for the purpose of color-tuning, we magnify the order of varying range of m_G to clarify its effect on recombination rate profiles and recombination ratios of the device.

4.4.3   Varying film thickness for each layer

Figures 4.31 and 4.32 demonstrate the effect of the thickness for the green (L_G) and the blue (L_B) layer on the R(x) and the value of $r_{G,B}$. r_G is clearly proportional to the green layer thickness, L_G; the value of r_B is also proportional to L_G, but less obviously than r_G. Nevertheless, the blue layer thickness, L_B, has no effect on r_G, but have a linear increasing effect on r_B.

4.4.4   Device structures and their simulation results

A color-tuning structure should have to tune the color from red to green then to blue as increasing bias, and the red light ratio should dominate over other colors for low voltage, while the green should dominate around medium and high voltage, and the blue should increase rapidly for high voltage. Fig. 4.33

Figure 4.25: The recombination rate profiles for the device varying (a) $\Delta\Phi_{eGB}$ and (b) $\Delta\Phi_{eBE}$.
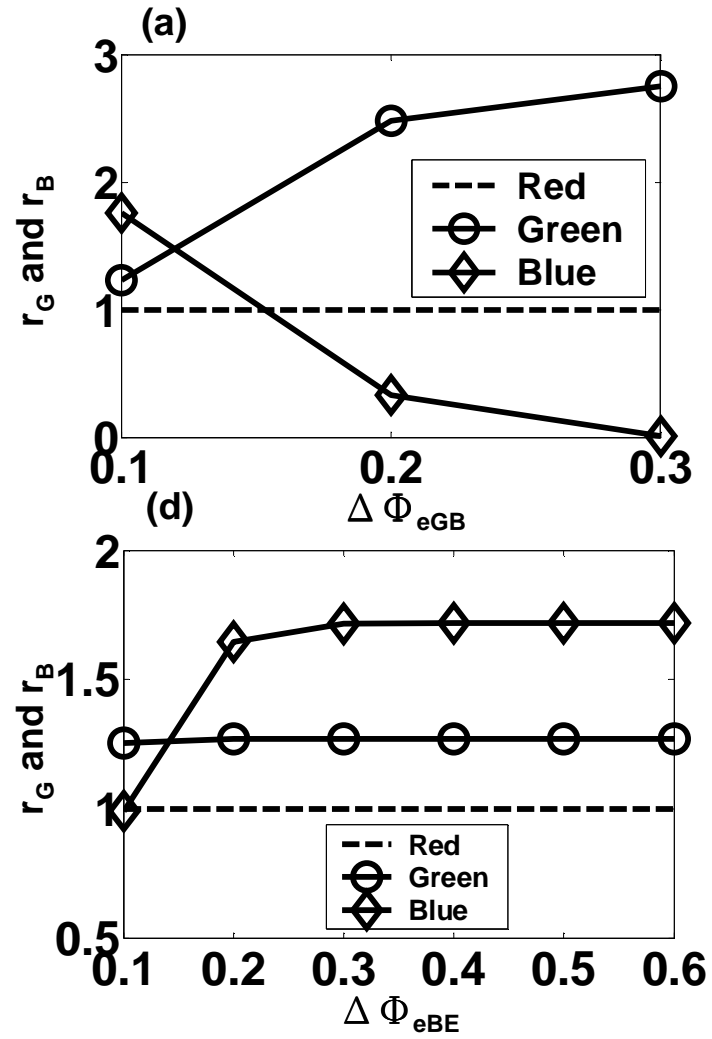
Figure 4.26: The recombination ratios as functions of (a) $\Delta\Phi_{eGB}$ and (b) $\Delta\Phi_{eGB}$.
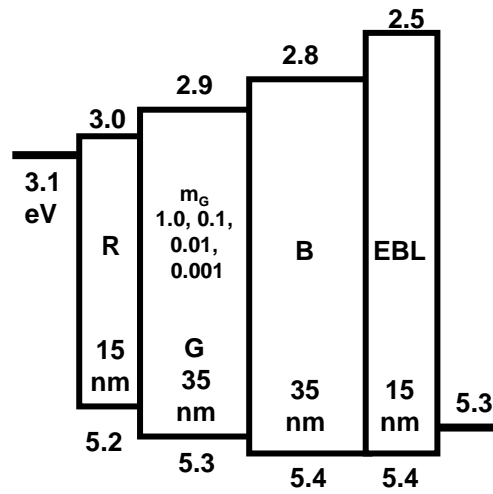
Figure 4.27: The device structures for varying the ratio of the electron zero field mobility to the hole zero field mobility for the green layer, m_G, and for blue layer, m_B. m_G ranges from 1.0, 0.1, 0.01, and to 0.001; m_B ranges from 0.2, 0.1, 0.05, and to 0.025.

displays the device structures for two color-tuning LEDs. One color-tuning structure has faster zero field electron mobility of the green layer (mG=0.2) than that of the other layer (the ratio of zero field electron mobility to that of hole is 0.1) (device A). η_R and η_G for device A are specified as one and η_B as 2. Device B has a thicker green layer (50nm) and a thinner blue layer (20nm), and the zero field electron mobilities for each layer are all one order of magnitude smaller than that of hole. η_R and η_G for device B are taken as one and η_B as 3. The electron affinity (EA) and ionization potential (IP) for each layer are chosen to be matching the proper energy gap to emit expected color for each layer. In order to rise r_G rapidly, the EA for the red and green layers are chosen to be the same. However, a 0.2eV barrier between the green and blue layers will make r_G dominating over medium voltage range. The 0.4eV barrier between the blue and electron blocking layer will let r_B grows rapidly near high voltage.

Figure 4.34 presents the electron density (Fig. 4.34(a)), the hole density (Fig. 4.34(b)), and the recombination rate profile (Fig. 4.34(c)) for device A. The electron density (Fig. 4.34(a)) of the blue layer for 3V is so low that the device emits red light. As the voltage increases to 10V and 13V, the electron density for the blue layer starts to compete with that for the green layer. The hole density (Fig. 4.34(b)) has sudden drops beside each interface. The abrupt drops are caused by efficient carrier "sweep-out" across the interface.
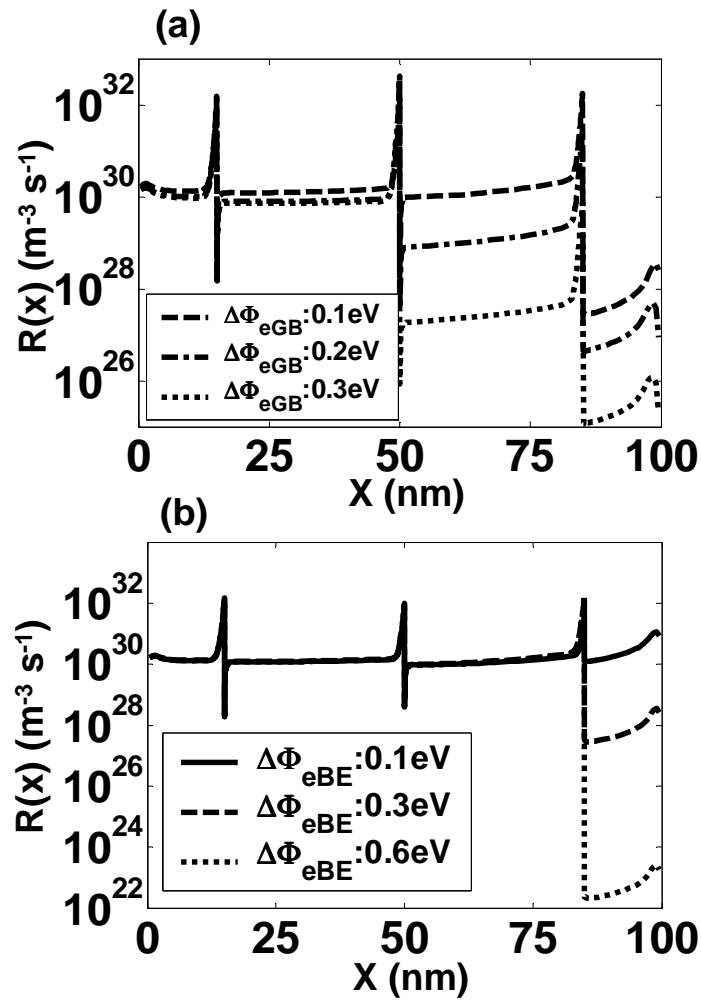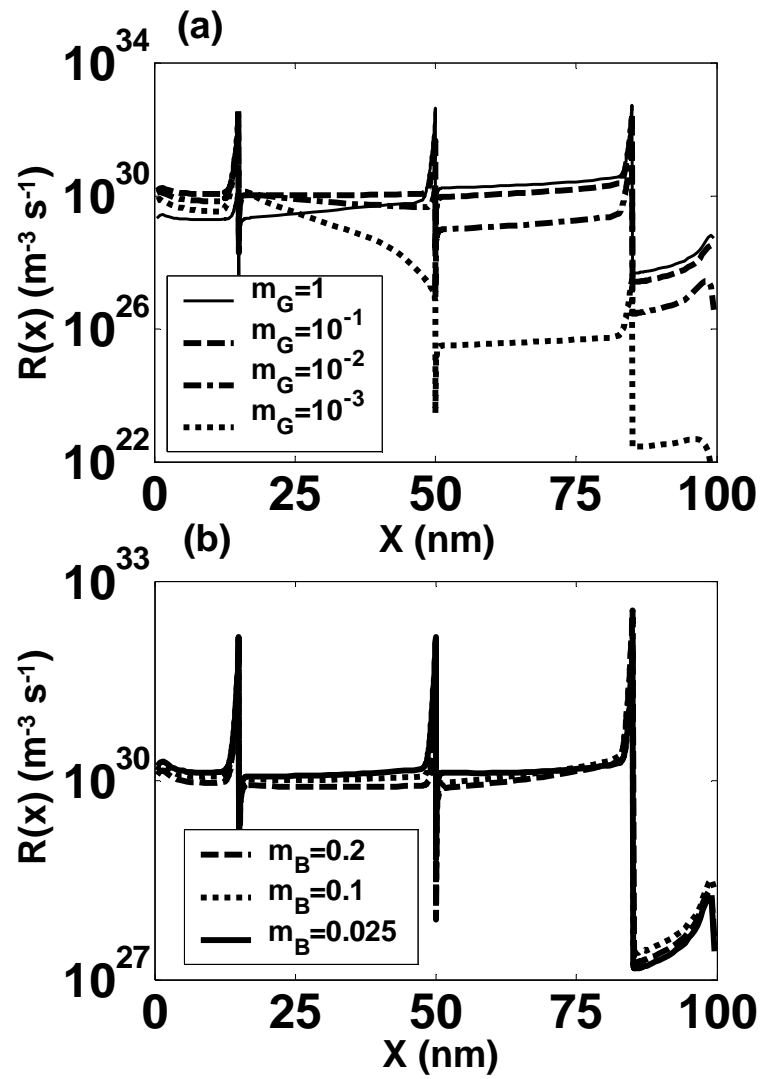
Figure 4.28: The recombination rate profiles for the device varying (a) m_G and (b) m_B.
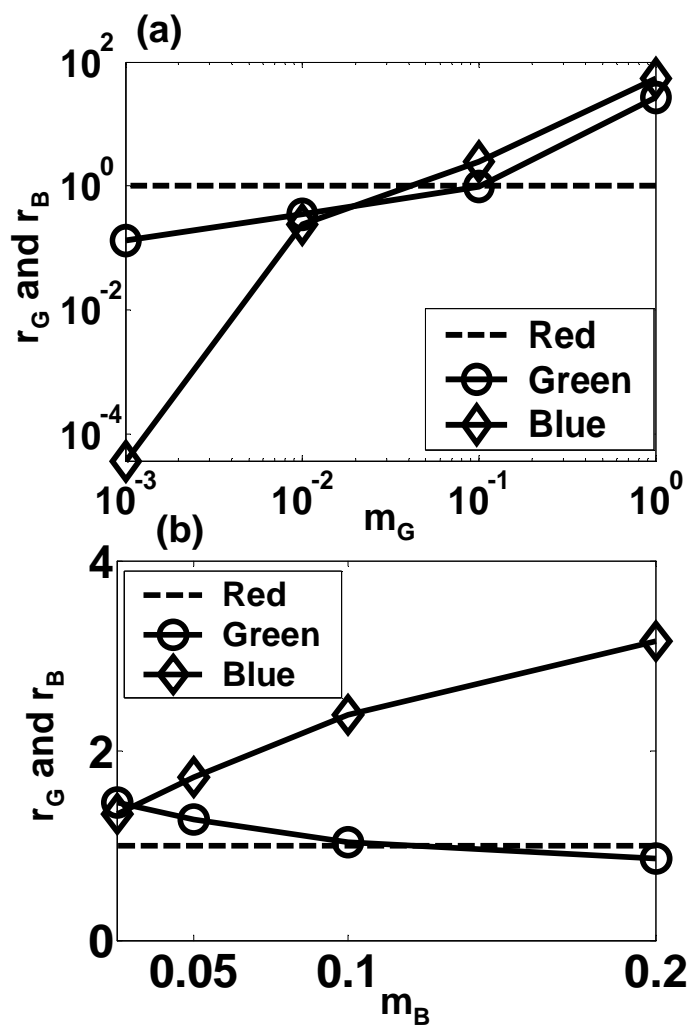
Figure 4.29: The recombination ratios as functions of (a) m_G and (b) m_B.
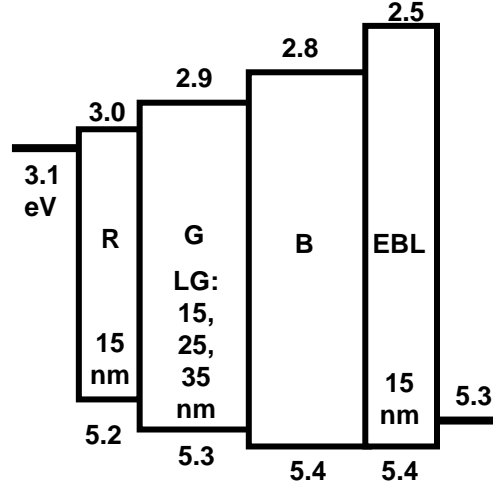
Figure 4.30: The structures for the devices varying layer thickness of the green layer (L_G) and the blue layer (L_B).

As the hole passes the interface, the past carrier can hardly "backflow" due to the large hole barrier. The recombination rate profile (Fig. 4.34(c)) of device A shows obvious growth of the contribution for the blue layer as the voltage increases.

To clarify the color-tuning effect, the CIE coordinates transition for bias change is calculated. The CIE coordinates are defined as[123] x=X/(X+Y+Z), y=Y/(X+Y+Z), and z =Z/(X+Y+Z), where

$$X = \int_{inv} s(\lambda)\bar{x}(\lambda)d\lambda, \tag{4.61}$$

$$Y = \int_{inv} s(\lambda)\bar{y}(\lambda)d\lambda, \tag{4.62}$$

and

$$Z = \int_{inv} s(\lambda)\bar{z}(\lambda)d\lambda. \tag{4.63}$$

"inv" means that the integration range is for the invisible light. The functions $\bar{x}(\lambda)$, $\bar{y}(\lambda)$, and $\bar{y}(\lambda)$ are CIE tristimulus values that define the primaries X, Y, and Z.

$$s(\lambda) = R_R R(\lambda) + R_G G(\lambda) + R_B B(\lambda), \tag{4.64}$$

the spectral responsivity emitting from the LED, represents the combination of all the luminescence spectra of the red, green, and blue layers of
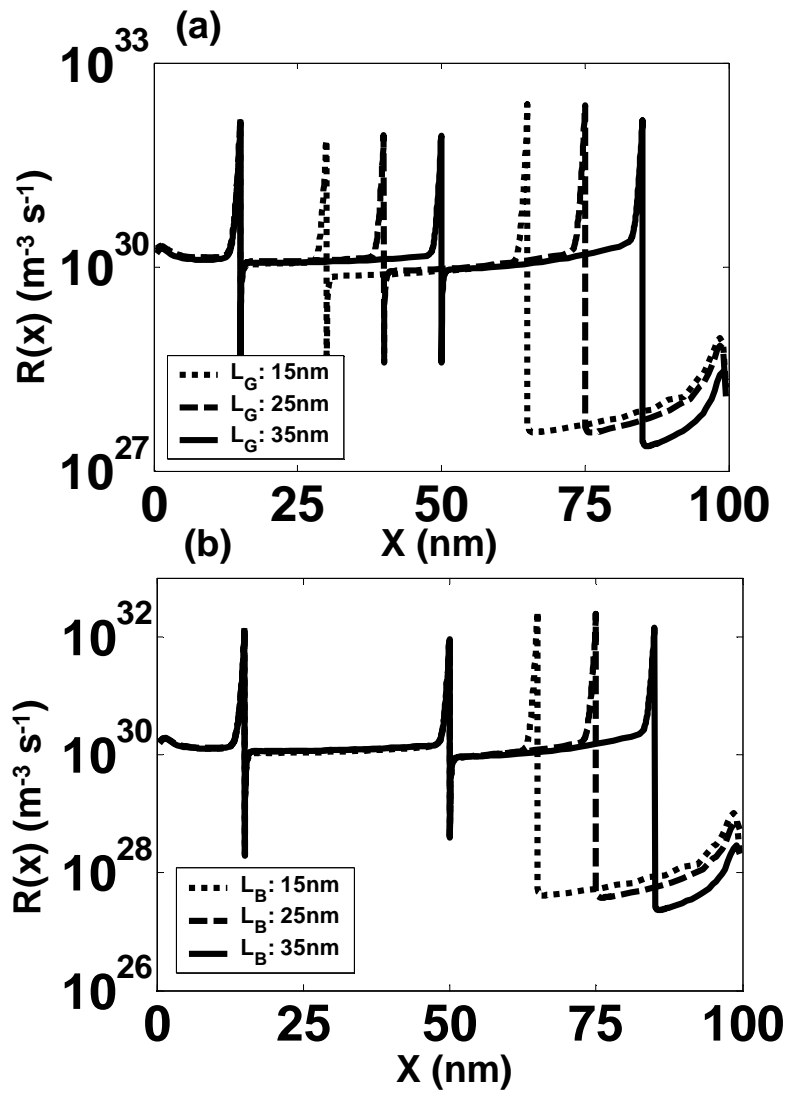
Figure 4.31: The recombination rate profiles for varying the layer thickness (a) L_G and (b) L_B.
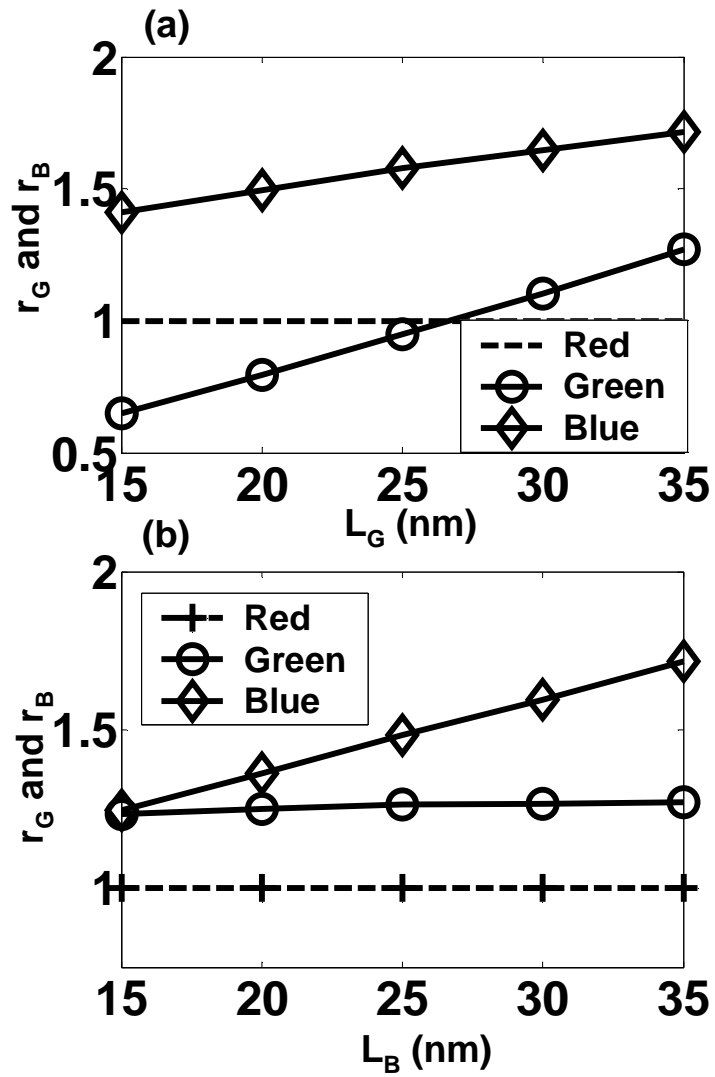
Figure 4.32: The recombination ratios for varying the layer thickness (a) L_G and (b) L_B.
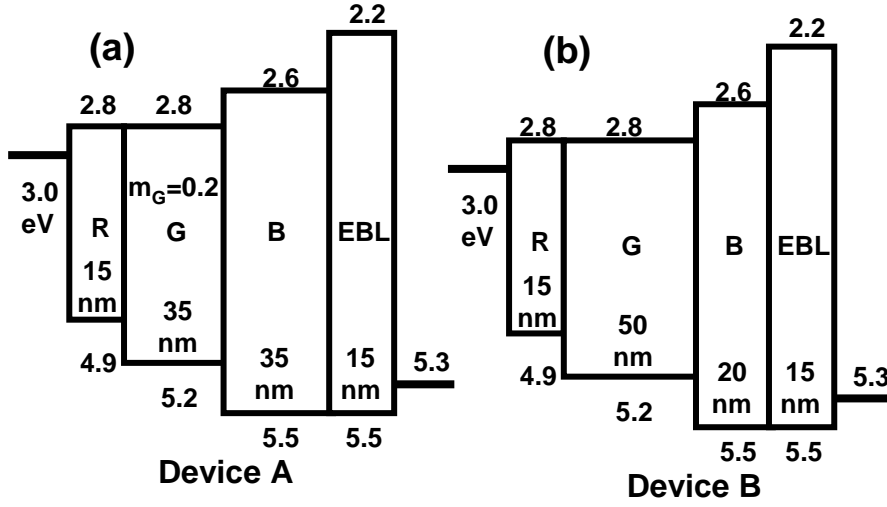
Figure 4.33: The structures of two color-tuning devices. Device A has a faster electron mobility for the green layer than that of the other layer. Device B has a thicker green layer (50nm and) and thinner blue layer (20nm).

the LED. $R(\lambda)$, $G(\lambda)$, and $B(\lambda)$ represent the luminescence spectra of the red, green, and blue color materials respectively; here they are assumed to demonstrate a normalized gaussian forms

$$R(\lambda) = \frac{1}{w_R\sqrt{2\pi}}e^{-\frac{(\lambda-\lambda_R)^2}{2w_R^2}} , \qquad (4.65)$$

$$G(\lambda) = \frac{1}{w_G\sqrt{2\pi}}e^{-\frac{(\lambda-\lambda_G)^2}{2w_G^2}} , \qquad (4.66)$$

and

$$B(\lambda) = \frac{1}{w_B\sqrt{2\pi}}e^{-\frac{(\lambda-\lambda_B)^2}{2w_B^2}} , \qquad (4.67)$$

where $\lambda_R = 600$nm, $\lambda_G = 520$nm, $\lambda_B = 440$nm, $w_R = 304$nm, $w_G = 30$nm, and $w_B = 20$nm.

Fig. 4.35 demonstrates the continuous motion of the CIE coordinates of device A and B. The three stars labelled with "Red", "Green", and "Blue" are where the phosphors of the typical red, green, and blue color monitor plots. The large open circle labelled with "White" is where the white color area is. The small black triangle beside "Red" star is the position for the spectrum peak of the red layer, the small black square is for that of the
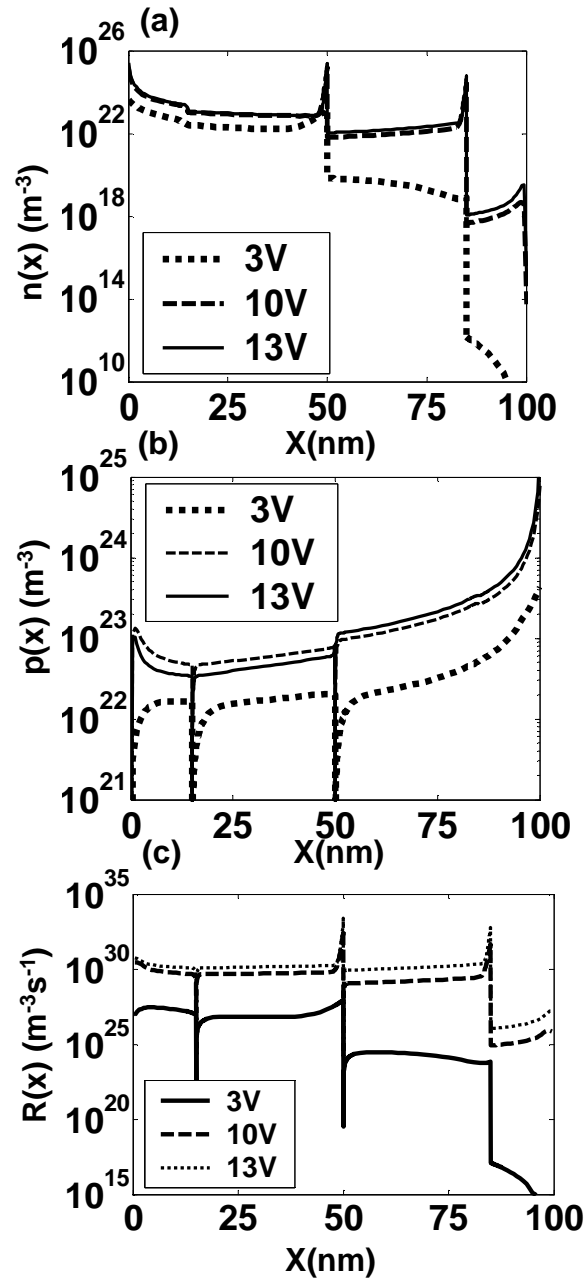
Figure 4.34: The (a) electron density, (b) the hole density, and (c) the recombination rate profile for the device A in Fig. 4.33.

green layer, and the small black diamond is for that of the blue layer. The trajectory of the CIE coordinates of device A are marked with open circles, that of device B are drawn with dashed line. Both of their transition paths go through red, green, and blue region. The inset shows the relative internal quantum efficiencies of device A and B from 3V to 13V. The contributions for the green layers of the device A (open circle) and B (dashed line) all start from the values about one and grow gradually to high voltage. However, the contributions for the blue layers of the device A (open diamond) and B (dotted line) all start from values about zero and grow rapidly to high voltage.

4.4.5 Discussion

Individual layer thickness can be controlled easily in both small molecule and polymer semiconductors via the deposition and spin-coating conditions, respectively. Increasing mobility for certain materials is difficult, but reducing the mobility for one layer is equivalent to increasing the mobility for other layers. Mobility may be decreased by doping some particles with suppressed effect on transport but with minimal influence on the luminance into luminescent layer. Synthesis of increasing number of materials, whether small molecules or polymers, with familiar luminescence color has provided suitable materials with proper energy level alignment for use in the proposed structures. Owing to solution mixing problems between each layer for polymer materials, the definiteness of the interface formation for polymeric structure is poor. The results of this work should be more applicable to devices comprised with small molecules.

Figure 4.36(a) presents the structure for a bilayer color-tunable LED, which is comprised with a green layer (PF(G)) and a red layer (PF(R)). From the spectra in fig. 4.36(b), we can see that at high voltage (12V) the peak of the spectrum centers at 532 nm, which is just the peak for the green layer material, PF(G). But the color is like yellow, not green. If we alternate the green layer with a mixed layer (fig. 4.37(a)), which is composed of blue PF(B) and green $DPOC_{1}0$ with the weight ratio 10:1, at high voltage, the peak of the spectrum centers at 500nm (fig. 4.41(b)), which looks more greener than the case in fig. 4.36. These experiments give an evidence that a green layer close to blue color will get better color-tuning effect.

4.4.6 Conclusion

In summary, we establish a theoretical model which is able to obtain the carrier and recombination distribution in organic multilayer LED for arbitrary
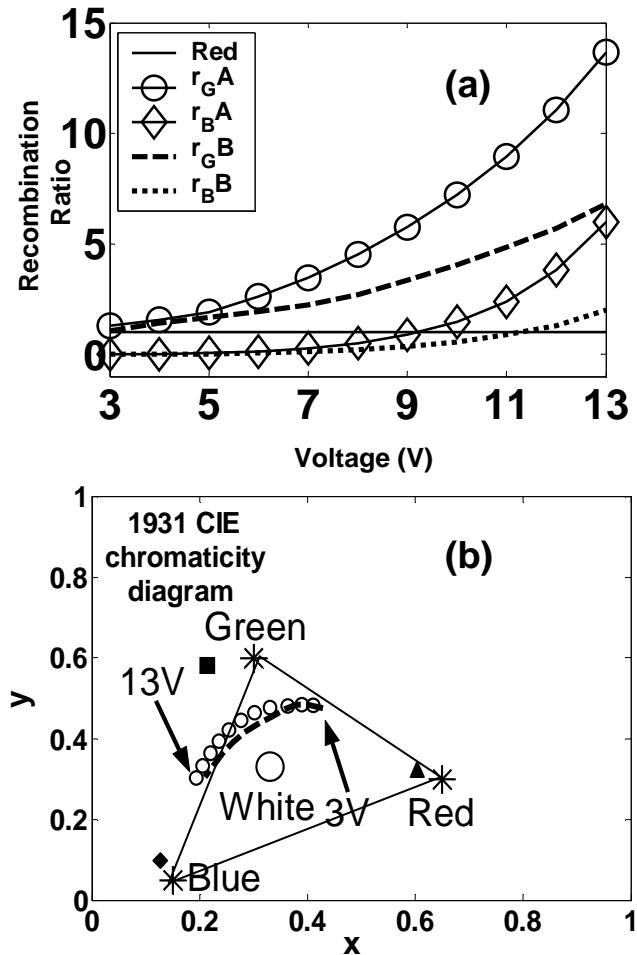
Figure 4.35: The continuous motion of the CIE coordinates for device A (small open circle) and B (dashed line). The inset shows relative recombination ratio of each layer for device A (green: open circle; blue: open diamond) and B (green: dashed line; blue: dotted line). The three stars labelled with "Red", "Green", and "Blue" are defined by the phosphors of the typical red, green, and blue color monitor plots. The large open circle label;ed with "White" is where the white color area is. The small black triangle beside "Red" star is the position for the spectrum peak of the red layer, the small black square is for that of the green layer, and the small black diamond is for that of the blue layer.
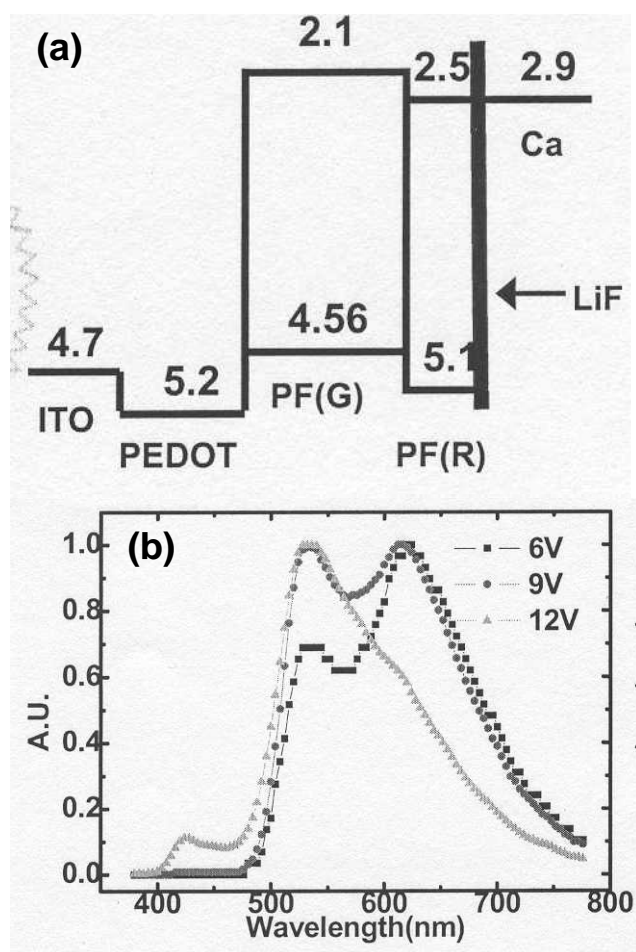
Figure 4.36: (a)Device structure for multilayer diode: PF(G)(60nm)/PF(R)(10nm)-LiF(6nm); (b)Spectra for upper device[7].
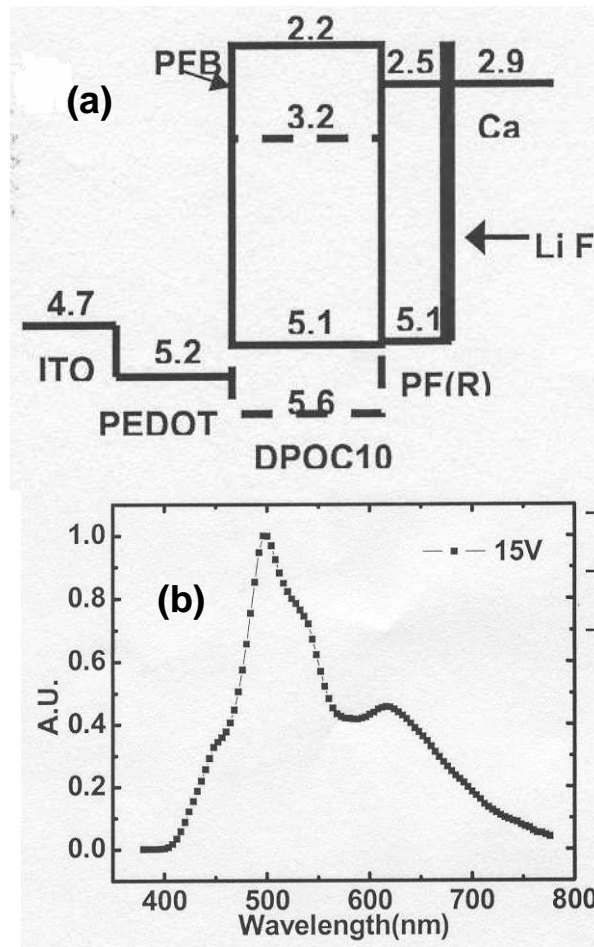
Figure 4.37: (a)Device structure for multilayer diode: PF(B)+DPOC$_1$0(60nm)/PF(R)(10nm)-LiF(6nm); (b)Spectra for upper device[7].

voltage. Due to the asymmetric electron and hole mobility, the recombination ratio in the layers changes continuously with the voltage. Two definite device structures are predicted to have wide-range color tunability from red to green to blue as the voltage increases from 3 to 13 V.

By considering the simulation model with asymmetric electron-hole Poole-Frenkel form mobility, this investigation has proposed two device structures which demonstrate full-color tuning while increasing bias voltage. The device with faster electron mobility for the green layer than that for the other layers can form the internal quantum efficiency ratio for the Red: Green: Blue layers (1:1.2:0.0) for low voltage, (1:7.0:3.0) for medium voltage and (1:13.5:12.0) for high voltage, and the respective CIE coordinates are (0.40,0.49)-(0.23,0.40)-(0.20,0.30). The internal quantum efficiency ratios for the device with thicker green layer and thinner blue layer from low to high voltage are (1:1.0:0.1)-(1:3.5:2.5)-(1:6.5:6.0) and the CIE coordinate transition is (0.41,0.48)-(0.25,0.40)-(0.21,0.31).

4.5 Experiments of color-tunable multilayer PLED

4.5.1 Device structure and fabrication

Four multilayered LEDs (devices AVD) are studied with various combinations of red (R), green (G), and blue (B) layers. The device structure for A is shown in Fig. 4.38(a).We use MEH-PPV for R, poly(2,3-diphenylphenylene vinylene) (DP10-PPV) [Fig. 4.38(b)] for G1, Dow Chemical LUMATION^{TM} Green-B polyfluorene (DPF) for G2, and poly[9,9-di-(2-ethylhexyl)-fluorenyl-2.7-diyl] (BEHF) [Fig. 4.38(c)] for B. MEH-PPV and DP10-PPV are synthesized[124, 125], DPF is from Dow Chemical Company[126], and BEHF is from Aldrich. The peaks of photoluminescence (PL) for the polymers are 592 nm (R), 500 nm (G1), 540 nm (G2), and 424 nm (B). Poly(3,4-ethylenedioxythiophene) doped with poly-styrene sulphonated acid (PEDOT:PSS) is used as the hole transport layer. A layer of poly(N-vinyl carbazole) (PVK) is added between PEDOT:PSS and the emissive layer in order to block the electrons. The electron affinity (EA) and ionization potential (IP) are indicated in Fig. 4.38(d). All the emissive polymers are dissolved in toluene with weight percentages 0.3 wt.% for R, 0.5 wt.% for G1, 1.2 wt.% for G2, and 1.5 wt.% for B. The concentration for R and G is lower than what is normally used for LED in order to have a thinner film. The layer thicknesses for the devices are as follows. Device A (B/G1/R): PEDOT/PVK (50 nm)/BEHF (70 nm)/ DP10-PPV (20 nm)/MEH-PPV (20 nm)/Ca; device B (B/G2/R): PEDOT/PVK
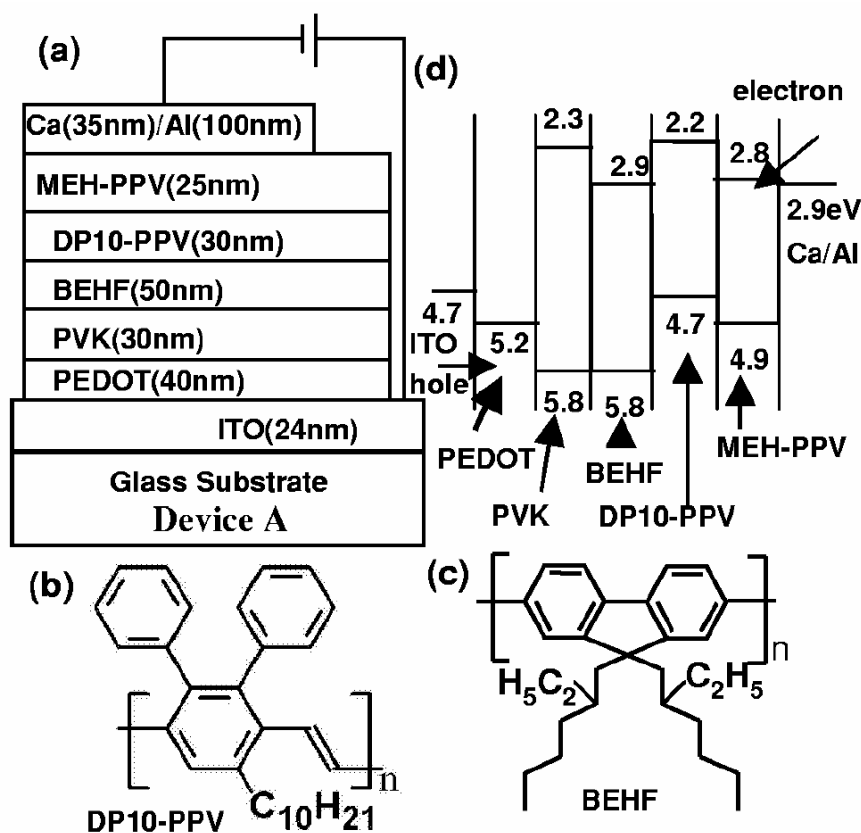
Figure 4.38: (a)Device structure of multilayer LED, (b)chemical structure of the emissive polymers DP10-PPV, and (c)BEHF. (d) The EA and IP are also shown.

(30 nm)/BEHF (50 nm)/DPF (30 nm)/ MEH-PPV (30 nm)/Ca; device C (B/G2): PEDOT/PVK (50 nm)/BEHF (70 nm)/DPF (30 nm)/Ca; device D (G2/B): PEDOT/PVK (50 nm)/DPF (70 nm)/BEHF (30 nm)/Ca. Each polymer layer is baked at 120^oC for 60 minutes in vacuum (10^{-3} torr) after spin-coating. It is crucial that the spin coating of the subsequent layer does not dissolve the previous layer. To check this, pure toluene is spin-cast on baked film and we found that the film thickness is reduced by no more than 5%. The Ca/Al cathode is evaporated and packaged in a glove box.
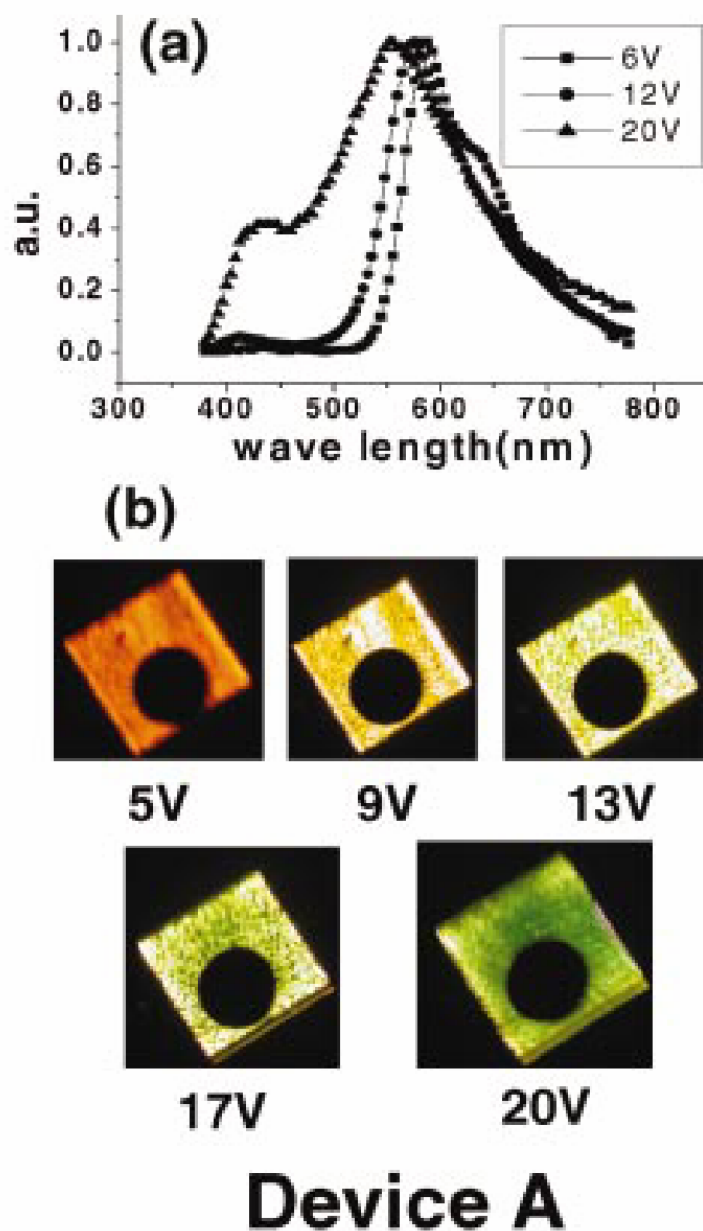
Figure 4.39: (Color)(a)Normalized spectra and (b)pictures of triple-layer device A(BGR) at various voltage.
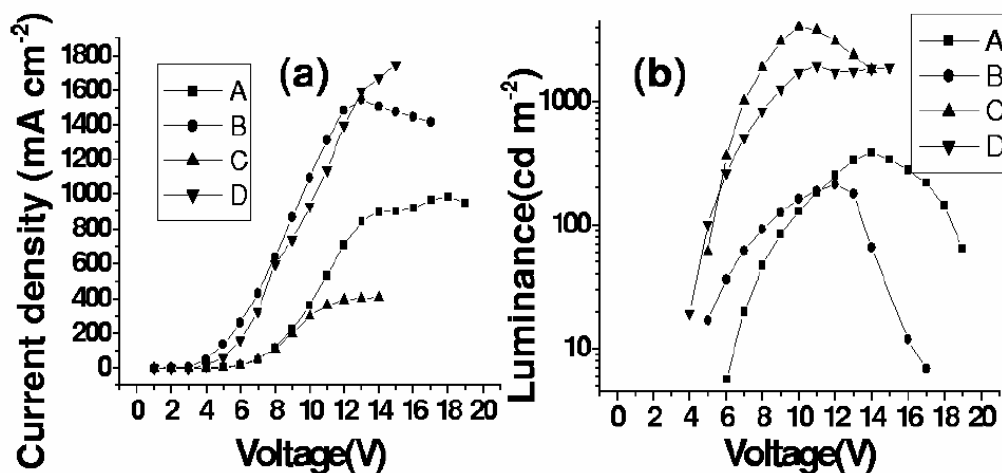
Figure 4.40: (a)Current-voltage and (b) luminescence-voltage relations for devices A-D.

4.5.2   Results for the experiments

The normalized emission spectrum and picture of device A with triple emission layers is shown in Fig. 4.39(a). At 6 V, the spectrum is identical to the PL of MEH-PPV because the electron-hole recombination concentrates near the cathode. As the bias voltage increases, there is a significant blueshift. It is yellow at 9 V and green at 13 V. The emission becomes greenish blue after 17 V. In the spectrum one sees clearly the emergence of the peak around 424 nm due to BEHF. The spectrum is, however, never dominated by the blue emission up to 20 V. The main reason is that the efficiency of blue polymers is much weaker than red and green polymers. Better color-tuning at higher voltage could be realized if more efficient blue polymers (or less efficient red and green) are used. The highest brightness is around 400 cd/m^2, reached at 14 V. Beyond 14 V, the brightness decreases and the current saturates at the same time (Fig. 4.40). This peculiar saturation behavior is reproduced in many triple-layer devices with similar structures. One possible reason is that as the voltage increases, a large amount of electrons are accumulated at the barrier between R and G, which screen the electric field effectively in the very thin R layer and cause an effective in-crease in the injection barrier from the cathode to R.20 The green polymer is replaced by DPF in device B. The spectrum shown in Fig. 4.41(a) starts to shift rigidly from red to green for voltage as low as 6 V. The blue emission is weaker, presumably due to the larger barrier between G2 and B. The current saturation at high voltage

is even more pronounced than de-vice A. Figure 4.41(b) shows the results for double-layer device C. As expected, there is an emergence of the blue emission as the voltage increases. Without the broad R emission, the B and G emission are well separated. Significant color-tuning occurs between 8 and 12 V. In order to test the mechanism of color-tuning further, we study device D, which has a re-versed order or G and B layers. As expected, from the stronger field dependence of electron mobility, the spectrum has a redshift instead of a blueshift as the voltage increases [Fig. 4.41(c)]. At low voltage, the recombination concentrates in the B layer, which is next to the cathode. The strong G emission at 7 V is due to the PL of the G layer excited by the B emission. There is no such effect in the other devices in which layers with larger band gaps are closer to the transparent ITO. The redshift of device D is a clear confirmation that the recombination zone is controlled by the mobility difference.

4.5.3 Discussion

The current and luminance are plotted in Fig. 4.40 as functions of voltage. In general, the double-layer devices are much brighter than the triple-layer devices. Perhaps the layer junctions introduce exciton quenching centers and the efficiency decreases with more junctions. The color is deter-mined by the field and the luminance is determined by the current. They change simultaneously in our LEDs. Many applications require independent control of the color and luminance. One may add a base layer between PEDOT:PSS and PVK to make a device similar to a bipolar junction transistor[18], in which color is controlled by the base-collector (Ca/Al) bias while current is controlled by the emitter (ITO) base bias.
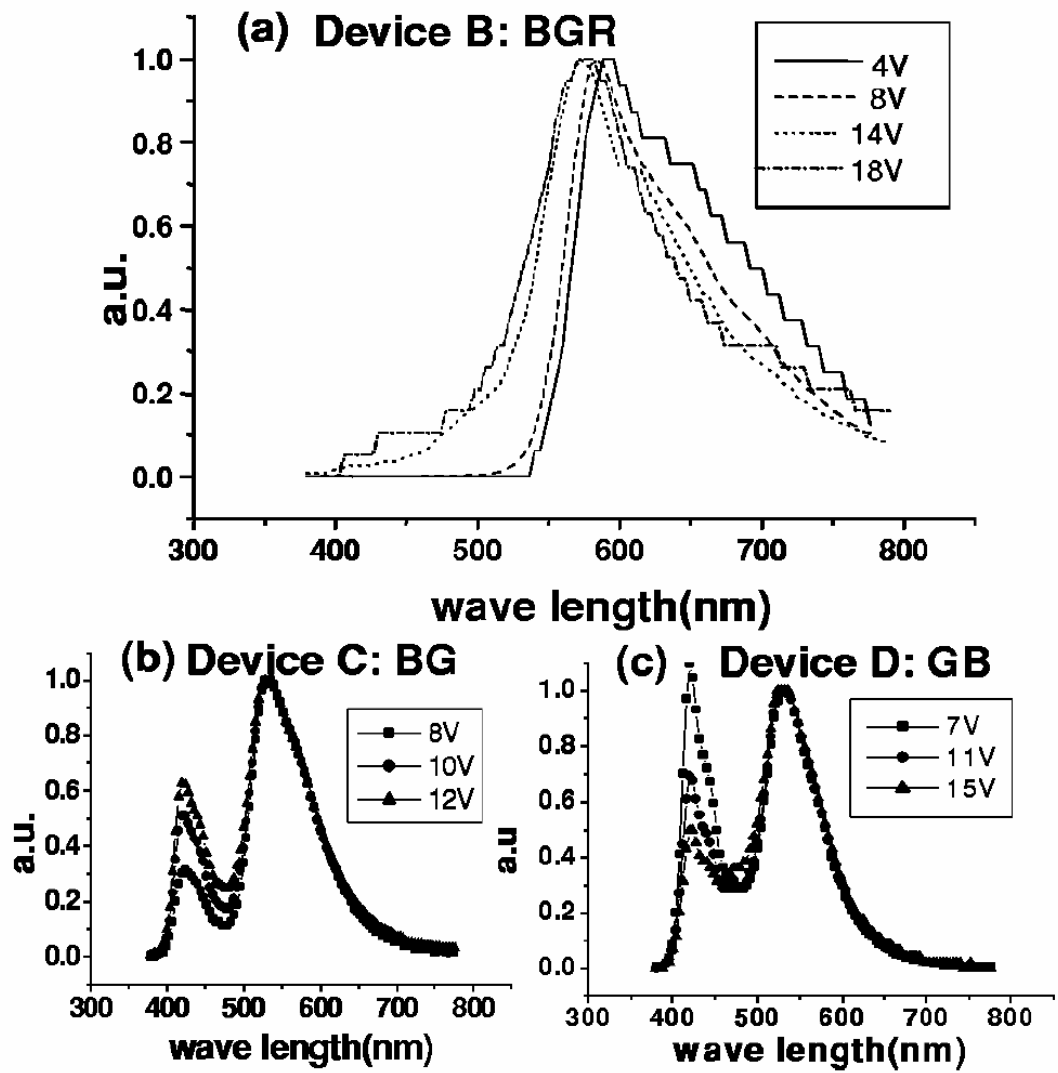
Figure 4.41: (a)Normalized spectra of triple-layer device B(BGR) and of (b)double-layer device C(BG) (c) D(GB). Green emission is normalized.

Appendix A

Matrix Element for Direct and Exchange Coulomb Scattering

In the Appendix we calculate the matrix element for direct and exchange Coulomb scattering involving one defect state and three band states.

1. Direct Term M_D

We start from integration over $\mathbf{r}_2$ in Eq.(2.3):

$$\int \psi_{v,-k_h}^*(\mathbf{r}_2) \frac{e^2}{4\pi\epsilon\epsilon_0|\mathbf{r}_1-\mathbf{r}_2|} \psi_{v,-k_{fh}}(\mathbf{r}_2) d^3\mathbf{r}_2$$

$$= \int e^{-i(k_{fh}-k_h)\mathbf{r}_2} u_{v,-k_h}^*(\mathbf{r}_2) u_{v,-k_{fh}}(\mathbf{r}_2) \frac{e^2}{4\pi\epsilon\epsilon_0|\mathbf{r}_1-\mathbf{r}_2|} d^3\mathbf{r}_2 , \quad \text{(A.1)}$$

where $\psi_{\mu,k}(\mathbf{r}) = e^{ikr} u_{\mu,k}(\mathbf{r})$ is the Bloch state. Set $\mathbf{r}_2 = R+\mathbf{r}$. R is the Bravais lattice vector and $\mathbf{r}$ runs over only one unit cell. Remember that $u_{\mu,k}(\mathbf{r})$ has the period of R. The integration region of $\mathbf{r}_2$ is divided into discrete lattice unit cells. Arranging the summation over R into two groups, one contains $\mathbf{r}_1$ and another one does not, the integral in Eq.(A.1) becomes

$$\sum_R \int_{cell\,at\,R} e^{-i(k_{fh}-k_h)(R+\mathbf{r})} u_{v,-k_h}^*(\mathbf{r}) u_{v,-k_{fh}}(\mathbf{r}) \frac{e^2}{4\pi\epsilon\epsilon_0|\mathbf{r}_1-(R+\mathbf{r})|} d^3\mathbf{r}$$

$$= \underbrace{\sum_{\mathbf{r}_1 \notin R} \int_{cell\,at\,R} \cdots}_{(a)} + \underbrace{\sum_{\mathbf{r}_1 \in R} \int_{cell\,at\,R} \cdots}_{(b)} \equiv I_a + I_b .$$

I_a and I_b are approximated separately. In group (a) $\mathbf{r}_2$ is far from $\mathbf{r}_1$, so we take $\mathbf{r}_2 \simeq R,(\mathbf{r} \simeq 0)$ to get

$$I_a = e^{-i(k_{fh}-k_h)\mathbf{r}_1} \sum_{\mathbf{r}_1 \notin R} e^{-i(k_{fh}-k_h)(R-\mathbf{r}_1)} \frac{e^2}{4\pi\epsilon\epsilon_0|\mathbf{r}_1-R|} \int_{cell\,at\,R} u_{v,-k_h}^*(\mathbf{r}) u_{v,-k_{fh}}(\mathbf{r}) d^3\mathbf{r} .$$

$$\text{(A.2)}$$

Assuming that the wave number $-k_h$ and $-k_{fh}$ in the last integral can be replaced by π/a, the band edge wave number, we have the approximation $\int_{cell\,at\,R} u_{v,-k_h}^*(\mathbf{r}) u_{v,-k_{fh}}(\mathbf{r}) d^3\mathbf{r} \simeq 1/N$, where N is the total number of unit cells. This is because that the integration would give unity by normalization if it were integrated over the whole space. But as the integration is over only one repeat unit cell, so it should be equal to $1/N$. I_a is simplified as

$$I_a = e^{-i(k_{fh}-k_h)\mathbf{r}_1} \sum_{\mathbf{r}_1 \notin R} e^{-i(k_{fh}-k_h)(R-\mathbf{r}_1)} \frac{e^2}{4\pi\epsilon\epsilon_0|\mathbf{r}_1-R|} \frac{1}{N} .$$

Taking $\mathbf{r}_1$ as the origin and performing the discrete R summation, we get

$$I_a = e^{-i(k_{fh}-k_h)\mathbf{r}_1} \frac{2e^2}{4\pi\epsilon\epsilon_0 a} \frac{1}{N} \left\{ -\ln\left[2\left|\sin\frac{(k_{fh}-k_h)a}{2}\right|\right] \right\} .$$

129

As for I_b, since $\mathbf{r}_2$ is close to $\mathbf{r}_1$ we can set $\mathbf{r}_2 = \mathbf{r}_1$ in the exponential term, and take it out of the integration:

$$I_b = e^{-i(k_{fh}-k_h)\mathbf{r}_1} \int_{cell} u^*_{v,-k_h}(\mathbf{r})u_{v,-k_{fh}}(\mathbf{r})\frac{e^2}{4\pi\epsilon\epsilon_0|\mathbf{r}|}d^3\mathbf{r} = e^{-i(k_{fh}-k_h)\mathbf{r}_1}\frac{U}{N} \ .$$

U is the on-site Coulomb energy. Adding I_a and I_b together, we get

$$I_a + I_b = \frac{2e^2}{4\pi\epsilon\epsilon_0 a}\frac{1}{N}e^{-i(k_{fh}-k_h)\mathbf{r}_1}m_D(k_{fh},k_h) \ ,$$

where

$$m_D(k_{fh},k_h) = \frac{4\pi\epsilon\epsilon_0 a}{2e^2}U - \ln\left[2\left|\sin\frac{(k_{fh}-k_h)a}{2}\right|\right]. \qquad (A.3)$$

Now we integrate over $\mathbf{r}_1$ to get the matrix element M_D.

$$\begin{aligned}
M_D(k_e,k_{fh},k_h) &= \left\{\int_{cell}\psi^*_d(\mathbf{r}_1)\psi_{c,k_e}(\mathbf{r}_1)e^{-i(k_{fh}-k_h)\mathbf{r}_1}d^3\mathbf{r}_1\right\}\frac{e^2}{4\pi\epsilon\epsilon_0 aN}m_D(k_{fh},k_h)\\
&= \left\{\int_{cell}u_{c,k_e}(\mathbf{r})\psi^*_d(\mathbf{r})d^3\mathbf{r}\right\}e^{-i(k_{fh}-k_h-k_e+\frac{\pi}{a})R_d}\frac{e^2}{4\pi\epsilon\epsilon_0 aN}m_D(k_{fh},k_h)\\
&= \frac{\alpha_c}{\sqrt{N}}\frac{e^2}{4\pi\epsilon\epsilon_0 aN}e^{-i(k_{fh}-k_h-k_e+\frac{\pi}{a})R_d}m_D(k_{fh},k_h) \ , \qquad (A.4)
\end{aligned}$$

where

$$\alpha_c \equiv \int_{all\ space}u_{c,k_e}(\mathbf{r})\psi^*_d(\mathbf{r})d^3\mathbf{r} = \sqrt{\frac{2}{a\kappa_c}} \ . \qquad (A.5)$$

R_d is the position of defect. α_c is the overlap between u_{c,k_e} and ψ_d. Using the "zero-radius-potential" model[48] to approximate the envelop function of the deep level by the bound state of a 1D δ−function potential well, the exponential decay of ψ_d is characterized by the decay coefficient $\kappa_c \equiv \sqrt{2m_c(E_c(k_0) - \frac{1}{2}\varepsilon_g - \Delta\varepsilon)}/\hbar$. $E_c(k_0) - \frac{1}{2}\varepsilon_g - \Delta\varepsilon$ is the defect level binding energy. k_0 is the wave number at the band edge. m_c is the effective mass of the conduction electron at the band minimum. The overlap α_c can be written as $\alpha_c = \sqrt{2/a\kappa_c} = \left[W_c/(\frac{1}{2}\varepsilon_g - \Delta\varepsilon)\right]^{1/4}$.

2. *Exchange Term M_E*

Exchanging the subscripts $v,-k_{fh}$ and c,k_e in M_D (See. Eq.(2.3) and (2.4)), and following the similar steps for $m_D(k_{fh},k_h)$, we obtain

$$M_E(k_e,k_h,k_{fh}) = \frac{\alpha_v}{\sqrt{N}}\frac{2e^2}{4\pi\epsilon\epsilon_0 aN}e^{-i(k_{fh}-k_h-k_e+\frac{\pi}{a})R_d}m_E(k_e,k_h), \quad (A.6)$$

$$m_E(k_e,k_h) = \gamma\left\{\frac{4\pi\epsilon\epsilon_0 a}{2e^2}U - \ln\left[2\left|\sin\frac{(k_e+k_h)a}{2}\right|\right]\right\}, \qquad (A.7)$$

and

$$\alpha_v \equiv \int_{all\ space} u_{v,-k_{fh}}(\mathbf{r})\psi_d^*(\mathbf{r})d^3\mathbf{r} \ . \tag{A.8}$$

α_v is the overlap between $u_{v,-k_{fh}}$ and ψ_d, which can be approximated as $\alpha_v = \left[W_v/(\frac{1}{2}\varepsilon_g + \Delta\varepsilon)\right]^{1/4}$. The exchange factor γ is defined by

$$\int_{cell\ at\ R} u_{v,-k_h}^*(\mathbf{r})u_{c,k_e}(\mathbf{r})d^3\mathbf{r} = \frac{\gamma}{N} \ . \tag{A.9}$$

γ characterizes the overlap between the valence and conduction band states, and is always smaller than one. The value for γ used in practice is obtained by fitting with the splitting between the singlet and triplet excitons in *ab initio* calculations[68].

Bibliography

[1] R. Friend, R. Gymer, A. Holmes, J. Burroughes, R. Marks, C. Taliani, D. Bradley, D. Dos Santos, J. Brédas, M. Lögdlund, and W. Salaneck. "Electroluminescence in Conjugated Polymers ". <u>Nature</u>, **397**:121, 1999.

[2] Thomas D. Anthopoulos, Jonathan P. J. Markham, Ebinazar B. Namdas, Ifor D. W. Samuel, Shih-Chun Lo, and Paul L. Burn. "Highly Efficient Single-layer Dendrimer Light-emitting Diodes with Balanced Charge Transport". <u>Appl. Phys. Lett.</u>, **82**:4828, 2003.

[3] Dongge Ma, Yufeng Hu, Yanguang Zhang, Lixing Wang, Xiabing, Fosong Wang, J. M. Lupton, I. D. W. Samuel, Shi-Chun Lo, and P.L. Burn. "Bright Electroluminescence from a New Conjugated Dendrimer". <u>Synth. Met.</u>, **137**:1125, 2003.

[4] L. Bozano, S. A. Carter, J. C. Scott, G. G. Malliaras, and P. J. Brock. "Temperature- and Field-Dependent Electron and Hole Mobilities in Polymer Light-Emitting Diodes". <u>Appl. Phys. Lett.</u>, **74**:1132, 1999.

[5] A. R Brown, D. D. C. Bradley, J. H. Burroughes, R. H. Friend, N. C. Greenham, P. L. Burn, A. B. Holemes, and A. Kraft. "Poly(p-)phenylenevinylene light-emitting diodes: Enhanced electroluminescent efficiency through charge carrier confinement". <u>Appl. Phys. Lett.</u>, **61**:2793, 1992.

[6] B. K. Crone. <u>Device Phyics of Polymer Light Emitting Diodes</u>. PhD thesis, Princeton University, July 1999.

[7] B. X. Chen. <u>Color Tunable Multilayer Conjugated Lighting-emitting Diode</u>. master thesis, National Tsing Hua University, July 2004.

[8] These datas are integrated by Opto-Electronics and System Laboratories in Industrial Technology Research Institute (OES/ITRI). The website is: http://www.oes.itri.org.tw/.

[9] J. H. Burrough, D.D.C. Bradley, A. R. Brown, R. N. Marks, K. Mackay, R. H. Friend, P. L. Burns, and A. B. Holmes. "Light Emitting Diodes Based on Conjugated Polymers". *Nature*, **347**:539, 1990.

[10] C. W. Tang and S. A. Slyke. "Organic Electroluminescent Diodes". *Appl. Phys. Lett.*, **51**:913, 1997.

[11] S. R. Forrest. "The Road to High Efficiency Organic Light Emitting Devices". *Or. Electr.*, **4**:45, 2003.

[12] S. R. Forrest. "The Path to Ubiquitous and Low-Cost Organic Electronic Application on Plastic". *Nature*, **428**:911, 2004.

[13] S. R. Forrest, P. Burrows, and M. Thompson. "The Dawn of Organic Electronics". *IEEE Spectrum*, **37**:29, 2000.

[14] Ananth Dodabalapur. "Organic Light Emitting Diodes". *Solid State Communications*, **102**:259, 1997.

[15] N. C. Greenham and R. H. Friend. "Semiconductor Device Physics of Conjugated Polymers". *Solid State Pysics (Ed.s. H. Ehrenreich and F. Spaepen)*, **49**:pp.1–149, 1995.

[16] A. J. Campbell, D. C. C. Bradley, and D. G. Lidzey. "Space-Charge Limited Conduction with Traps in Poly(phenylene vinylene) Light-Emitting Diodes". *J. Appl. Phys.*, **82**:6326, 1997.

[17] I. H. Campbell, D. L. Smith and J. P. Ferraris. "Electrical Impedance Measurements of Polymer Light-Emitting Diodes". *Appl. Phys. Lett.*, **66**:3030, 1995.

[18] S. M. Sze. *Physics of Semiconductor Devices*. Wiley, New York, second edition, 1981.

[19] E. M. Conwell and M. W. Wu. "Contact Injection into Polymer Light-Emitting Diodes". *Appl. Phys. Lett.*, **70**:1867, 1997.

[20] A. Rajagopal, C. I. Wu, and A. Kahn. "Energy Level Offset at Organic Semiconductor Heterojunctions". *J. Appl. Phys.*, **83**:2649, 1998.

[21] Y. Hirose, A. Kahn, V. Aristov, and P. Soukiassian. "Chemistry, Diffusion, and Electronic Properties of a Metal / Organic Semiconductor Contact: In / Perylenetetracarboxylic Dianhydride". *Appl. Phys. Lett.*, **68**:217, 1996.

[22] Y. Hirose, C. I. Wu, V. Aristov, P. Soukiassian, and A. Kahn. "Chemistry and Electronic Properties of Metal Contacts on an Organic Molecular Semiconductor". *Appl. Surf. Sci.*, **113**:291, 1997.

[23] P. Blom and M. de Jong. "Electrical Characterization of Polymer Light-Emitting Diodes". *IEEE J. Sel. Top. Quant. Ele.*, **4**:105, 1998.

[24] H. Antoniadis, M. A. Abkowitz, and B. R. Hsieh. "Carrie Deep-Trapping Mobility-Lifetime Products in Poly(p-phenylene vinylene)". *Appl. Phys. Lett*, **65**:2000, 1994.

[25] M. A. Lampert and P. Mark. *Current Injection in Solid*. Academic Press, New York, 1970.

[26] L. J. Rothberg, M. Yan, F. Papadimitrakopoulos, M. E. Galvin, E. W. Kwock, and T. M. Miller. "Photophysics of Phenyltnevinylene Polymers". *Synth. Met.*, **80**:41, 1996.

[27] W. Rehwald and H. G. Kiess. "Charge Transport in Polymer". *in Conjugated Conductiong Polymers(Ed. H. Kiess), Springer-Series in Solid-state Sciences*, **102**:pp. 135–173, 1992.

[28] C. Kittel. *Quantum Theory of Solid*. Wiley, New York, 1963.

[29] Z. Shuai, J. L. Bredas, and W. P. Su. "Nature of Photoexitations in Poly(para-phenylenevinylene) and its Oligomers". *Chem. Phys. Lett.*, **228**:301, 1994.

[30] J. -W. van der Horst, P. A. Bobbert, M. A. J. Michels, G. Brocks, and P. J. Kelly. "Ab Initio Calculation of the Electronic and Optical Excitations in Polythiophene: Effects of Intra- and Interchain Screening". *Phys. Rev. Lett.*, **83**:4413, 1999.

[31] L. D. Landau and E. M. Lifshitz. *Quantum Mechanics: Non-relativistic Theory*. Pergamon, Oxford, 3rd edition edition, 1977.

[32] H. Bässler. "Charge Transport in Disordered Organic Photoconductors: a Monte Carlo Simulaton Study". *Phys. Stat. Solidi B*, **175**:15, 1993.

[33] D. H. Dunlap, P. E. Parris, and V. M. Kenkre. "Charge-Dipole Model for the Universal Field Dependence of Mobilities in Molecularly Doped Polymers". *Phys. Rev. Lett.*, **77**:542, 1996.

[34] Yu. N. Gartstein and E. M. Conwell. "Hgih-Field Hopping Mobility in Molecular System with Spatially Correlated Energetic Disorder". *Chem. Phys. Lett.*, **77**:542, 1995.

[35] H. Meyer, D. Haarer, H. Naarmann, and H. H. Hörhold. "Trap Distribution for Charge Carriers in Poly(paraphenylene vinylene)(PPV) and its Substituted Derivative DPOP-PPV". *Phys. Rev. B*, **52**:2587, 1995.

[36] M. Abkowitz, J. S. Facci, and M. Stolka. "Time-Resolved Space Charge-Limited Injection in a Trap-Free Glassy Polymer". *Chem. Phys.*, **177**:783, 1993.

[37] R. G. Kepler, P. M. Beeson, S. J. Jacobs, R. A. Anderson, M. B. Sinclair, V. S. Valencia, and P. A. Cahill. "Electron and Hole Mobility in Tris(8-hydroxyquinolinolato-N1,O8) Aliminum". *Appl. Phys. Lett.*, **66**:3618, 1995.

[38] I. H. Campbell and D. L. Smith. "Schottky Energy Barriers and Charge Injection in Metal / Alq / Metal Structures". *Appl. Phys. Lett.*, submitted.

[39] I. H. Campbell, P. S. Davids, D. L. Smith, N. N. Barashkov and J. P. Ferraris. "The Schottky Energy Barrier Dependence of Charge Injection in Organic Light-Emitting Diodes". *Appl. Phys. Lett.*, **72**:1863, 1998.

[40] P. W. M. Blom, M. J. M. de Jong, and M. G. van Munster. "Electric-Field and Temperature Dependence of the Hole Mobility in Poly(p-phenylene vinylene)". *Phys. Rev. B*, **55**:R565, 1997.

[41] P. E. Burrows, Z. Shen, V. Bulovic, D. M. McCarty, S. R. Forrest, J. A. Cronin, and M. E. Thompson. "Relationship Between Electroluminescence and Current Transport in Organic Heterojunction Light-Emitting Devices". *J. Appl. Phys.*, **79**:7991, 1996.

[42] P. W. M. Blom, M. J. M. de Jong, and J. J. M. Vleggaar. "Electron and Hole Transport in Poly(p-phenylene vinylene) Devices". *Appl. Phys. Lett.*, **68**:3308, 1996.

[43] A. J. Campbell, M. S. Weaver, D. G. Lidzey, and D. D. C. Bradley. "Bulk Limited Conduction in Electroluminescent Polymer Devices". *J. Appl. Phys.*, submitted.

[44] D. Braun and A. J. Heeger. "Visble Light Emission from Semiconducting Polymer Diodes". *Appl. Phys. Lett.*, **58**:1982, 1991.

[45] P. S. Davids, I. H. Campbell, and D. L. Smith. "Direct Model for Single Carrier Organic Diodes". *J. Appl. Phys.*, **82**:6319, 1997.

[46] I. H. Campbell, T. W. Hagler, and D. L. Smith. "Direct Measurement of Conjugated Polymer Electronic Excitation Energies Using Metal / Polymer / Metal Structure". *Phys. Rev. Lett.*, **76**:1900, 1996.

[47] U. Albrecht and H. Bässlaer. "Langevin-Type Charge-Carrier Recombination in a Disordered Hopping System". *Phys. Stat. Solidi B*, **191**:455, 1995.

[48] V. N. Abakumov, V. I. Perel, and I. N. Yassievich. *Nonradiative Recombination in Semiconductors*. North-Holland, Armsterdam, 1991.

[49] V. Bulovic, G. Gu, P. E. Burrows, M. E. Thompson, and S. R. Forrest. "Transparent Light-emitting Devices". *Nature*, **380**:29, 1996.

[50] H. Murata, Z. H. Kafafi, and M. Uchida. "Efficient Organic Light-emitting Diodes with Undoped Active Layers based on Silole Derivatives". *Appl. Phys. Lett.*, **80**:189, 2002.

[51] H. Y. Chen, W. Y. Lam, J. D. Luo, Y. L. Ho, B. Z. Tang, D. B. Zhu, M. Wong, and H. S. Kwok. "Highly Efficient Organic Light-emitting Diodes with a Silole-based Compound". *Appl. Phys. Lett.*, **81**:574, 2002.

[52] Brian W. D'Andrade, Marc A. Baldo, Chihaya Adachi, Jason Brooks, Mark E. Thompson, and Stephen R. Forrest. "High-efficiency yellow double-doped organic light-emitting devices based on phosphor-sensitized fluorescence". *Appl. Phys. Lett.*, **79**:1045, 2001.

[53] M. A. Baldo, D. F. O'Brien, Y. You, A. Shoustikov, M. E. Thompson, S. R. Forrest. "Highly Efficient Phosphorescent Emission from Organic Electroluminescent Devices". *Nature (London)*, **395**:151, 1998.

[54] C. Adachi, M. A. Baldo, M. E. Thompson, and S. R. Forrest. "Nearly 100Organic Light Emitting Device". *J. Appl. Phys.*, **90**:5048, 2001.

[55] M. Ikai, S. Tokito, Y. Sakamoto, T. Suzuki, and Y. Taga. "Highly Efficient Phosphorescence from Organic Light-emitting Devices with an Exciton-block Layer". *Appl. Phys. Lett.*, **79**:156, 2001.

[56] Shizuo Tokito, Mitsunori Suzuki, Fumio Sato, Motoaki Kamachi, and Kourou Shirane. "High-efficiency Phosphorescent Polymer Light-emitting Devices". *Orgaic Electronics*, **4**:105, 2003.

[57] R. C. Kwong, M. R. Nugent, L. Michalski, T. Ngo, K. Rajan, Y. -J. Tung, M. S. Weaver, T. X. Zhou, M. Hack, M.E . Thompson, S. R. Forrest, and J. J. Brown. "High Operational Stability of Electrophosphorescent Devices". *Appl. Phys. Lett.*, **81**:162, 2002.

[58] J. C. Carter, I. Grizzi, S. K. Heeks, D. J. Lacey, S. G. Latham, P. G. May, O. Ruiz de los Pañ*os*, K. Pilcher, C. R. Towns, and H. F. Wittmann. "Operating Stability of Light-Emitting Polymer Diodes Based on Poly(p-phenylene vinylene)". *Appl. Phys. Lett.*, **71**:34, 1997.

[59] B. W. D'Andrade, J. Brooks, V. Adamovich, M. E. Thompson, and S. R. Forrest. "White Light Emission Using Triplet Excimers in Electrophosphorescent Organic Light-Emitting Devices". *Adv. Mater.*, **14**:1032, 2002.

[60] Chia-Hsin Chen and Hsin-Fei Meng. "Defect Auger Exciton Dissociation and Impact Ionization in Conjugated Polymers". *Phys. Rev. B*, **64**:125202, 2001.

[61] C.H. Chen and H.F. Meng. "Enhancement of Singlet Exciton Formation Ratio in Electroluminescent Conjugated Polymers by Magnetic Doping". *Phys. Rev. B*, **68**:94112, 2003.

[62] Chia-Hsin Chen and Hsin-Fei Meng. "Recombination Distribution and Color Tuning of Multilayer Organic Light-Emitting Diode". *submitted*.

[63] H. Meng and T. Hong. "Carrier Generation Mechanisms for Photoconductivity in Conjugated Polymers". *Phys. Rev. B*, **61**:9913, 2000.

[64] D. Moses, J. Wang, G. Yu, and A. Heeger. "Temperature-Independent Photoconductivity in Thin Films of Semiconducting Polymers: Photocarrier Sweep-out prior to Deep Trapping". *Phys. Rev. Lett.*, **80**:2685, 1998.

[65] M. Yan, L. Rothberg, F. Papadimitrakopoulos, M. Galvin, and T. Miller. "Defect Quenching of Conjugated Polymer Luminescence". *Phys. Rev. Lett.*, **73**:744, 1994.

[66] S. Nakajima, Y. Toyozawa, and R. Abe. *The Physics of Elementary Excitations*. Springer-Verlag, Berlin, 1980.

[67] P. da Cosda and E. Conwell. "Excitons and the Band-Gap in Poly(phenylene vinilene)". *Phys. Rev. B*, **48**:1993, 1993.

[68] The values of the intrachain dielectric constant ϵ, the on-site Coulomb repulsion energy U and the exchange factor γ in Table.1 are obtained by fitting our results of single configuration interaction calculation with the first principle calculations by Rohlfing *et al* (*Phys. Rev. Lett.*, **82**, 1959, 1999) on the lowest and second lowest singlet and triplet exciton energies.

[69] E. M. Conwell. "Hot Electrons and Impact Ionization in poly(p-phenylene vinylene)". *Phys. Rev. B*, **57**:R12670, 1998.

[70] K. Seeger. *Semiconductor Physics*. Springer-Verlag, Berlin, 2nd edition edition, 1982.

[71] M. Lannoo and J. Bourgoin. *Point Defects in Semiconductors*. Springer-Verlag, Berlin, 1981.

[72] U. Lemmer, R. Mahrt, Y. Wada, A. Greiner, H. Bässler, and E. Göbel. "Time-Resolved Luminescence Study of Recombination Porcesses in Electroluminescent Polymers". *Appl. Phys. Lett.*, **62**:2867, 1993.

[73] H. Gomes, P. Stallinga, H. Rost, A. Holmes, M. Harrison, and R. Friend. "Analysis of Deep Levels in a Phenylenevinylene Polymer by Transient Capacitance Methods". *Appl. Phys. Lett.*, **74**:1144, 1999.

[74] M. McGehee and A. Heeger. "Semiconducting (Conjugated) Polymers as Materials for Solid-State Lasers". *Ad. Mat.*, **12**:1655, 2000.

[75] R. Österbacka, M. Wohlgenannt, D. Chinn, and Z. Vardeny. "Optical Studies of Ttriplet Excitations in Poly(p-phenylene vinylene)". *Phys. Rev. B*, **60**:R11253, 1999.

[76] M. Rohlfing and S. Louie. "Optical Excitations in Conjugated Polymers". *Phys. Rev. Lett.*, **82**:1959, 1999.

[77] T. Hong and H. Meng. "Spin-Dependent Recombination and Electroluminescence Quantum Yield in Conjugated Polymers". *Phys. Rev. B*, **63**:075206, 2001.

[78] J. Wilson, A. Dhoot, A. Seeley, M. Khan, A. Köhler, and R. Friend. "Spin-Dependent Exciton Formation in π-Conjugated Compounds". *Nature*, **413**:828, 2001.

[79] M. Kobrak and E. Bittner. "Quantum Molecular Dynamics Study of Polaron Recombination in Conjugated Polymers". *Phys. Rev. B*, **62**:11473, 2000.

[80] M. Baldo, D. O'Brien, M. Thompson, and S. Forrest. "Excitonic Singlet-Triplet Ratio in a Semiconducting Organic Thin Film". *Phys. Rev. B*, **60**:14422, 1999.

[81] M. Wohlgenannt, K. Tandon, S. Mazumdar, S. Ramasesha, and Z. Vardeny. "Formation Cross-Sections of Singlet and Triplet Excitons in π-Conjugated Polymers". *Nature*, **409**:494, 2001.

[82] F. Cacialli, P. Ho, J. Kim, J. Burroughes, H. Becker, S. Li, T. Brown and R. Friend. "Molecular-Scale Interface Engineering for Polymer Light-Emitting Diodes". *Nature*, **404**:481, 2000.

[83] Y. Cao, I. Parker, G. Yu, C. Zhang, and A. Heeger. "Improved Quantum Efficiency for Electroluminescence in Semiconducting Polymers". *Nature*, **397**:414, 1999.

[84] Z. Shuai, D. Beljonne, R. J. Silbey, and J. L. Bredas. "Singlet and Triplet Exciton Formation Rates in Conjugated Polymer Light-Emitting Diodes". *Phys. Rev. Lett.*, **84**:131, 2000.

[85] R. Friend and N. Tessler. "Harvesting Singlet and Triplet Energy in Polymer LEDs". *Adv. Mater.*, **11**:285, 1999.

[86] M. Silberberg. *Chemestry: The Molecular Nature of Matter and Change*. Mosby-Year Book, St. Louis, 1996.

[87] B. Douglas and C. Hollingsworth. *Symmetry in Bonding and Spectra: An Introduction*. Academic Press,, San Diego, 1985.

[88] translated by B. Taylor O. Madelung. *Introduction to Solid-State Theory*. Springer-Verlag, Berlin, 1978.

[89] D. Beljonne, J. Cornil, D. dos Santos, Z. Shuai, and J. Brédas. *Chap. 19. in Primary Photoexcitation in Conjugated Polymers: Molecular Exciton versus Semiconductor Band Model, edited by N. Sariciftci*. World Scientific, Singapore, 1997.

[90] S. Abe, J. Yu, and W. Su. "Singler and Triplet Exctions in Conjugated Polymers". *Phys. Rev. B*, **45**:8264, 1992.

[91] B. Larsson, K. Hass, H. Ehrenreich, and A. Carlsson. "Theory of Exhange Interactions and Chemical Trends in Diluted Magnetic Semiconductors". *Phys. Rev. B*, **37**:4137, 1988.

[92] M. Yan, L. Rothberg, B. Hsieh, and R. Alfano. "Exciton Formation and Decay Dynamics in Electroluminescent Polymers Observed by Subpicosecond Stimulated-Emission". *Phys. Rev. B*, **49**:9419, 1994.

[93] H. Woo, O. Lhost, S. C. Graham, D. D. C. Bradley, R. H. Friend, C. Quattrocchi, J. L. Bredas, R. Schenk, and K. Mullen. "Optical-Spectra and Excitations in Phenylene Vinylene Oligomers". *Synth. Met.*, **59**:13, 1993.

[94] J. Halls, K. Pichler, R. Friend, S. Moratti, and A. Holmes. "Exciton Diffusion and Dissociation in a Poly(p-phenylenevinylene)/C-60 Heterojunction Photovoltaic Cell". *Appl. Phys. Lett.*, **68**:3120, 1996.

[95] E. Houzé, M. Nechtschein, and A. Pron. "Fixed-Spin-Induced ESR Linewidth and Polaron Mobility in Conducting Polymers". *Phys. Rev. B*, **56**:12263, 1997.

[96] K. Pokhodnya, A. Epstein, and J. Miller. "Thin-Film v[tcne](x) Magnets". *Adv. Mater.*, **12**:410, 2000.

[97] O. Inganäs. *Making Polymer Light Emitting Diodes with Polythiophenes, in Organic Electroluminescent Materials and Devices, edited by S. Miyata and H. S. Nalwa.* Gordon and Breach, Amsterdam, 1997.

[98] M. Berggren, O. Inganäs, G. Gustafsson, J. Rasmusson, M. R. Andersson, T. Hjertberg, and O. Wennerstrom. "Light-Emitting-Diodes with Variable Colors from Polymer Blends". *Nature(London)*, **372**:444, 1994.

[99] B. O. Dabbousi, M. G. Bawendi, O. Onitsuka, and M. F. Rubner. "Electroluminescence from CdSe Quantum-Dot/Polymer Composites". *Appl. Phys. Lett.*, **66**:1316, 1995.

[100] V. L. Colvin, M. C. Schlamp, and A. P. Alivisatos. "Light-Emitting-Didoes Made from Cadmium Selenide Nanocrystals and a Semiconducting Polymer". *Nature(London)*, **370**:354, 1994.

[101] C.C. Huang, H. F. Meng, G. K. Ho, C. H. Chen, C. S. Hsu, J. H. Huang, S. F. Horng, B. X. Chen, and L. C. Chen. "color-Tunable Multilayer Light-Emitting Diodes Based on Conjugated Polymer". *Appl. Phys. Lett.*, **84**:1195, 2004.

[102] B. K. Crone, P. S. Davids, I. H. Campbell, and D. L. Smith. "Device Model Investigation of Bilayer Organic Light Emitting Diodes". *J. Appl. Phys.*, **87**:1974, 2000.

[103] B. Ruhstaller, S. A. Carter, S. Barth, H. Riel, and J. C. Scott. "Trasient and Steady-State Behavior of Space Charges in multilayer Organic Light-Emitting Diodes". *J. Appl. Phys.*, **89**:4575, 2001.

[104] J. Staudigel, M. Stöβel, F. Steuber, and J. Simmerer. "A Quantitative Numeric Model of Multilayer Vapor-deposited Organic Light Emitting Diodes". *J. Appl. Phys.*, **86**:3895, 1999.

[105] H. Kobayashi, S. Kanbe, S. Seki, H. Kigchi, M. Kimura, I. Yudasaka, S. Miyashita, T. Shimoda, C. R. Towns, J. H. Burroughes, and R. H. Friend. "A Novel RGB Multicolor Light-Emitting Polymer Display". *Synth. Mat.*, **111-112**:125, 2000.

[106] J. Birnstock, J. Blässing, A. Hunze, M. Scheffel, M. Stöβel, K. Heuser, G. Wittmann, J. Wörle, and A. Winnacker. "Screen-Printed Passive Matrix Displays Based on Light-Emitting Polymers". *Appl. Phys. Lett.*, **78**:3905, 2001.

[107] J. Kalinowski, P. Di Marco, M. Cocchi, N. Camaioni, and J. Duff. "Voltage-Tunable-Color Multilayer Organic Light Emitting Diode". *Appl. Phys. Lett.*, **68**:2317, 1996.

[108] M. Granstrom and O. Inganäs. "White Light Emission from a Polymer Blend Light Emitting Diode". *Appl. Phys. Lett.*, **68**:147, 1996.

[109] M. Hamaguchi, A. Fujii, Y. Ohmori, and K. Yoshino. "Voltag- and Polarity-Tunable Organic Electroluminescent Devices". *Jpn. J. Appl. Phys.*, Part 2 **35**:L1462, 1996.

[110] Y. Z. Wang, R. G. Sun, F. Meghdadi, G. Leising, and A. J. Epstein. "Multicolor Multilayer Light-Emitting Devices Based on Pyridine-Containing Conjugated Polymers and Para-Sexiphenyl Oligomer". *Appl. Phys. Lett.*, **74**:3613, 1999.

[111] A. Kaur, M. Cazeca, S. Sengupta, J. Kumar, and S. Tripathy. "Voltage Tunable Multicolor Light Emitting Diodes Based on a Dye-Doped Polythiophene Derivative". *Synth. Met.*, **126**:283, 2002.

[112] X. Zhang and S. Jeneke. "Electroluminescence of Multicomponent Conjugated Polymers. 1. Roles of Polymer/Polymer Interfaces in Emission

Enhancement and Voltage-Tunable Multicolor Emission in Semiconducting Polymer/Polymer Heterojunctions". *Macromolecules*, **33**:2069, 2000.

[113] W. D. Gill. "Drift Mobilities in Amorphous Charge-Transfer Complexes of Trinitroflourenone and Poly-n-vinylcarbazole". *J. Appl. Phys.*, **43**:5033, 1972.

[114] S. V. Novikov and A. V. Vannikov. "Field-Dependence of Charge Mobility in Polymer Matrices". *Chem. Phys. Lett.*, **182**:598, 1991.

[115] C. M. Meller, I. H. Campbell, B. K. Laurich, D. L. Smith, P. L. Burn, J. P. Ferraris, and K. Müllen. "Solid-State-Concentration Effects on the Optical Absorption and Emission of Poly(p-phenylene vinylene)-Related Materials". *Phys. Rev. B*, **54**:5516, 1996.

[116] G. D. Hale, S. J. Oldenburg, and N. J. Halas. "Effect of Photo-oxidation on Conjugated Polymer Films". *Appl. Phys. Lett.*, **71**:1483, 1997.

[117] P. W. M. Blom, M. J. M. de Jong, and S. Breedijk. "Temperature Dependent Electron-Hole Recombination in Polymer Light-Emitting Diodes". *Appl. Phys. Lett.*, **71**:930, 1997.

[118] D. L. Scharfetter and H. K. Gummel. "Large-Signal Analysis of a Silicon Read Diode Oscillator". *IEEE Transactions on Electron Devices*, **ED-16**:64, 1969.

[119] H. William. *Numerical Recipes in C: the art of scientific computing.* Cambridge University Press, New York, 2nd edition edition, 1992.

[120] S. S. M. Wong. *Computational Methods in Physics and Engineering.* Prentice Hall, Englewood Cliffs, 1992.

[121] C. B. Duke. "Tunneling in Solid". *in Solid State Physics: Advances in Research and Applications (Ed. F. Seitz, D. Turbull and H. Ehrenreich)*, **10**:pp.1–353, 1969.

[122] R. H. Fowler and L. Nordheim. "Electron Emission in Intense Electric Fields". *Proc. Roy. Soc.*, **A119**:173, 1928.

[123] C. L. Novak and S. A. Shafer. *Color Vision in Color: Physics-based vision,Principles and Practice, Edited by G. E. Healey, S. A. Shafer, and L. B. Wolff.* Jones and Bartlett, Boston, 1992.

[124] C. Neef and J. Ferraries. "MEH-PPV: Improved Synthetic Procedure and Molecular Weight Control". *Macromolecules*, **33**:2311, 2000.

[125] W. C. Wan, H. Antoniadis, V. E. Choong, H. Razafitrimo, Y. Gao, W. A. Feld, and B. R. Hsieh. "Halogen Precursor Route to Poly[(2,3-diphenyl-p-phenylene)vinylene] (DP-PPV): Synthesis, Photoluminescence, Electroluminescence, and Photoconductivity". *Macromolecules*, **30**:6567, 1997.

[126] M. T. Bernius, M. Inbasekaran, J. O'Brien, and W. Wu. "Progress with Light-Emitting Polymers". *Adv. Mater(Weinheim, Ger.)*, **12**:1737, 2000.

Publication List

Theoretical Works

1. Chia-Hsin Chen and Hsin-Fei Meng, "Defect Auger Exciton Dissociation and Impact Ionization in Conjugated Polymers", _Phys. Rev. B_ **64**, 125202, 2001.

2. Chia-Hsun Chen and Hsin-Fei Meng, "Enhancement of Singlet Exciton Formation Ratio in Electroluminescent Conjugated Polymers by Magnetic Doping", _Phys. Rev. B_ **68**, 94112, 2003.

3. Chia-Hsin Chen and Hsin-Fei Meng, "Recombination Distribution and Color Tuning of Multilayer Organic Light-Emitting Diode", submitted.

Experimental Works

1. C.C. Huang, H. F. Meng, G. K. Ho, C. H. Chen, C. S. Hsu, J. H. Huang, S. F. Horng, B. X. Chen, and L. C. Chen, "Color-Tunable Multilayer Light-Emitting Diodes Based on Conjugated Polymer", _Appl. Phys. Lett._ **84**, 1195, 2004.

2. L. C. Lin, H. F. Meng, J. T. Shy, S. F. Horng, L. S. Yu, C. H. Chen, H. H. Liaw, C. C. Huang, K. Y. Peng, and S. A. Chen, "Triplet-to-Singlet Exciton Formation in Poly(p-phenylene-vinylene) Light-Emitting Diodes ", _Phys. Rev. Lett._**90**, 30366, 2003.